Louisiana State University
LSU Digital Commons

LSU Doctoral Dissertations | Graduate School

2012

Multiscale viscoplastic-viscodamage analysis of shape memory polymer fibers with application to self healing smart materials

Amir Shojaei
Louisiana State University and Agricultural and Mechanical College

Follow this and additional works at: https://digitalcommons.lsu.edu/gradschool_dissertations

 Part of the Mechanical Engineering Commons

Recommended Citation

Shojaei, Amir, "Multiscale viscoplastic-viscodamage analysis of shape memory polymer fibers with application to self healing smart materials" (2012). *LSU Doctoral Dissertations*. 2833.
https://digitalcommons.lsu.edu/gradschool_dissertations/2833

This Dissertation is brought to you for free and open access by the Graduate School at LSU Digital Commons. It has been accepted for inclusion in LSU Doctoral Dissertations by an authorized graduate school editor of LSU Digital Commons. For more information, please contactgradetd@lsu.edu.

MULTISCALE VISCOPLASTIC-VISCODAMGE ANALYSIS OF SHAPE MEMORY POLYMER FIBERS WITH APPLICATION TO SELF HEALING SMART MATERIALS

A Dissertation

Submitted to the Graduate Faculty of the
Louisiana State University and
Agricultural and Mechanical College
in partial fulfillment of the
requirements for the degree of
Doctor of Philosophy

in

The Department of Mechanical Engineering

by
Amir Shojaei
B.S., Mechanical Engineering, Kashan University, 2005
M.S. Mechanical Engineering, Amir-kabir University of Technology, 2008
May, 2012

DEDICATION

To my parents,

Tahereh and Mahmoud Shojaei,

and my dear wife

Soodabeh Sharafi

ACKNOWLEDGEMENTS

The author wishes to express deep appreciation to Dr. Guoiqang Li, the major professor and committee chairman, and Dr. George Z. Voyiadjis the minor professor for their encouragement and invaluable guidance throughout the research. I also acknowledge Professor Mehdy Sabbaghian for his precious supports and advices during my M.Sc. and Ph.D. programs. The author would also like to acknowledge the invaluable help and assistance from, Dr. Su-Seng Pang, and Dr. Shengmin Guo, as members of the committee and Dr. Ioan Negulescu as the Dean's representative.

Most of all, I would like to acknowledge my parents, Mahmoud and Tahereh for their continuous supports and love. I would also like to acknowledge and extend my thanks to my dear wife, Soodabeh, for her invaluable love and patient. This dissertation would not have been possible without their support and love.

TABLE OF CONTENTS

DEDICATION ……ii
ACKNOWLEDGEMENTS ……iii
LIST OF TABLES ……vi
LIST OF FIGURES ……viii
ABSTRACT ……xiii
CHAPTER 1 INTRODUCTION ……1
1.1 Self-Healing Materials ……1
1.2 New bio-mimic self-healing scheme ……2
1.3 Multiscale Analysis ……2
1.4 Research Objective ……2
1.5 Dissertation Outline ……3
1.6 References ……3
CHAPTER 2 MANUFACTURING AND CHARACTERIZATION OF THE SMP FIBER ……5
2.1 Manufacturing Process: ……5
2.2 Characterization Techniques: ……6
2.3 References ……6
CHAPTER 3 A MULTISCALE INELASTIC ANALYSIS OF SEMICRYSTALLINE GLASSY SHAPE MEMORY POLYMERS WITHIN THE MICROMECHANICS FRAMEWORK ……7
3.1 Nomenclature ……7
3.2 Introduction ……9
3.3 Finite Deformation Kinematics ……13
3.4 Semicrystalline characterization and constitutive equations ……15
3.5 Micromechanics ……22
3.6 Modified Two-phase TFA approach ……28
3.7 Computational Aspect ……37
3.8 Experimental observations and numerical implementations ……45
3.9 Conclusions ……53
3.10 References ……54
CHAPTER 4 A MULTISCALE VISCOPLASTIC THEORY OF SHAPE MEMORY POLYMER FIBERS ……63
4.1 Nomenclature ……63
4.2 Introduction ……64
4.3 Experimental characterization of shape memory polymer fibers ……70
4.4 Constitutive behaviors of semicrystalline shape memory polymer fibers ……74
4.5 Kinematic and Computational Aspect of Finite Stain ……82
4.6 Results and Discussion ……85
4.7 Concluding remarks ……88
4.8 References ……89
CHAPTER 5 CYCLIC VISCOPLASTIC-VISCODAMAGEANALYSIS OF SHAPE MEMORY POLYMER FIBERS WITH APPLICATION TO SELF HEALING SMART MATERIALS ……93
5.1 Nomenclature ……93
5.2 Introduction ……94
5.3 Thermodynamics of coupled plasticity-damage process ……95

5.4 SMP fibers characterization 98
5.5 Micromechanics Formulation....101
5.6 Micro-constituents governing relations....102
5.7 Cyclic damage analysis 108
5.8 Multiscale coupled viscoplastic-viscodamage computational aspects....112
5.9 Results and discussion....114
5.10 Conclusion....119
5.11 References 119
CHAPTER 6 SUMMARY AND FUTURE WORKS....123
6.1 Summary 123
6.2 Recommendation of Future Works 123
APPENDIX A: ESHELBY TENSOR 125
APPENDIX B: LETTERS OF PERMISSION TO USE PUBLISHED MATERIAL 128
VITA 131

LIST OF TABLES

Table 3-1 Iterative algorithm for an elastic-predictor/return mapping solution 41

Table 3-2 Outlines for a finite strain elasto-viscoplastic strain controlled elastic-predictor/plastic-corrector solution for the amorphous phase. (Superscripts "(n)" and "(n+1)" indicate respectively the previous and current load steps.) 42

Table 3-3 Material constants for the SMP system presented in Fig. 3-9 43

Table 3-4 Inelastic solution algorithm based on elastic-predictor/plastic-corrector for the crystalline phase (Superscripts "(n)" and "(n+1)" indicate respectively the previous and current load steps.). 44

Table 3-5 The tensile properties of PTT–PTMO copolymer [45] 46

Table 3-6 Material parameters for soft and hard segments computational modules 46

Table 3-7 Hypothetical crystalline slippage systems [98] 47

Table 3-8 Material parameters for crystalline and amorphous computational modules 50

Table 4-1 Fundamental difference between the previous study and the current study 69

Table 4-2 Material parameters for the stress recovery and cyclic hardening simulations 85

Table 4-3 Material parameters for crystalline and amorphous computational modules 86

Table 4-4 Hypothetical crystalline slippage systems [23] 87

Table 5-1 Material parameters for the crystalline and amorphous computational modules 118

Table 5-2 Hypothetical crystalline slippage systems 118

Table 5-3 Damage related material parameters 118

LIST OF FIGURES

Figure 1-1 Self-healing system based on CTH mechanism [9] 1

Figure 1-2 SEM and TEM pictures of (a) cracked and (b) healed configurations [8, 9] 2

Figure 2-1 Rolling heat treatment and winding process of the SMP fiber filaments 5

Figure 3-1 Schematic representation (a) intermediate and (b) polar decompositions in the finite deformation context 15

Figure 3-2 (a)Two-phase RVE, (b) added interfacial layer between inclusion and matrix and (c) dispersing computational seeds over the RVE..... 31

Figure 3-3 Flowchart for the multiscale analysis with proposed atomic computational strategy 31

Figure 3-4 (a) two-phase RVE with embedded inclusion at center and assembled computational seeds in 3D configuration, (b) primary micro-strain distribution around the inclusion from the trivial elastic solution under the biaxial macroscale strain E (This distribution is updated after each load increment once the inelastic strain or damage is initiated in either of sub-phases.) 34

Figure 3-5 Dilute RVE with magnified view of influence region for Eigen influence functions 35

Figure 3-6 Distribution of the Eigen influence functions in 3D 36

Figure 3-7 Regularization technique to reduce a spare RVE to an equivalent dilute media 37

Figure 3-8 Schematic representations of (a) fibrous inclusion, (b) Penny-shape inclusion, and (c) Assembled RVE in a macro length scale. 38

Figure 3-9 Simulation and experimental results for a SMP system with embedded thermoplastic particles [42] 43

Figure 3-10 A simplified flowchart for the implementation of the proposed computational strategy 45

Figure 3-11 Simulation and experimental results for a two-phase semicrystalline copolymer, experiments are after [45] 48

Figure 3-12 Simulation and experimental results for a two-phase semicrystalline copolymer, experiments are after [45] 48

Figure 3-13 Micromechanical simulations based on obtained empirical relations for correction factors $\chi(0)$ and $\chi(1)$ 49

Figure 3-14 Simulation and experimental results for a two phase semicrystalline polyurethane SMP (experiments are after [99]) 49

Figure 3-15 Micromechanical simulation for semicrystalline polyurethane SMP with different crystalline volume fraction content 50

Figure 3-16 Microscale strain distribution for a two-phase RVE with schematic RVE configuration 51

Figure 3-17 Microscale inelastic strain distribution for a two-phase RVE with 6 computational seeds placed at the middle plane of the RVE, y/A=0.5. The macroscale strain levels are: (a) $E = 11\%$, (b) $E = 21\%$ and (c) $E = 41\%$ 52

Figure 3-18 Microscale strain distribution for a three-phase RVE with schematic RVE configuration 52

Figure 3-19 Microscale inelastic strain distribution for a three-phase RVE with 30 computational seeds placed at the middle plane of the RVE, y/A=0.5. The macroscale strain levels are (a) $E = 1\%$ and (b) $E = 13\%$ 53

Figure 4-1 Schematic of the bio-inspired healing process of the proposed composite (3-D view) (a) a unit cell (bay) of SMP grid (ribs and z-pins) stiffened conventional thermoset polymer dispersed with thermoplastic particles. A macroscopic crack is introduced in the unit cell, which can be identified by visual or non-destructive inspections($T< T_g$), (c) crack closure process through recovery of the SMP fiber ribs and z-pins, when local heating is applied ($T> T_g$), (d) further temperature rising melts the thermoplastic particles which flow into the crack by capillary force and diffuse into the fractured surface by concentration gradient ($T> T_m$), (e) cooling down to below the glassy temperature, solid wedge can be formed and molecular entanglement will be established ($T< T_g$), magnified view shows the molecule entanglement at the crack interface..... 67

Figure 4-2 Closing of macroscopic crack due to shape recovery of the SMP grid skeleton through localized heating , (a) a SMP orthogrid stiffened thermoset polymer composite with a macroscopic crack at the center of the central bay, (b) FEA results for the displacement field at Y direction when stored stresses in SMP fibers are released by a local heating process. Magnified view shows closure of the macroscopic crack, (c) normal stress at x direction, (d) normal stress at y direction, (e) shear stress in xy plane, (f) equivalent von-Mises stress. 68

Figure 4-3 Polarized optical microscope image of the side view of the SMP fiber sample #1 with 0.04mm diameter (a) non-stretched fiber and (b) after 3rd cyclic load where the sample is stretched up to 350% of strain level 71

Figure 4-4 Polarized optical microscope image of the side view of the SMP fiber sample #2 with 0.002 mm diameter (a) non-stretched fiber and (b) after 3rd cyclic load where the sample is stretched up to 200% of strain level..... 71

Figure 4-5 Cyclic loading tests for a bundle of SMP fibers (a) 4 simple fiber #1 and (b) 4 simple fiber #2..... 72

Figure 4-6 Stress recovery test results with heating rate 0.35 ^{o}C/Sec and up to 90 ^{o}C (a) SMP fiber #1 after 3 strain controlled cyclic loads each of them up to 350% of the strain level with 50.8 (mm/min) strain rate, and (b) SMP fiber #2 after 3 strain controlled cyclic loads each of them up to 180% of the strain level with 50.8 (mm/min) strain rate..... 72

Figure 4-7 DMA test results (a) Phase angle $Tan\ \delta$ and (b) Storage modulus E' (c) Loss modulus E'' 74

Figure 4-8 FTIR test results for the SMP fiber #2 75

Figure 4-9 SAXS image for SMP fiber #1 (a) non-stretched fiber and (b) stretched fiber up to 350% of the strain level..... 75

Figure 4-10 Microstructural representation for the SMP fiber (a) primary microstructure of the SMP fiber which contains some crystalline phase, (b) cold drawn SMP fiber results in stress induced crystalline phase. 82

Figure 4-11 Computation algorithm for a micromechanics based multiscale analysis [23]..... 84

Figure 4-12 Simulation and experimental results for stress recovery of SMP fiber#1 based on different heating rates 85

Figure 4-13 Simulation results for various volume fractions of the crystalline and amorphous phases together with cyclic tension test results for the SMP fiber #1 up to 120% strain level with 50.8 mm/min strain rate..... 87

Figure 4-14 Simulation of the stress induced crystallization process in which internal and outer radii of the crystalline phase evolves with loading process..... 88

Figure 5-1 Schematic representation of the bio-mimetic self-healing material system (a) damaged configuration with a macroscale crack, (b) closed crack configuration due to the stress recovery process of SMP fibers, (c) diffusion of the molten Thermoplastic Particles (TPs) into the cracked matrix and (d) healed configuration with magnified view of the crack interface which shows molecular entanglement of the solidified TPs and thermosetting polymer molecular chain..... 96

Figure 5-2 Crystalline microstructure under biaxial loading condition (a) undeformed body, (b) formation of different type of dislocation due to the external loading condition and (c) microcrack formation. 99

Figure 5-3 Polymeric network under biaxial loading condition, (a) undeformed body, (b) conformational changes due to external loading, (c) stretched chains after saturation of conformational changes and (d) microcrack formation due to breakage of polymer chain. 99

Figure 5-4 Schematic representation of loading-unloading process for SMP fibers 100

Figure 5-5 RVE (a) non-stretched SMP fiber, and (b) stretched SMP fiber..... 102

Figure 5-6 Semicrystalline morphology (a) manufacturing induced spherulite microstructure under isotropic conditions and (b) stress induced crystallized microstructure 103

Figure 5-7 Recovery test results for SMP fiber #2 (a) after 150 % cyclic tensions, (b) corresponding recoverable strains 112

Figure 5-8 Recovery test results for SMP fiber #2 (a) after 300 % cyclic tensions, (b) corresponding recoverable strains 113

Figure 5-9 Computational modules for the proposed multiscale analysis where a Message Passing Interface is shown as the blue ellipse for parallel programming applications..... 114

Figure 5-10 Cyclic loading of SMP fiber with $\Delta\epsilon = 150\%$ and strain rate of 50.8 mm/min 115

Figure 5-11 Cyclic loading of SMP fiber with $\Delta\epsilon = 300\%$ and strain rate of 50.8 mm/min 115

Figure 5-12 Cyclic evolution of the crystalline axes 0.5,0.5,0.5 116

Figure 5-13 Viscoplastic response of SMP fiber at three different strain rates 117

Figure 5-14 Cyclic damage evolution of SMP fiber with loading conditions (a) $\Delta\epsilon = 150\%$, and (b) $\Delta\epsilon = 300\%$..... 117

ABSTRACT

Self-healing smart material systems have been introduced into the research arena and they have already been deployed into industrial applications. The Close-Then-Heal (CTH) healing mechanism for polymeric self-healing systems is addressed herein and then a new generation of Shape Memory Polymer (SMP) based self-healing system is proposed in this work. This system incorporates SMP fibers to close the cracks while the embedded Thermoplastic Particles (TPs) are diffused into the crack surfaces upon heating and provide a molecular level of healing.

The SMP fiber manufacturing procedure is briefly addressed in this work in which the bobbin of SMP fibers are heat treated in a specific procedure and then they are wound to produce SMP fibers. The performance of the proposed healing system is highly dependent on mechanical responses of SMP fibers.

The polyurethane SMP fibers are categorized as semicrystalline polymeric material systems. These semicrystalline SMP fibers are then constituted from two distinguishable phases, which are amorphous and crystalline polymers. Such a multiphase system can be evaluated through a multiscale analysis within the micromechanics framework in which the macroscopic mechanical responses are evolved through averaging the microscale mechanical fields. Then in this research the constitutive relation for each of the micro-constituents are utilized to compute the microscale mechanical fields and then these fields are correlated to the macroscopic field through the micromechanics framework.

The cyclic viscoplastic and viscodamage of these fibers are of utmost importance for designing self-healing systems in which repeatability of the healing process and the healing efficiency for subsequent healing cycles are highly dependent on cyclic responses of these fibers. A new approach in measurement of cyclic damage of SMP fibers is proposed in this work in which the reduction in recoverable stress after each cyclic stress recovery is correlated to the damage. In this approach the damage is interpreted as failure of the polymeric bonds to recover their original shape (SM effect).

In general the proposed self-healing scheme establishes a new generation of self-healing systems while the developed theoretical multiscale analysis provides a well-structured method to investigate the cyclic viscoplastic and viscodamage of the SMP fibers.

CHAPTER 1 INTRODUCTION

1.1 Self-Healing Materials

The self-healing smart materials with the ability to heal micro- and macro-scale damages have been developed and deployed into the research and industrial applications recently. These smart materials may use a microencapsulated healing agent inside their matrix, in which micro- or macro-damages fracture the wall of the microcapsules and the released healing agent solidifies in presence of catalysts and heals the micro cracks and/or voids [1]. Toohey et al. extended this idea by designing a microvascular network, within the body of the system, to feed the healing agent continuously into the material [2]. However, this system suffers from clogging of vascular network after first round of healing which limit the repeatability of the healing process. Particularly, the performance of these systems in healing macro-scale damages is still an obstacle that must be overcome. This kind of healing methodology is referred to as a coupled damage-healing system herein to indicate that both the damage and the healing processes are activated concurrently in the system. The healing systems utilizing external triggering to activate the healing mechanism are referred to as a decoupled damage healing systems herein. In these types of systems the damage and the healing processes occur separately, where just one of these processes are active. These systems may utilize thermoplastic particles [3], thermally reversible covalent bonds [4], confined shape recovery of shape memory polymers [5], or biomimic two-step close-then-heal (CTH) mechanisms to molecularly heal structural-length scale damages [6-8].

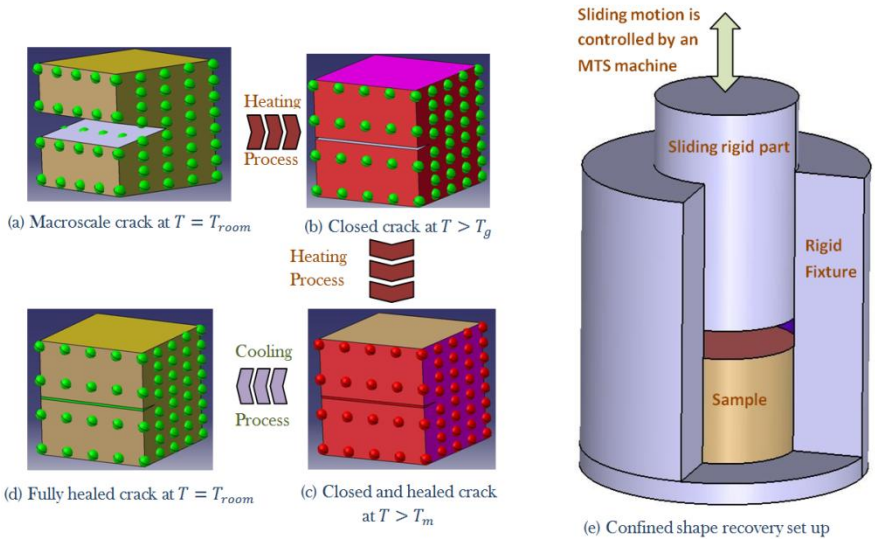

Figure 1-1 Self-healing system based on CTH mechanism [9]

Figure 1-1 shows the schematic of a typical CTH self-healing system which utilizes the confined shape recovery of SMP to close the crack and upon further heating the diffusion of the melted TPs into the crack surfaces provides a molecular length scale healing as shown in Fig. 1-2.

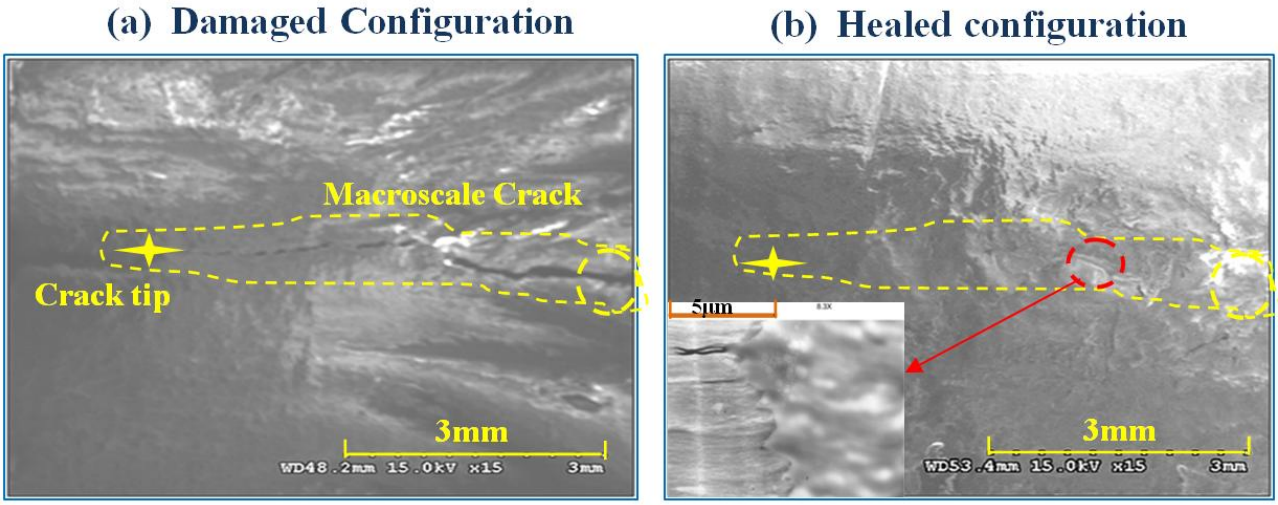

Figure 1-2 SEM and TEM pictures of (a) cracked and (b) healed configurations [8, 9]

1.2 New bio-mimic self-healing scheme

The high cost of the SMP, as the matrix phase, may be considered as a drawback for the classical CTH mechanisms. A novel modification in design of SMP based self-healing systems are proposed in which the SMP fibers are utilized as closing agent which reduce the cost of self-healing systems considerably while the need for external confinement is eliminated through specific programming of SMP fibers. In this new healing scheme the local heating activates the SMP fibers and upon shrinking these fibers the crack is closed. This recovery strategy opens a wide structural application for SMP fibers in which the embedded programmed fibers provides the closing step for the healing process.

1.3 Multiscale Analysis

The tendency to the multiscale elasto-plastic-damage analysis of material systems has been increased significantly during past decade and the capability of these theories in accurately capturing the coupled viscoplastic-viscodamage phenomenon has been addressed in the literature [10, 11].

1.4 Research Objective

It is found that with the proposed new CTH scheme the application of the self-healing materials in bioengineering and aerospace industries enters to a new arena in which upon detection of the damaged

zone a local heating process can fulfill all the healing steps. The detection procedure can be through visual inspections or Non-Destructive techniques. To accomplish the design and implementation of such a self-healing scheme a full understanding of thermomechanical responses of SMP fibers are required. In this work, a multiscale viscoplastic-viscodamage theory is developed to predict the cyclic responses of SMP fibers. In addition, the experimental tests are implemented to backup the proposed theory.

1.5 Dissertation Outline

This dissertation deals with three subtopics: Multiscale modeling through the micromechanics framework, proposing new CTH healing scheme and a viscoplastic model for SMP fibers and cyclic loading analysis of SMP fibers. The chapters are written in the form of a journal paper.

In Chapter 2, the Transformation Field Analysis is presented with detailed discussion on proposed modification on this theory. In Chapter 3, a viscoplastic theory for SMP fibers is proposed and the new CTH system is elaborated. Chapter 4 covers the cyclic loading analysis of SMP fibers and a coupled viscoplastic-viscodamage theory is proposed. Chapter 5 is the summary of this dissertation. Some recommendations of future works are also given in this chapter.

1.6 References

[1] White, S. R. , Sottos, N. R. , Geubelle, P. H. , Moore, J. S. , Kessler, M. R. , Sriram, S. R. , Brown, E. N. and Viswanathan, S., *Autonomic healing of polymer composites* Nature, 2001. **409**(6822): p. 794-797.

[2] Toohey, K.S., Sottos, N.R., Lewis, J.A., Moore, J.S. and White, S.R., *Self-healing materials with microvascular networks.* Nat Mater, 2007. **6**(8): p. 581-585.

[3] Zako, M. and N. Takano, *Intelligent Material Systems Using Epoxy Particles to Repair Microcracks and Delamination Damage in GFRP.* Journal of Intelligent Material Systems and Structures, 1999. **10**(10): p. 836-841.

[4] Liu, Y.L. and Y.W. Chen, *Thermally Reversible Cross-Linked Polyamides with High Toughness and Self-Repairing Ability from Maleimide- and Furan-Functionalized Aromatic Polyamides.* Macromolecular Chemistry and Physics, 2007. **208**(2): p. 224-232.

[5] Li, G. and M. John, *A self-healing smart syntactic foam under multiple impacts.* Composites Science and Technology, 2008. **68**(15-16): p. 3337-3343.

[6] Li, G. and D. Nettles, *Thermomechanical characterization of a shape memory polymer based self-repairing syntactic foam.* Polymer, 2010. **51**(3): p. 755-762.

[7] Li, G. and N. Uppu, *Shape memory polymer based self-healing syntactic foam: 3-D confined thermomechanical characterization.* Composites Science and Technology, 2010. **70**(9): p. 1419-1427.

[8] Nji, J. and G. Li, *A Biomimetic Shape Memory Polymer Based Self-Healing Particulate Composite.* Polymer 2010. **51**: p. 6021-6029

[9] Voyiadjis, G. Z., Shojaei, A, Li, G. and Kattan, P.I., *A Theory of Anisotropic Healing and Damage Mechanics of Materials.* Proceeding of The Royial Society A, 2012. **468**(2137): p.163-183.

[10] Chaboche, J. L., Kruch, S., Maire, J. F. and Pottier, T., *Towards a micromechanics based inelastic and damage modeling of composites.* International Journal of Plasticity, 2001. **17**(4): p. 411-439.

[11] Kruch, S. and J.-L. Chaboche, *Multi-scale analysis in elasto-viscoplasticity coupled with damage.* International Journal of Plasticity, 2011. **27**(12): p. 2026-2039.

[12] Meng, Q.H. and J.L. Hu, The Influence of Heat Treatment on Properties of Shape Memory Fibers: I. Crystallinity, Hydrogen Bonding and Shape Memory Effect. Journal of Applied Polymer Science, 2008. 109: p. 2616-2623.

CHAPTER 2 MANUFACTURING AND CHARACTERIZATION OF THE SMP FIBER

In this work two types of single SMP fibers (filaments) are characterized in which their microstructure changes upon cold drawing process are evaluated. In the following the manufacturing process and the characterization techniques that have been incorporated in this work are briefly discussed.

2.1 Manufacturing Process:

The shape memory polyurethane based on polyester polyol and it is a PCL-4000-based shape memory polyurethane[1]. The polyurethane was synthesized from poly(butylene adipate)-600 (Mn) (PBA), 4'4 -diphenylmethane diisocyanate (MDI) and 1,4-butanediol (BDO). On average, the molar ratio of (MDI+BDO): PBA=3:1. The average formula weight ratio of (MDI+BDO): PBA=1021:650. The hard segment, soft segment, and their contents were selected to prepare polyurethane with amorphous soft segment phase and crystalline hard segment phase. The soft segment phase has a glass transition at about -50 ^{o}C and a melting transition at about 47 ^{o}C. Based on the manufacturing procedure, discussed in [1], the SMP fibers were spun using a spinning machine. The pure nitrogen gas was injected for protection and the temperature was kept about 210 ^{o}C with the winding up speed of 100 m/min. A schematic representation of the spinning process of SMP fiber is shown in Fig. 2-1.

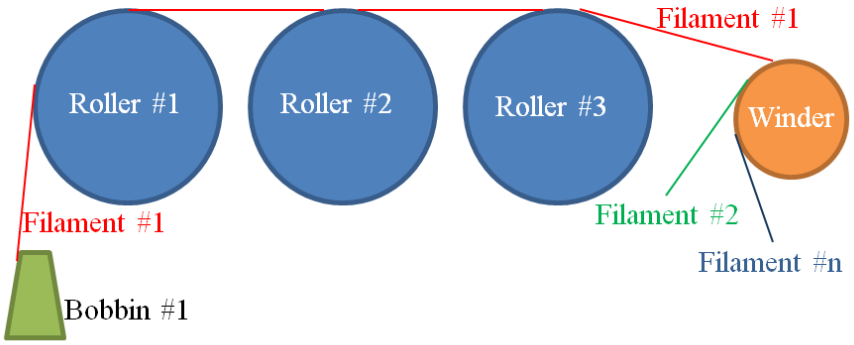

Figure 2-1 Rolling heat treatment and winding process of the SMP fiber filaments

The SMP filaments at each roller is heat treated while the speed and temperature of the three rollers are controlled and the filaments are wound at winder without external stress [2, 3]. The effect of the heat treatment and the temperature range of rolling process on the degree of crystallinity and mechanical properties of the hard segment is investigated in the literature [1-3].

2.2 Characterization Techniques:

A Material Testing System (MTS) Alliance RT/5 machine, which is specified for fiber tension tests, is utilized to cyclically stretch the SMP fibers. Dynamic mechanical analysis (DMA) tests were carried out on a Rheometric Scientific, RSA III Mechanical Analyzer, operated in a tensile mode. The heating rate was 5 ^{o}C/min, testing frequency 1 Hz, and the oscillation amplitude 5.0 μm. Tests were conducted over the temperature range from 25 to150 ^{o}C. The gauge length between the clamps was 30 mm and the fiber diameter was 0.04 mm, measure from Optical Microscopy images. Fourier Transform Infrared spectrometry test was carried out and the transmission spectra were determined using a TENSOR 27 spectrometer at room temperature. Small Angle X-ray Scattering (SAXS) experiments were conducted at facilities in the Center for Advanced Microstructures and Devices (CAMD) at Louisiana State University to investigate the microstructural change of SMP fibers upon cold drawing process. The results of these experiments are presented in Chapter 4 with detailed discussion.

2.3 References

[1] Meng, Q.H. and J.L. Hu, The Influence of Heat Treatment on Properties of Shape Memory Fibers: I. Crystallinity, Hydrogen Bonding and Shape Memory Effect. Journal of Applied Polymer Science, 2008. 109: p. 2616-2623.

[2] Qinghao, M., et al., Morphology, phase separation, thermal and mechanical property differences of shape memory fibres prepared by different spinning methods. Smart Materials and Structures, 2007. 16(4): p. 1192.

[3] Meng, Q., J. Hu, and Y. Zhu, Shape-memory polyurethane/multiwalled carbon nanotube fibers. Journal of Applied Polymer Science, 2007. 106(2): p. 837-848

CHAPTER 3 A MULTISCALE INELASTIC ANALYSIS OF SEMICRYSTALLINE GLASSY SHAPE MEMORY POLYMERS WITHIN THE MICROMECHANICS FRAMEWORK [*]

3.1 Nomenclature

$A_{ij}^{(\alpha)}$ skew-symmetry part of the Schmid tensor

$A_{ijkl}^{(r)}$ strain concentration tensor

$B_{ijkl}^{(r)}$ stress concentration tensor

c_i crystallographic axes vector

d_{ij} Lagrangian strain tensor

d_{ij}^{e} Lagrangian elastic strain tensor

d_{ij}^{p} Lagrangian plastic strain tensor

D_{ij} Eulerian strain tensor

D_{ij}^{e} Eulerian elastic strain tensor

D_{ij}^{p} Eulerian plastic strain tensor

$\dot{D}_{ij}^{c}$ inelastic crystalline stretch rate tensor

$D_{ijkl}^{(sr)}$ eigenstrain influence tensor

$F_{ijkl}^{(sr)}$ eigenstress influence tensor

F_{ij} total deformation gradient tensor

F_{ij}^{e} elastic deformation gradient tensor

F_{ij}^{p} plastic deformation gradient tensor

L_{ij}^{c} crystalline velocity gradient tenor

L_{ijkl} stiffness tensor

M_{ijkl} compliance tensor

[*] Paper submitted to ELSEVIER JOURNAL of INTERNATINAL JOURNAL OF PLASTICITY for peer review

$\aleph_{ij}$ eigenstress tensor

σ_{ij} Cauchy stress tensor

ϵ_{ij} strain tensor

τ_{ij}^{p} first Piola-Kirchhoff tensor

$\tau^{(\alpha)}$ crystalline phase Cauchy shear stress, associated with the αth slippage system

$|\tau|$ amorphous phase shearing stress

μ shear modulus

$\mu_{ij}^{(r)}$ eigenstrain tensor

ν Poisson's ratio

α_{ij} amorphous phase back stress tensor

X_{ij} amorphous phase deviatoric back stress tensor

S_{ij}^{p} second Piola-Kirchhoff tensor

S_{ij}^{c} deviatoric Cauchy stress tensor

S_{ij}^{c*} crystalline deviatoric Cauchy stress tensor, projected at the c_i direction

S_{ij}^{cp} deviatoric Cauchy stress tensor, projected perpendicular to the c_i direction

s_{ij}^{*} driving stress tensor in the amorphous phase

s amorphous athermal shear strength

R_{ij} rotation tenor

U_{ij} stretch tensor

$R_{ij}^{(\alpha)}$ symmetric part of the Schmid tensor

$\dot{\gamma}^{(\alpha)}$ crystalline shearing strain rate associated with αth slippage system

$|\dot{\gamma}^{p}|$ amorphous shearing strain rate

W_{ij}^{c} spin tensor

W_{ij}^{c*} lattice spin tensor

3.2 Introduction

3.2.1 Semicrystalline polymers and polyurethane SMP:

In general polymers are constituted from long disordered molecular chains and entangled coils. Amorphous polymers can be produced when this disordered polymeric network is frozen during the cooling down process. Crystallization process occurs when the disordered structure is rearranged into an ordered structure. In some cases the crystallization may occur during the cooling down process, in which the crystalline lamellae are created in the direction of the largest temperature gradients, or under mechanical loading, i.e. stress induced crystallization, at temperatures well below the glass transition temperature. In many cases the crystallization process is not fully developed chemically and the resulting microstructure contains 10 wt% up to 80 wt% crystalline segment. This partially ordered polymeric microstructure is called semicrystalline polymer [4, 5]. The properties of semicrystalline polymers are determined not only by the degree of crystallinity, but also by the size and orientation of the molecular chains.

Polyurethane SMP is classified as a polyurethane elastomer with crystalline hard phase and amorphous soft phase. Generally polyurethane elastomers are block copolymers of $(AB)_n$ molecular structure where A and B correspond respectively to the soft and hard phases. These phases serve to give the polymer its extensibility property and stiffness, respectively [6-8]. In the case of smart material systems, polyurethane SMP is one of the most prominent thermoplastic SMPs when solution, melting and diffusion processability, and repeatability of the Shape Memory (SM) cycle are required. In this SMP system, the soft segment produces a thermally activated SM effect when temperature exceed the transition temperature, T_s, while the hard segment is responsible for maintaining the overall shape of the structure above T_s [9]. Soft segment may consist of the amorphous (i.e. polyester and polyether) or the semi-crystalline (i.e. poly(ε-caprolactone) (PCL)) structures while the hard segments (i.e. diisocyanate (TDI), aromatic urethane or aramid) may be dispersed over soft segment to produce thermally stable chemical or physical cross linkages. Due to difficulties for adjusting glass transition temperature, T_g, in the amorphous phase, semi-crystalline soft segments are preferred [10, 11]. The hard segment made from urethane tends to degrade upon heating cycles and a thermally stable fast crystallizing hard segment made from aramid has replaced the urethane [12, 13]. As reported by Rabani et al. [11] long segments of PCL with high fraction of aramid hard segment (30-40 wt%) has resulted in a 98% strain recovery SM property.

In polyurethane elastomers the hard segment can undergo phase separation and produced distinguishable domains [14, 15]. Appearance of these distinctive microphase segregations are dependent on degree of compatibility between the soft segment molecular chains and the hard segment blocks [6-8]. This segregated structure may motivate designers to incorporate a micromechanical approach for characterization of semicrystalline polymer-based material systems, such as polyurethane SMP, in

which the geometry of the microscale domains together with their individual mechanical properties are utilized to obtain the associated global mechanical responses.

3.2.2 Micromechanical based approach:

The micromechanisms associated with the permanent inelastic deformation and recoverable elastic strains of solids cannot be examined within classical continuum elastoplastic framework. On the other hand, the molecular dynamic calculations based on the interatomic forces have shown unrealistic results for an inelastic deformation analysis of solids [16-18]. Hence, the experimental procedures in material characterizations remain the most promising way to explore their mechanical responses [19, 20].

The microstructural configuration of heterogeneous materials could be correlated to the macroscopic constitutive relations through micromechanics framework. The Representative Volume Element (RVE) concept is utilized in establishment of this correlation. The RVE represents a specific arrangement of sub-phases, each of them with specific geometry and/or mechanical properties [21]. Accordingly the RVE should be large enough to represent the microstructural morphology and sufficiently small for neglecting the macroscopic mechanical gradients over that.

Micromechanical based theories may provide certain bounds for the macroscale properties according to the microstructural properties and the exact elasticity solutions, e.g. Reuss, Viogt and Hashin-Shtrikman bounds [21], or inelastic analysis [22, 23]. Balendran and Nemat Nasser evaluated the bound of stored elastic energy in a heterogeneous media [24]. Another micromechanical approach is referred as *average field theory* which takes into account the average micro-stress and micro-strain fields to estimate the macroscale mechanical response of the heterogeneous media. This approach was proposed formerly by Eshelby [25] and later it has been developed to the Mori-Tanaka and self-consistent methods [21]. *Homogenization micromechanical theory* is applied to heterogeneous materials with periodic microstructure, in which a multi-scale perturbation analysis is implemented to estimate the effective properties [26, 27]. This method build up the macroscopic RVE through periodic unit cells and periodic boundary conditions and Finite Element (FE) or fast Fourier transforms are required to solve the problem.

Localization relations within the micromechanical framework bridge the microscopic and macroscopic fields. When the media behaves elastically, these relations are exact [21]. The main difficulty arises when the non-linearity is introduced in mechanical behavior of the sub-phases such as inelastic deformation or damage [28]. In general three approaches, within the micromechanical based multi-scale analysis, are available to establish the localization relations while the non-linearity is taking into the account:

- *Analytical approaches*: Following Eshelby's elastic solution for an ellipsoidal inclusion embedded in an infinite media [25], non-linear matrices with linearization of Eshelby's solution have been investigated. Secant linearization approach was developed by Berveiller and Zaoui [29] which is applicable only to monotonic loading condition. Elastoplastic analysis within micromechanics framework for an ellipsoidal crystal, which is embedded in a finite

homogeneous media, was discussed by Hill [30]. The self-consistent approach together with the tangent linearization was utilized by Hill to establish the constitutive relations. This tangent linearization is capable of modeling cyclic loading condition [30, 31]. An isotropic and non-isotropic splitting algorithm for the tangent modulus compensates for the difficulty in computing the tangent operator of the Eshelby's tensor [32-34]. The main deficiency of these methods is their failure in simulation of the complex structures. Moreover, when these semi-analytical approaches are applied to the elasto-plasticity analysis, too stiff mechanical responses are resulted [28, 32] and precise stress redistributions in an inelastic process cannot be captured by them [35]. Several attempts have been made to resolve this issue and to soften the mechanical responses, such as the mentioned "tangent" [30], "secant"[29, 36] and "affine" [35, 37] models.

- *Numerical solutions:* A direct approach in a multi-scale analysis is to model the real microstructural morphologies and apply their respective material constitutive equations to each of them. Computational cost and lack of the knowledge of the micro-scale constituent properties remain the main difficulties facing these methods. Using finite element approach in homogenization techniques for the periodic media [38] and Voronoi finite element method [39] compensate for the huge computational difficulties in simulation of such a fine microstructures. These methods are restricted by computational cost in large scale structural analysis.

- *Sequential approaches:* These methods lie between the two presented micromechanical based multi-scale approaches. The macroscopic constitutive equations are established from a multi-scale analysis performed on a discretized RVE. The mentioned overestimation of mechanical properties in analytical solutions has been addressed in the sequential approaches while the computational difficulties are resolved by proposing the macroscopic constitutive equations. The pioneering works done by Dvorak et al. resulted in *Transformation Field Analysis* (TFA) approach, which discretizes the exact solution of Lippman-Schwinger equation [1-3]. The TFA divides the local RVE into several sub-phases and, similar to the mean field micromechanical approach, uniform mechanical fields are assumed for each of sub-phases. Division of the RVE into several sub-phases forces the periodic media solution methodology in which the homogenization techniques with periodic boundary conditions are incorporated in order to obtain the required tensors. The advantage of this method is the possibility to incorporate Eshelby's analytical solutions for each sub-phase when their shapes follow the standard Eshelby's inclusion solutions such as ellipsoids, fibrous and penny shape sub-phases [1-3, 21]. Although the TFA approach takes into account the effect of the inelastic local fields and results in more accurate simulations, it still overestimates the mechanical responses. This issue has been addressed by Chaboche et al. who proposed a modification on the TFA model in which an isotopic hardening rule is incorporated to update the local tangent stiffness based on a hardening law [17, 28].

3.2.3 Contributions of the present work:

The TFA method is adopted here to link the crystalline and amorphous microstructural properties of a polyurethane based SMP to the macroscopic constitutive equations. Due to the large inelastic deformation of the polymeric based material systems, this approach is generalized here to take into account the finite strain deformations. It is worthwhile to indicate that classical continuum mechanics analysis does not count for the microstructural evolution and as a results it responds properly only for a specific type of loading while it fails to predict the material response subjected to different loading conditions [40-44]. On the other hand, once the macroscopic behavior is captured within a microscale based evolution, a generalized constitutive equation is obtained in which the material constants are independent of loading condition. Furthermore, such a multiscale analysis provides the material designers with the capability to predict the macroscale mechanical responses with knowledge of the micro-constituent properties.

The TFA method incorporates a number of ideal assumptions which may result in deviation of its simulation results from the experiments. For example its RVE consists of a matrix with limited number of the predefined inclusion shapes which are perfectly bounded together. Then this method cannot capture the real microstructures in which random inclusions with non-perfect bonding exist. These deficiencies may undermine the accuracy of such a micromechanical approach and it could be the source of stiffened macroscale mechanical responses [28]. To compensate for such deficiencies, the TFA method is modified in this work in which the experimental observations are incorporated in the TFA model and a series of softening empirical laws are derived. These laws provide enough flexibility for the designers to capture the irregular inelastic responses of glassy semicrystalline polymers.

In this work a generalized trivial two-phase TFA solution is then established for application to localized RVEs. In other words, a dilute heterogeneous media is assumed for constituting the macroscopic multiphase RVE. This multiphase RVE is then sub-divided into the local two-phase RVEs. Based on this methodology a novel computation scheme is introduced which is called *atomic* computation herein. While the classical two-phase TFA solution homogenizes the RVE into an equivalent media through averaging techniques [1], the proposed atomic computation provides a localized evaluation for non-linear phenomenon such as inelastic and damage processes. This computation approach consists of a hypothetical computational layer with specific arrangement of computational seeds. This hypothetical layer is assembled on the RVE where the generalized two-phase TFA solution identifies the local mechanical responses over that multi-phase RVE. In other words, *atomic* computation utilizes the generalized two-phase TFA solution to feed each of the computational seeds with necessary data. With this computational strategy, the micromechanics solution ensures that the basic solid mechanics equations, which are equilibrium, compatibility, strain-displacement and stress-strain relations, hold in the RVE. These permissible microscale strain and stress fields from the generalized two-phase TFA solution are then passed to the computational layer and subsequently to each of the computational seeds. Consequently, each of the computational seeds receives a localized loading condition and then they compute the localized inelastic strain or residual stress based on their respective governing constitutive equation. Such a localized analysis is crucial during a multiscale analysis where the designer needs to

investigate different damaging mechanisms. For example excessive damage or inelastic deformation in one of the sub-phases may results in local failures which can be in advance of the macroscopic failure. While these localized evaluations provide worthy information about local accumulated inelastic deformations or damages, they are hidden in the classical two-phase TFA solution in which homogenization or averaging approaches eliminate such localizations [1].

In section 2 of this work the finite deformation formulation approach is briefly presented. In section 3 the constitutive phases of a semicrystalline polymer are discussed, which are crystalline and amorphous phases. In section 4 the TFA method is elaborated and in section 5 the modified TFA is presented. In section 6 the computational aspect of the presented multi-scale finite deformation problem is discussed in detail. In section 7 the experimental and numerical results are presented with a detailed discussion on the performance of the presented micromechanical theory and the numerical algorithms. Here, indicial notations are utilized to denote tensorial quantities and lightface letters show the scalars.

3.3 Finite Deformation Kinematics

The formulation of an inelastic analysis within the finite deformation framework encounters with a considerable conjecture. A brief review is given here on available formulation approaches and finally the finite deformation kinematic of the interest is introduced. In general, during a finite strain deformation process the *material configuration* is deformed to *spatial configuration* as shown in Fig. 3-1. A basic kinematic assumption in the finite deformation context is to decompose the gradient of deformation multiplicatively. This is called *multiplicative decomposition* and proposed formerly by Lee [45-47]:

$$F_{ij} = F^e_{ik} F^p_{kj} \tag{3-1}$$

where F^e_{ij} is obtained through unloading the deformed body elastically in which an *intermediate configuration* is used to show this state as shown in Fig. 3-1(a) and F^p_{ij} is the plastic deformation gradient. More detailed description of this multiplicative decomposition concept can be found in [48]. This approach is amenable in the physical description of the polycrystalline large deformation. Additive decomposition of the total strain into the elastic and plastic components is another essential kinematic assumption in a large deformation elasto-plastic analysis. Additive decomposition of Lagrangian strain tensor d_{ij}, which is measured in the material configuration, has been adopted by Green and Naghdi [49] to describe the large deformation processes:

$$d_{ij} = d^e_{ij} + d^p_{ij} \tag{3-2}$$

where d^e_{ij} and d^p_{ij} are Lagrangian elastic and plastic strain tensors, respectively. Naghdi and Trapp [50] have shown that this additive decomposition follows the basic solid mechanics thermodynamic

framework. Another well-known approach is based on additive decomposition of Eulerian strain tensors D_{ij}, which is measured in the spatial configuration [51, 52]:

$$D_{ij} = D_{ij}^{e} + D_{ij}^{p} \tag{3-3}$$

where D_{ij}^{e} and D_{ij}^{p} are respectively Eulerian elastic and plastic strain tensors. Nemat-Nasser [53-55] and Green and Naghdi [56] have discussed these topics in details. The conjugate stresses to each configuration are described based on the strain measurements. The Cauchy stress tensor, σ_{ij}, which is defined as force per unit deformed area, is related to the spatial configuration (deformed body). Expressing stresses with respect to the material configuration is more convenient in continuum mechanics where the Cauchy stress tensor is transformed to obtain the *first Piola-Kirchhoff* stress tensor, τ_{ij}^{p}, which is defined as force per unit undeformed area. First Piola-Kirchhoff stress tensor is still allocated in spatial configuration (deformed body). If the first Piola-Kirchhoff stress is transferred to the material configuration then *second Piola-Kirchhoff* stress tensor, S_{ij}^{p}, is resulted. For a complete review on conjugate stresses see [57, 58]. Cauchy and first Piola-Kirchhoff stresses are conjugated with the Eulerian strain and second Piola-Kirchhoff stress is conjugated with the Lagrangian strain. Cauchy, first and second Piola-Kirchhoff stresses are obtainable from each other through application of *pull-back/push forward* method as discussed by Simo and Ortiz [59] .

An alternative description of the finite deformation kinematic is to decompose the deformation into the material, stretched and spatial configurations. In this context the polar decomposition of the deformation gradient tensor, F_{ij}, is utilize to decompose it into the rotational, R_{ij}, and stretching, U_{ij}, tensors as shown in Fig. 3-1(b) [57]:

$$F_{ij} = R_{ik} U_{kj} \tag{3-4}$$

The pull-back/push-forward approach is applicable for this decomposition to interchange the associated values with each configuration [52].

In this work, the polar decomposition is applied to each of the deformation gradients of the intermediate configuration in Fig. 3-1(a). In other words, the intermediate relaxed configuration can be represented by the polar decomposition of inelastic *right stretch tensor*, $U_{ij}^{p} = \left(F_{ik}^{p\,T} F_{kj}^{p}\right)^{1/2}$, and *proper orthogonal rotation* tensor, R_{ij}^{p}, as follows:

$$F_{ij}^{p} = R_{ik}^{p} U_{kj}^{p} \tag{3-1}$$

The eigenvalues of the symmetry and positive definite tensor U_{ij}^{p} are denoted by Λ_{i}^{p} which are called *principal inelastic stretches*. The deviation of Λ_{i}^{p} from unity measures the amount of inelastic strain.

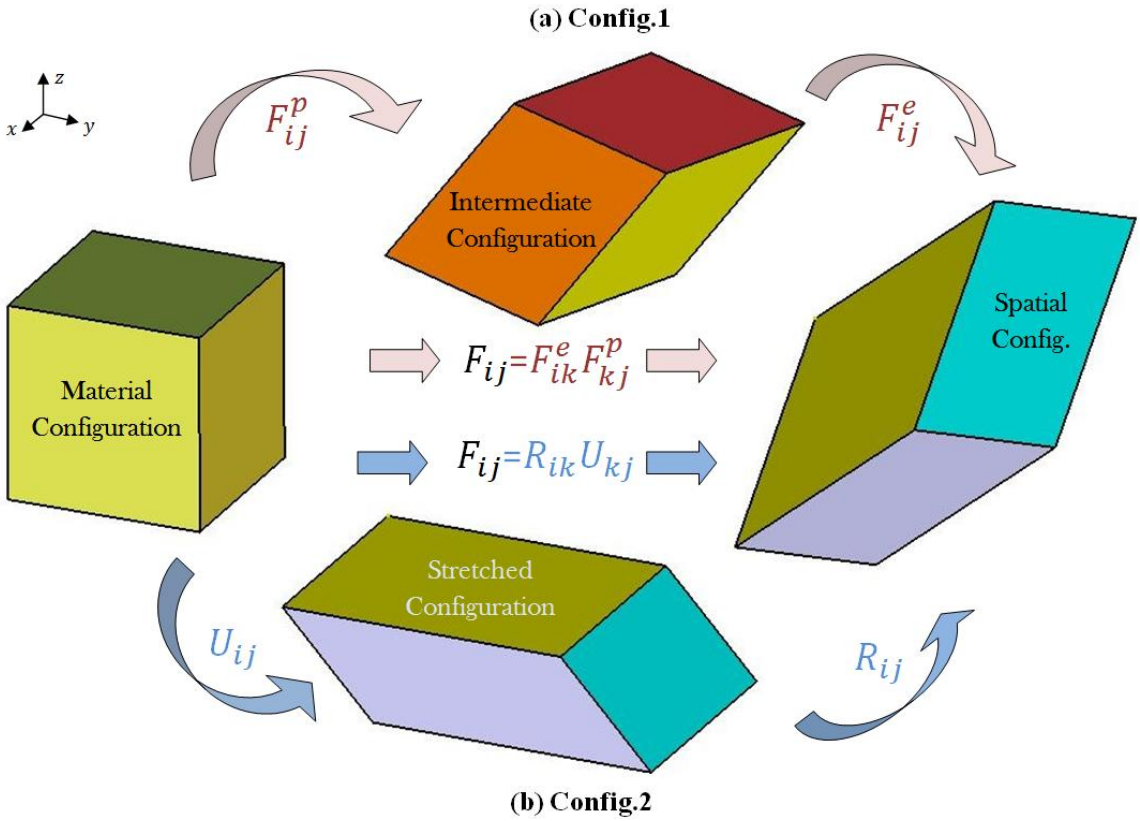

Figure 3-1 Schematic representation (a) intermediate and (b) polar decompositions in the finite deformation context

Furthermore, the polar representation of the transformation between the intermediate configuration and the spatial configuration is shown by:

$$F_{ij}^{e} = R_{ik}^{e} U_{kj}^{e} \tag{3-2}$$

It is assumed that the elastic gradient, F_{ij}^{e}, is only affected by the stretching process in this work and one may substitute $F_{ij}^{e} = U_{ij}^{e}$ in which $U_{ij}^{e} = \left({F_{ik}^{e}}^{T} F_{kj}^{e}\right)$ is the *elastic right stretch tensor*.

3.4 Semicrystalline characterization and constitutive equations

3.4.1 Semicrystalline characterization and constitutive equations:

As discussed in the introduction section, two distinctive micro-phases in the semicrystalline polymer-based systems, e.g. polyurethane SMP system, are distinguishable, i.e. amorphous and crystalline segments. The crystal phase is created during cooling down process of the melted polymer to the room temperature. This process results in the isotropic spherulite crystallographic morphology where the crystalline phase forms radial dark lamellae and the amorphous phase fills the space between these

layers [60, 61]. Upon inelastic deformation this spherulite morphology disappears and preferential crystalline orientation in the polymeric network is established within a layered microstructure [62]. In the produced crystalline networks, the chain segments are inextensible which implies that the inelastic deformation mechanisms cannot extend the crystalline chain [60]. Accordingly, the inelastic deformation of semicrystalline polymers involves three microstructural mechanisms: (a) change in crystallographic axis which is resulted from changes in crystalline texture, (b) change in orientation and arrangement of crystalline network which is referred as morphologic changes herein and (c) macromolecular alignment in amorphous phase. While many modeling efforts for simulating large inelastic deformation of semicrystalline polymers rely on ignoring amorphous phase and letting the crystalline phase represents the mechanical response including texture effects, experimental facts confirm the role of amorphous phase in the deformation process [63, 64]. In the case of semi-crystalline polyurethane elastomers once the yielding initiates the macromolecules in amorphous phase tend to align with their preferential orientations and crystallographic axes rotates with respect to the loading direction [65-67]. Composite formulations, to take into account the amorphous phase evolution beside crystallographic texture evolution have been proposed in the literature [65, 68-70]. A highly oriented layered semicrystalline microstructure was modeled by Takayanagi [71] who used a rheological description in which series element was utilized to account for the amorphous and crystalline phases and a parallel element is incorporated to account for crystalline links and tying the amorphous macromolecules between the layers. While the averaging schemes do not account for morphology, in the case of crystalline fibers, averaging approach for an oriented short fiber composite is adopted by Barham and Arridge [72] and the effective elastic modulus is introduced. In the following subsections, the constitutive equations for the amorphous and the crystalline phases are introduced. The micromechanical framework will correlate these individuals with the macroscale constitutive behaviors as shown in the next section. The texture and morphological updates are taken into account during an inelastic deformation analysis in this work.

3.4.2 Crystalline Phase:

The crystalline phase follows a few independent slip systems in which classical crystal plasticity theories (Taylor type ones) cannot be utilized to model them [60, 65, 69]. Similar to the metal like crystalline phases, inelastic deformation in polymeric systems follows three different mechanisms: (a) crystallographic slip, (b) twining and (c) Martensite transformations, in which two latest phenomenon are common in highly oriented polymeric networks [73]. All these mechanisms leave the crystallographic axis inextensible and provide less than five independent deformation modes to accommodate an inelastic deformation [65]. Here only slip mechanism is considered based on works done by Parks and coworkers [60, 65, 68]. Basically, a crystalline structure consists of a periodic unit cells where the same surrounding is maintained for all unit cells. The elastic deformation of a crystalline solid is associated with distortion of unit cells where the applied stress does not exceed the resistance of

interatomic bonds in a crystallographic network. Once the loading breaks these interatomic bonds, the permanent deformation is produced. In metals this permanent deformation is associated with the relative movement of atoms without change in unit cells conformations [57]. In a crystalline polymeric network this permanent deformation changes the crystallographic texture. A reference vector, c_i, coincides with crystalline chains and show the crystallographic texture. A schematic representation of an orthorhombic crystal system together with the lattice dimension for a high-density polyethylene (HDPE) crystalline system are shown by [60]. Two slip mechanisms can be active in a polymeric network slippage system: (a) chain slip where the burgers vector is aligned with c_i and (b) transverse slip where the burgers vector is perpendicular to c_i [60]. There are only four linearly independent crystalline slip systems indicated by unit vectors in the direction of slip and normal to the slip planes: (i) chain slip: (100)[001] and (010)[001], and (ii) transverse slip: (100)[010] and (010)[100] [60]. Minimum normalized resistance, between these four slips, shows the required stress to initiate the inelastic flow and this value is inserted to the computations. Let $s_i^{(\alpha)}$ denotes slip direction and $n_i^{(\alpha)}$ shows unit normal vector to the slip plane, where $\alpha = 1$ to 4 is the number of slip systems, the inelastic crystalline stretch rate tensor, $\dot{D}_{ij}^c$, is given by [60]:

$$\dot{D}_{ij}^c = \sum_{\alpha=1}^{K} \dot{\gamma}^{(\alpha)} R_{ij}^{(\alpha)} \tag{3-3}$$

where $\dot{\gamma}^{(\alpha)}$ is shear rate scalar variable, to be defined in the following, and $R_{ij}^{(\alpha)} = \frac{1}{2}\left\{s_i^{(\alpha)} n_j^{(\alpha)} + n_i^{(\alpha)} s_j^{(\alpha)}\right\}$ is called symmetric part of Schmid tensor and represents the αth crystalline system. The inextensibility of the crystalline chain together with the incompressibility assumption results in the following constraint relation:

$$\dot{D}_{ij}^c . C_{ij}^{'} = 0 \tag{3-4}$$

where $C_{ij}^{'} = c_i c_j - \frac{1}{3} I_{ij}$ is the deviatoric part of dyadic $c_i c_j$. The shear rate, $\dot{\gamma}^{(\alpha)}$, is defined as follows [31, 60, 74, 75]:

$$\dot{\gamma}^{(\alpha)} = \dot{\gamma}_0 \frac{\tau^{(\alpha)}}{g^{(\alpha)}} \left| \frac{\tau^{(\alpha)}}{g^{(\alpha)}} \right|^{n^c - 1} \tag{3-5}$$

where $g^{(\alpha)}$ is the shear strength for the α^{th} slip system, $\tau^{(\alpha)}$ represents the shear stress at the slippage system, $\dot{\gamma}_0$ is a reference shear rate and n^c is the rate sensitivity factor. One may utilize the following alternative for the shear stress:

$$\tau^{(\alpha)} = S_{ij}^{c} R_{ij}^{(\alpha)} \tag{3-6}$$

where $S_{ij}^{c} = \sigma_{ij}^{c} - \frac{1}{3}\sigma_{kk}^{c}\delta_{ij}$ is the deviatoric Cauchy stress in the crystalline phase. The deviatoric stress tensor, S_{ij}^{c}, can be decomposed into orthogonal tensor, S_{ij}^{cP}, and aligned tensor, S_{ij}^{c*}, projected with respect to the $C_{ij}^{'}$. In such a way the deviatoric stress tensor, S_{ij}^{c}, can be categorized based on the constraint Eq. (3-8). The resultant deviatoric stresses, S_{ij}^{cP}, aligned with the $C_{ij}^{'}$ cannot produce any inelastic deformation (due to constraint Eq. (3-8)) and only the remained part of deviatoric stress tensor, S_{ij}^{c*}, is in charge of producing the inelastic stretching. This fact is stated in the following [60]:

$$S_{ij}^{c} = S_{ij}^{c*} + S_{ik}^{cP} C_{kj}^{'} \tag{3-7}$$

Then instead of Eq. (3-10), one may conclude that the active shear stress in a inelastic deformation of the crystalline polymers is obtained as [60]:

$$\tau^{(\alpha)} = S_{ij}^{c*} R_{ij}^{(\alpha)} \tag{3-8}$$

The undetermined deviatoric stress component $\boldsymbol{S}^{cP}$ should be identified from equilibrium. The skew symmetry spin tensor, W_{ij}^{c}, is decomposed into inelastic spin, W_{ij}^{Ine}, and lattice spin, W_{ij}^{*}, additively [76]. The lattice spin which controls the rate of changes in direction of the crystallographic axes is introduced by [60, 76]:

$$\dot{W}_{ij}^{*} = \dot{W}_{ij}^{c} - \sum_{\alpha=1}^{K} \dot{\gamma}^{(\alpha)} A_{ij}^{(\alpha)} \tag{3-9}$$

where $A_{ij}^{(\alpha)} = \frac{1}{2}\left\{s_i^{(\alpha)} n_j^{(\alpha)} - n_i^{(\alpha)} s_j^{(\alpha)}\right\}$ is skew part of Schmid tensor and W_{ij}^{c} is the skew part of the velocity gradient L_{ij}^{c} in which $L_{ij}^{c} = D_{ij}^{c} + W_{ij}^{c}$.

3.4.3 Amorphous Phase:

The amorphous microstructure is constituted from random array of long molecular chains, called macromolecules hereinafter, which intersect to produce physical entanglements [77]. Both elastic and inelastic response of amorphous phase is affected by texture updates of macromolecules; however, inelastic process is much more sensitive to these texture changes [62]. The inelastic deformation of glassy polymers ($T < T_g$) initiates when applied stress overcomes the intermolecular resistance which restricts rotation of a chain segment individually or in a cluster [77, 78]. After initiation of inelastic flow chain segments aligns in the direction of principal inelastic deformations in which conformational entropic changes occur and result in a second source of resistance which is termed network resistance. Amorphous inelastic deformation is affected by the strain rate, pressure and temperature effects and they

often show a strain softening and subsequent strain hardening after initiation of the inelastic flow [40-44]. Argon proposed a rate dependent micro-mechanical inelastic theory based on a double kink formation and the intermolecular resistant, which is the free energy barrier to chain segment rotation [77]. Boyce and coworkers extended the Argon's viscoplastic element to a pressure, rate and temperature dependent theory which is based on modeling the intermolecular energy barriers [62, 78-81]. This theory is outlined in the following and it is utilized to model the inelastic deformation of the amorphous phase of a semicrystalline polymer-based material system. The plastic multiplier is introduced as follows [62]:

$$|\dot{\gamma}^p| = \dot{\gamma}_0 \exp\left[-A\,\frac{s + a\,p}{\Theta}\left(1 - \left(\frac{|\tau|}{s + a\,p}\right)^{5/6}\right)\right] \tag{3-10}$$

with

$$A = \frac{39\pi\omega^2\bar{a}^3}{16k} \tag{3-11}$$

where ω is the net angle of rotation between active and initial molecular segment configurations and $\bar{a}$ is the mean molecular radius and k is the Boltzmann's constant [77]. The material constant $\dot{\gamma}_0$ is called pre-exponential inelastic strain rate, and $|\dot{\gamma}^p|$ is the effective equivalent inelastic deformation rate of a glassy polymer subjected to effective equivalent shear stress, $|\tau|$, to be defined at absolute temperature, Θ, in the following. Linear dependency of peak shear yield strength on pressure is introduced by pressure coefficient a and $p = -\frac{1}{3}tr(\sigma_{ij})$ is the hydrostatic pressure in Eq. (3-14). Phenomenological relation for *athermal shear strength,* s, which takes into account the pressure, rate and temperature dependency and the strain softening effect, has been proposed by Boyce et al. [62, 78] as follows:

$$\dot{s} = h\left(1 - \frac{s}{s_{ss}(\Theta, |\dot{\gamma}^p|)}\right)|\dot{\gamma}^p| \tag{3-12}$$

where h is the rate of drop with respect to the inelastic deformation rate to incorporate the strain softening and s_{ss} represents the asymptotic *preferred structure*. The initial value of s for the annealed material is: $s_0 = \frac{0.077\mu}{1-\nu}$ where μ is the elastic shear modulus and ν is the Poisson's ratio.

Back stress tensor, α_{ij}, has been defined by Boyce and coworkers [82-84] and is defined here as:

$$\alpha_{ij} = nk\Theta\,\frac{\lambda^L}{3}\left[\lambda_i^p\,\mathcal{L}^{-1}\left(\zeta\,\frac{\lambda_j^p}{\lambda^L}\right) - \frac{1}{3}\lambda_k^p\,\mathcal{L}^{-1}\left(\zeta\,\frac{\lambda_k^p}{\lambda^L}\right)\delta_{ij}\right] \tag{3-13}$$

where n is the number of chains per unit volume, k is the Boltzmann's constant, and λ^L is the limit of chain extensibility which shows the inelastic deformation cannot exceed this limiting value ($\lambda_i^p \le \lambda^L$) where further macroscopic inelastic deformation may monitor the chain breakage and ζ is a viscoplastic related material constant which controls the magnitude of hardening with regard to the inelastic stretches.

In limit analysis Langevin function, $L(\beta) = \coth(\beta) - 1/\beta$, is used extensively and it imposes a limiting case in evolution of back stress tensor in which $\left|\lambda_i^p\right| \ll 0$ results in $\alpha_{ij} \cong \emptyset_{ij}$ where $\emptyset_{ij}$ is the second rank zero tensor. Furthermore, $\left|\lambda_i^p\right| = \lambda^L$ yields $\alpha_{ij} \gg I_{ij}$, where I_{ij} is the second rank unity tensor, and produces an extreme network resistance to the inelastic deformation and models the hardening. The driving stress state for producing inelastic deformation is given by: $s_{ij}^* = s_{ij} - X_{ij}$ in which $X_{ij} = \alpha_{ij} - \frac{1}{3}\alpha_{mm}\,\delta_{ij}$ is the back stress tensor, resulted from entropic resistance and $s_{ij} = \sigma_{ij} - \frac{1}{3}\sigma_{kk}\,\delta_{ij}$ is the deviatoric Cauchy stress. The effective shear stress is obtained as the norm of driving stress as follows:

$$|\tau| = \sqrt{\frac{1}{2}s_{ij}^*\,s_{ij}^*} \tag{3-14}$$

The viscous element in Eq. (3-14) represents the magnitude of the amorphous inelastic shear strain rate; while the direction of the inelastic flow is governed by the deviatoric driving stress as stated in the following flow rule [77]:

$$D_{ij}^p = |\dot{\gamma}^p|\frac{s_{ij}^*}{\sqrt{2}|\tau|} \tag{3-15}$$

3.4.4 Morphological texture updates:

In this work the effect of changes in the texture for the amorphous and crystalline phases and changes in the morphological texture for the whole semicrystalline structure are taken into account as discussed in the following.

(i) Amorphous phase: In the case of the amorphous phase the tensile tests of oriented amorphous polymers reveal that the yield stress is strongly affected by the initial texture. Effect of initial texture and preorientation has been considered on the two intermolecular and molecular alignment resistance mechanisms by Boyce et al. [78]. It is common to neglect the texture effect in a elastic deformation and consider it only during an inelastic deformation by incorporating initial values for the back stress tensor, α_{ij}, athermal shear resistance, s, network stretch vector, Λ_i, and residual stress tensor, σ_{ij} [62]. The preorientation effect may not be induced only by inelastic deformations, for example spinning or other manufacturing processes may produce preferential texture. Here the texture effect is modeled by introducing an initial inelastic deformation into the back stress evolution law and the initial value of the back stress is obtained.

(ii) Crystalline phase: In the case of crystalline phase, the crystallographic texture is updated by taking into account the changes in the crystallographic axes which is given by the following rate equation [76]:

$$\dot{c}_i = W_{ij}^* c_j \tag{3-16}$$

Eq. (3-20) captures the change in the crystallographic axis regarding lattice spins. The incremental form of Eq. (3-20) is given by [60]:

$$c_i(t+\Delta t) = \exp\left(W_{ij}^* \Delta t\right) c_j(t) \tag{3-17}$$

Based on the Cayley-Hamilton expression for exponential term, one may find [60]:

$$\exp\left(W_{ij}^* \Delta t\right) = I_{ij} + \frac{\sin w}{w} W_{ij}^* \Delta t + \left(\frac{1-cosw}{w^2}\right) W_{ik}^* W_{kj}^* \Delta t^2 \tag{3-18}$$

with $w^2 = -tr\left(W_{ik}^* W_{kj}^* \Delta t^2\right)/2$.

(iii) Morphological texture: The morphological texture in the semicrystalline polymeric system is updated based on changes in the directions of the unit outer normal vectors to the interfaces, n_i^I, which is computed according to the changes in the material coordinate system at interface. Let the material coordinate system at the interface plane be indicated by two infinitesimal independent vectors, δx_i and δx_j at time $t = 0$. At generic time t, these vectors are transformed respectively to the $F_{ij}(t)\delta x_i$ and $F_{ij}(t)\delta x_j$ where $F_{ij}(t)$ is the deformation gradient. Then the following expression for the normal vector n_i^I is trivial:

$$n_k^I(0) = \frac{\delta x_i^{(1)} \times \delta x_j^{(2)}}{\left|\delta x_i^{(1)} \times \delta x_j^{(2)}\right|} \tag{3-19}$$

$$n_k^I(t) = \frac{F_{ij}(t)\delta x_j^{(1)} \times F_{ij}(t)\delta x_i^{(2)}}{\left|F_{ij}(t)\delta x_i^{(1)} \times F_{ij}(t)\delta x_j^{(2)}\right|} \tag{3-20}$$

The deformation gradient is updated based on the rate equation, $\dot{F}_{ij} = L_{ik} F_{kj}$, which is converted into the following incremental form:

$$F_{ij}(t+\Delta t) = \exp(L_{ik}\Delta t)\, F_{kj}(t) \tag{3-21}$$

The deformation compatibility at the interface implies that the gradient deformation tensors of each phase can be used in Eq. (3-25). To take into the account the molecular alignment in the amorphous phase, the deformation gradient of the amorphous phase is incorporated as follows:

$$F_{ij}^{a}(t+\Delta t) = \exp(L_{ik}^{a}\Delta t)\, F_{kj}^{a}(t) \qquad (3\text{-}22)$$

Basically the updated interfacial vector, n_i^I, renders the movement and rotation of the inclusion inside the RVE. This allows designers to update the morphology of the RVE based on the deformation gradient during a finite strain deformation process. Eqs. (25) and (26) will be utilized in coupling with the micromechanical formulations to investigate the effect of loading on the RVE configuration where n_i^I is updated based on deformation gradients and enforcing compatibility in the deformation field. Of course the bonding between inclusion and matrix is assumed to be perfect.

Up to now, the constitutive equations for the individual constituents are introduced and the texture update procedures for the amorphous, crystalline and the semicrystalline structure are established. Next step is to establish the interaction laws between these micro-constituents and develop the macroscopic constitutive equation based on the knowledge of the microscale deformation mechanisms. This is accomplished within the micromechanical framework and the process is discussed in the next section.

3.5 Micromechanics

In the micromechanic framework two approaches are widely incorporated to relate the overall macroscale properties of a heterogeneous media to the local microscale properties. The Representative Volume Element (RVE) concept bridges the local and overall properties within introduction of a volumetric element which contains a certain number of microscale phases. In this concept the heterogeneity characterization depends on the length scales, and the length scale of an RVE is selected in such a way that contains enough micro-phases to represent the overall macrostructure of the heterogeneous media. The second approach is the periodic *unit cell* method which utilizes periodic boundary conditions to tessellate a macroscale problem with the unit cells. In either methods the overall macroscopic properties are obtained through assumption of macroscopically uniform overall Cauchy stress field, $\sigma_{ij}(t)$, and uniform overall macroscopic strain field, $\epsilon_{ij}(t)$; where t represents time. When the RVE approach is adopted, these uniform macroscopic fields are obtained through imposing compatible boundary conditions on the phase interfaces. In the case of the unit cell method, certain periodic boundary conditions are required to reproduce such uniform macroscopic fields. The mechanical responses of the microscale phases and macroscale RVE are then correlated with specific transformation tensors, i.g. concentration tensors. The main difficulty arose when non-linearity, such as inelastic deformation, is introduced in one or some of the microscale phases.

Inelastic strains and relaxed stresses during an inelastic process are termed respectively as eigenstrains and eigenstresses herein, which implicates that these residual fields cannot be recovered after elastic

unloading. The transformation tensors between the local uniform eigenvalues and the macroscale responses are obtained through *transformation influence functions* or *concentration factors*; in which, self-consistent, Mori-Tanaka or unit-cell approaches are utilized to approximate them. Since all of the micromechanical approximation schemes for the local-overall relations rely on the local and overall thermo-elastic moduli, once the elasticity solution is obtained the solution to this part of problem is trivial [21].

Due to the nature of the inelastic deformation, a history dependent solution algorithm is required in order to take into account the load history effect. TFA method provides an incremental solution of uniform thermomechanical loading condition for inelastic analysis of such a heterogeneous media. This approach evaluates the elasto-plastic responses of a material system based on the geometry and mechanical properties of its microscale constituents and it is applicable to any plasticity or viscoplasticity constitutive equation which has been formulated in the additive decomposition of the inelastic and elastic strains [2, 3]. While each of the microscale phases may undergo non-homogeneous inelastic deformation, the TFA method assumes explicit piecewise uniform residual fields over these phases.

In this work the RVE representation is adopted where the microscale phases are defined through dividing the macroscopic RVE into sub-volumes, $V^{(r)}$ with $r = 1,2,\dots,N$ where N is the number of phases in the RVE. The macroscopic properties are indicated by: fourth order elastic stiffness tensor, L_{ijkl}, fourth order compliance tensor, M_{ijkl}, second order eigenstrain tensor, $\mu_{ij}(t)$, and second order eigenstress tensor, $\aleph_{ij}(t)$. The microscopic properties associated with the rth sub-volume, $V^{(r)}$, are indicated by: stiffness tensor, $L_{ijkl}^{(r)}$, compliance tensor, $M_{ijkl}^{(r)}$, eigenstrain tensor, $\mu_{ij}^{(r)}(x,t)$, and eigenstress tensor, $\aleph_{ij}^{(r)}(x,t)$, where x represents dependency on the coordinate system and t shows the time dependency. The macroscopic eigenstress tensor, $\lambda_{ij}(t)$, and macroscopic eigenstrain tensor, $\mu_{ij}(t)$, should be uniform to result in a uniform overall stress, $\sigma_{ij}(t)$, and strain, $\epsilon_{ij}(t)$, which is one of the primary assumption in the TFA theory. Then the local eigenstress $\aleph_{ij}^{(r)}(x,t)$ and eigenstrain $\mu_{ij}^{(r)}(x,t)$ over the rth sub-phase are constrained to produce such a macroscopic uniform field. The additive decomposition of the elastic and inelastic strains identifies the macroscopic constitutive relation for an RVE as follows [2, 3]:

$$\sigma_{ij}(t) = L_{ijkl}\,\epsilon_{kl}(t) + \aleph_{ij}(t), \qquad \epsilon_{ij}(t) = M_{ijkl}\,\sigma_{kl}(t) + \mu_{ij}(t) \tag{3-23}$$

where $\aleph_{ij}(t) = -L_{ijkl}\,\mu_{kl}(t)$. Additive decomposition of the elastic and inelastic strains holds during developing the microscale constitutive equations in the rth sub-phase as follows [2]:

$$\begin{aligned} \sigma_{ij}^{(r)}(x,t) &= L_{ijkl}^{(r)}\,\epsilon_{kl}^{(r)}(x,t) + \aleph_{ij}^{(r)}(x,t), \\ \epsilon_{ij}^{(r)}(x,t) &= M_{ijkl}^{(r)}\,\sigma_{kl}^{(r)}(x,t) + \mu_{ij}^{(r)}(x,t) \end{aligned} \tag{3-24}$$

where $\sigma_{ij}^{(r)}(x,t)$ and $\epsilon_{ij}^{(r)}(x,t)$ are local distribution of stress and strain tensors over the rth sub-phase. Eqs. (3-27) and (3-28) represent an additive conformation of eigenvalues with their respective elastic values regardless of the origin of the eigenvalues (eigenvalues may be originated from the inelastic deformation, damaging mechanisms or other source of non-linearity). Each sub-phase may follow a certain constitutive equation which provides $\sigma_{ij}^{(r)}(x,t)$ and $\epsilon_{ij}^{(r)}(x,t)$ at any time. It is worthy of noting that during the assembling of these local fields, they should conform to the overall compatibility condition and global equilibrium. Here eigenfields are considered to be originated only in the inelastic and thermal processes:

$$\begin{aligned} \aleph_{ij}^{(r)}(x,t) &= \sigma_{ij}^{(r)^{Res}}(x,t) + \sigma_{ij}^{(r)^{Thr}}(x,t) \\ \mu_{ij}^{(r)}(x,t) &= \epsilon_{ij}^{(r)^{Ine}}(x,t) + \epsilon_{ij}^{(r)^{Thr}}(x,t) \end{aligned} \tag{3-25}$$

Local inelastic strain, $\epsilon_{ij}^{(r)^{Ine}}(x,t)$, or local residual stress, $\sigma_{ij}^{(r)^{Res}}(x,t)$ in the rth sub-phase are given by the inelastic constitutive equations of the rth phase. The local thermal strain, $\epsilon_{ij}^{(r)^{Thr}}(x,t)$, and thermal stress, $\sigma_{ij}^{(r)^{Thr}}(x,t)$, in the rth sub-phase are obtained through linear thermal expansion coefficient tensors. Substituting Eq. (3-29) into Eq. (3-28) results in the following stress and strain decompositions which are recasts of the additive strain decomposition into the elastic, inelastic and thermal stresses/strains:

$$\begin{aligned} \sigma_{ij}^{(r)}(x,t) &= L_{ijkl}^{(r)}\epsilon_{kl}^{(r)}(x,t) + \sigma_{ij}^{(r)^{Res}}(x,t) + \sigma_{ij}^{(r)^{Thr}}(x,t), \\ \epsilon_{ij}^{(r)}(x,t) &= M_{ijkl}^{(r)}\sigma_{kl}^{(r)}(x,t) + \epsilon_{ij}^{(r)^{Ine}}(x,t) + \epsilon_{ij}^{(r)^{Thr}}(x,t) \end{aligned} \tag{3-26}$$

In the context of micromechanics the fields containing eigenvalues are transformed into an equivalent elastic media and then trivial elastic solutions are obtained for local-overall transformation tensors [21]. In the case of zero eigenstrains and eigenstresses, the stress, $B_{ijkl}^{(r)}(x)$, and strain, $A_{ijkl}^{(r)}(x)$, concentration tensors are utilized to relate the macro- and micro-scale stress-strain fields as follows [2]:

$$\begin{aligned} \sigma_{ij}^{(r)}(x,t) &= B_{ijkl}^{(r)}(x)\sigma_{kl}(t) + b_{ij}^{(r)}(x)\theta(t), \\ \epsilon_{ij}^{(r)}(x,t) &= A_{ijkl}^{(r)}(x)\epsilon_{kl}(t) + a_{ij}^{(r)}(x)\theta(t) \end{aligned} \tag{3-27}$$

where $b_{ij}^{(r)} = \sum_{S=1}^{N} F_{ijkl}^{(rs)} l_{kl}^{(s)}$ and $a_{ij}^{(r)} = \sum_{S=1}^{N} D_{ijkl}^{(rs)} m_{kl}^{(s)}$ are respectively thermal stress and strain transformation tensors and θ represents the uniform temperature changes. Besides, $F_{ijkl}^{(rs)}$ and $D_{ijkl}^{(rs)}$ are

eigenstress and eigenstrain influence function tensors, respectively. And $l_{ij}^{(s)}$ and $m_{ij}^{(s)}$ denote respectively the thermal stress and strain tensors. Dvorak et al. extended Eq. (3-31) for the case of nonzero eigenvalues as follows [1]:

$$\begin{aligned}\sigma_{ij}^{(r)}(x,t) &= B_{ijkl}^{(r)}(x)\sigma_{kl}(t) + \sum_{s=1}^{N} F_{ijkl}^{(sr)}(x)\left(\aleph_{kl}^{(s)}(t) + l_{kl}^{(s)}\theta(t)\right) \\ \epsilon_{ij}^{(r)}(x,t) &= A_{ijkl}^{(r)}(x)\epsilon_{kl}(t) + \sum_{s=1}^{N} D_{ijkl}^{(sr)}(x)\left(\mu_{kl}^{(s)}(t) + m_{kl}^{(s)}\theta(t)\right)\end{aligned} \tag{3-28}$$

Eq. (3-32) takes into account the contribution of three sources of effect on the local behavior including, (i) *elastic field effect*: this effect is induced by the elastic changes in the rth sub-phase. The strain, $A_{ijkl}^{(r)}(x)$, and stress concentration, $B_{ijkl}^{(r)}(x)$, tensors are responsible to capture this effect. (ii) *adjacent non-linear field effect*: the residual fields in the neighboring sub-phases ($r \neq s$) may affect the local mechanical response of the rth sub-phase. It is captured by eigenfields influence tensors, $F_{ijkl}^{(sr)}(x)$ and $D_{ijkl}^{(sr)}(x)$, (iii) *self-residual field effect:* the influence of self-residual fields ($r = s$) are captured by eigenfields influence tensors, $F_{ijkl}^{(ss)}(x)$ and $D_{ijkl}^{(ss)}(x)$. Local strain, $\epsilon_{ij}^{(r)}(x,t)$, and stress, $\sigma_{ij}^{(r)}(x,t)$, fields in Eq. (3-32) are connected to the overall strain, $\epsilon_{ij}(t)$, and stress, $\sigma_{ij}(t)$, fields through averaging techniques as indicated in the following:

$$\begin{aligned}\epsilon_{ij}(t) &= \frac{1}{V}\int_{V} \epsilon_{ij}^{(r)}(x,t)dV, \\ \sigma_{ij}(t) &= \frac{1}{V}\int_{V} \sigma_{ij}^{(r)}(x,t)dV\end{aligned} \tag{3-29}$$

As discussed by Dvorak et al., the local eigenvalues tensors $\aleph_{ij}^{(r)}(x,t)$ and $\mu_{ij}^{(r)}(x,t)$ are respectively related to the overall piecewise uniform macroscopic eigenvalues tensors of $\aleph_{ij}^{(r)}(t)$ and $\mu_{ij}^{(r)}(t)$ by the generalized Levin formula [2]:

$$\begin{aligned}\aleph_{ij}(t) &= \frac{1}{V}\int_{V} \left(A_{ijkl}^{(r)}(x)\right)^{T} \lambda_{kl}^{(r)}(x,t)dV, \\ \mu_{ij}(t) &= \frac{1}{V}\int_{V} \left(B_{ijkl}^{(r)}(x)\right)^{T} \mu_{kl}^{(r)}(x,t)dV\end{aligned} \tag{3-30}$$

where superscript T indicates the transpose of the corresponding tensors. In practice specific geometries are assumed for each of sub-phases in order to imply homogeneous deformation regimes on each of the sub-phases and then all of the continuous strain-stress fields in Eq. (3-33) and (3-34) can be substituted by piecewise uniform approximations. Moreover, $A_{ijkl}^{(r)}(x)$ and $B_{ijkl}^{(r)}(x)$ are averaged over the rth sub-phase to result in $A_{ijkl}^{(r)}$ and $B_{ijkl}^{(r)}$. Eqs. (3-33) and (3-34) are reproduced by applying these modifications to obtain the following expressions [1-3]:

$$\begin{aligned} \epsilon_{ij}(t) &= \sum_{r=1}^{N} c^{(r)} \epsilon_{ij}^{(r)}(t), \qquad \sigma_{ij}(t) = \sum_{r=1}^{N} c^{(r)} \sigma_{ij}^{(r)}(t) \\ \aleph_{ij}(t) &= \sum_{r=1}^{N} c^{(r)} \left(A_{ijkl}^{(r)}\right)^{T} \aleph_{kl}^{(r)}(t), \qquad \mu_{ij}(t) = \sum_{r=1}^{N} c^{(r)} \left(B_{ijkl}^{(r)}\right)^{T} \mu_{kl}^{(r)}(t) \end{aligned} \tag{3-31}$$

where $c^{(r)} = V^{(r)}/V$ is the volume fraction. By replacing the continuous influence functions $D_{ijkl}^{(rs)}(x)$ and $F_{ijkl}^{(rs)}(x)$ by their respective volumetric averaged values, $D_{ijkl}^{(rs)}$ and $F_{ijkl}^{(rs)}$, over the rth sub-phase, Eq. (3-32) reduces to:

$$\begin{aligned} \sigma_{ij}^{(r)}(t) &= B_{ijkl}^{(r)} \sigma_{kl}(t) + \sum_{s=1}^{N} F_{ijkl}^{(sr)} \left(\aleph_{ij}^{(r)}(t) + l_{kl}^{(r)} \theta(t)\right) \\ \epsilon_{ij}^{(r)}(t) &= A_{ijkl}^{(r)} \epsilon_{kl}(t) + \sum_{s=1}^{N} D_{ijkl}^{(sr)} \left(\mu_{ij}^{(r)}(t) + m_{kl}^{(r)} \theta(t)\right) \end{aligned} \tag{3-32}$$

where inelastic constitutive laws relates the local inelastic strains to the history of loading, i.g. $\mu_{ij}^{(r)}(t) = f\left(\sigma_{ij}^{(r)}(t)\right)$. The residual fields are always related by elastic modulus through, $\aleph_{ij}^{(r)} = -L_{ijkl}^{(r)} \mu_{kl}^{(r)}$. Finally, the inelastic solution for a multiphase material system is reduced to evaluation of mechanical concentration tensors, A_{ijkl} and B_{ijkl}, and eigenfields influence tensors, D_{ijkl} and F_{ijkl}. All of these tensors are functions of local and overall thermo-elastic moduli and also history of loading, which is enforced by integration of the local inelastic constitutive equations. The mechanical concentration tensors are obtained through micromechanical models for elastic media and eigenfields influence tensors are computed as illustrated by Dvorak et al. [2, 3]. In general the eigenstrain influence function, $F_{ijkl}^{(rs)}$, and eigenstress influence function, $D_{ijkl}^{(rs)}$, are computed from the following properties as shown by Dvorak et al. [1, 3]:

$$\begin{aligned}
\sum_{r=1}^{N} D_{ijkl}^{(rs)} &= I_{ijkl} - A_{ijkl}^{(s)}, \\
\sum_{r=1}^{N} F_{ijkl}^{(rs)} &= I_{ijkl} - B_{ijkl}^{(s)}, \\
\sum_{r=1}^{N} D_{ijkl}^{(rs)} M_{klij}^{(r)} &= 0, \\
\sum_{r=1}^{N} F_{ijkl}^{(rs)} L_{klij}^{(r)} &= 0.
\end{aligned} \tag{3-33}$$

The set of equations (37_1) and (37_3) (or (37_2) and (37_4)) provides $2 \times N$ independent equations while there are $N \times N$ unknown. It is clear that for a multiphase system with $N > 2$ exact relation between influence functions and related material properties cannot be derived analytically. Then the solution of a multiphase media with $N > 2$ includes the interaction evaluation for each sub-phases under eigenstrain loading. In other words, each specific microstructure is taken into consideration while their geometry and eigenstrain are involved into the calculations. However, in the case of a two phase material system the analytical solution results in the following relations, which relate the $D_{ijkl}^{(rs)}$ to the material properties [3, 28]:

$$\begin{aligned}
D_{ijkl}^{(11)} &= \left(I_{ijmn} - A_{ijmn}^{(1)}\right)\left(L_{mnzx}^{(1)} - L_{mnzx}^{(0)}\right)^{-1} L_{zxkl}^{(1)} \\
D_{ijkl}^{(10)} &= \left(I_{ijmn} - A_{ijmn}^{(1)}\right)\left(L_{mnzx}^{(0)} - L_{mnzx}^{(1)}\right)^{-1} L_{zxkl}^{(0)}
\end{aligned} \tag{3-34}$$

where superscript 0 indicates matrix and 1 indicates the inclusion phase. Then in a two phase material system the analysis can be reduced to a mechanical loading problem. For a three phase material system following relations between transmitted and self-induced influence functions are derived by solving the system of equations (37_1) and (37_3):

$$\begin{aligned}
D_{ijkl}^{(12)}\left(M_{klpq}^{(2)} - M_{klpq}^{(3)}\right) &= D_{ijkl}^{(11)}\left(M_{klpq}^{(3)} - M_{klpq}^{(1)}\right) - \left(I_{ijkl} - A_{ijkl}^{(1)}\right)M_{klpq}^{(3)} \\
D_{ijkl}^{(13)}\left(M_{klpq}^{(3)} - M_{klpq}^{(2)}\right) &= D_{ijkl}^{(11)}\left(M_{klpq}^{(2)} - M_{klpq}^{(1)}\right) - \left(I_{ijkl} - A_{ijkl}^{(1)}\right)M_{klpq}^{(2)} \\
D_{ijkl}^{(21)}\left(M_{klpq}^{(1)} - M_{klpq}^{(3)}\right) &= D_{ijkl}^{(22)}\left(M_{klpq}^{(3)} - M_{klpq}^{(2)}\right) - \left(I_{ijkl} - A_{ijkl}^{(2)}\right)M_{klpq}^{(3)} \\
D_{ijkl}^{(23)}\left(M_{klpq}^{(3)} - M_{klpq}^{(1)}\right) &= D_{ijkl}^{(22)}\left(M_{klpq}^{(1)} - M_{klpq}^{(2)}\right) - \left(I_{ijkl} - A_{ijkl}^{(2)}\right)M_{klpq}^{(1)} \\
D_{ijkl}^{(31)}\left(M_{klpq}^{(1)} - M_{klpq}^{(2)}\right) &= D_{ijkl}^{(33)}\left(M_{klpq}^{(2)} - M_{klpq}^{(3)}\right) - \left(I_{ijkl} - A_{ijkl}^{(3)}\right)M_{klpq}^{(2)} \\
D_{ijkl}^{(32)}\left(M_{klpq}^{(2)} - M_{klpq}^{(1)}\right) &= D_{ijkl}^{(33)}\left(M_{klpq}^{(1)} - M_{klpq}^{(3)}\right) - \left(I_{ijkl} - A_{ijkl}^{(3)}\right)M_{klpq}^{(1)}
\end{aligned} \tag{3-35}$$

where the knowledge of self-induced inelastic influence for each inclusion is required to reduce the problem to a mechanical loading case. Now the self-consistent or Mori-Tanaka estimations may be utilized to derive the stress and strain concentration factors. The overall stiffness and compliance for a multiphase media are obtained as [2, 3, 21]:

$$\begin{aligned} L_{ijkl} &= L^{(0)}_{ijkl} + \sum_{r=2}^{N} c^{(r)}\left(L^{(r)}_{ijmn} - L^{(0)}_{ijmn}\right)A^{(r)}_{mnkl} \\ M_{ijkl} &= M^{(0)}_{ijkl} + \sum_{r=2}^{N} c^{(r)}\left(M^{(r)}_{ijmn} - M^{(0)}_{ijmn}\right)B^{(r)}_{mnkl} \end{aligned} \tag{3-36}$$

The self-consistent or Mori-Tanaka estimations result in following form of strain, $A^{(r)}_{ijkl}$, and stress, $B^{(r)}_{ijkl}$, concentration tensors [2, 3]:

$$\begin{aligned} A^{(r)}_{ijkl} &= \left(L^{*}_{ijmn} + L^{(r)}_{ijmn}\right)^{-1}\left(L^{*}_{mnkl} + L_{mnkl}\right) \\ B^{(r)}_{ijkl} &= \left(M^{*}_{ijmn} + M^{(r)}_{ijmn}\right)^{-1}\left(M^{*}_{mnkl} + M_{mnkl}\right) \end{aligned} \tag{3-37}$$

Here $L^{*}_{ijkl} = \left(M^{*}_{ijkl}\right)^{-1}$ denotes Hill's ellipsoidal inclusion transformation constraint tensor [30]. The difference between self-consistent and Mori-Tanaka approximations arise from their approach to compute constraint tensor L^{*}_{ijkl}. Self-Consistent (SC) method incorporates the effective overall stiffness tensor L_{ijkl}, while Mori-Tanaka (MT) utilizes the matrix stiffness tensor $L^{(0)}_{ijkl}$ in the evolution equation of L^{*}_{ijkl} as shown below [2, 3]:

$$\begin{aligned} SC \rightarrow\ L^{*}_{ijkl} &= L_{ijmn}\left(I_{mnzx} - S_{mnzx}\right)S^{-1}_{zxkl} \\ MT \rightarrow\ L^{*}_{ijkl} &= L^{(0)}_{ijmn}\left(I_{mnzx} - S_{mnzx}\right)S^{-1}_{zxkl} \end{aligned} \tag{3-38}$$

where S_{ijkl} is the Eshelby tensor for different inclusion types as given in Appendix A.

3.6 Modified Two-phase TFA approach

The TFA solution for a two-phase media is trivial which leads to derivation of constitutive equation for the two-phase RVE with uniform microscale strain and stress distribution. This two-phase RVE cannot be utilized for evaluating complex microstructures and the resultant uniform microscale stress and strain

fields cannot identifies the localized effects of non-linear processes. Furthermore, the performance of the two-phase TFA method is undermined with too simplified assumptions during the composition of its RVE where the actual microstructure of the material systems cannot be predicted accurately with this simple RVE composition. For example, chemical induced crystallization process in polymers results in spherulite crystalline structures surrounded with amorphous phases as shown by [61]. The magnitude and size of crystalline domains are functions of temperature and many other physical and chemical conditions while the crystalline morphology and size may vary under applied stress. Then in the reality the microstructural texture of crystalline and amorphous phases in a semicrystalline polymeric material system is too complicated to be estimated with a simplified two-phase RVE. To render the nature of the material systems, some additional data from the experimental results has been incorporated into the TFA formulation while the trivial two-phase solution is generalized for a dilute heterogeneous material system. In the following the steps for upgrading the two-phase TFA solution are elaborated:

- Softening the TFA responses:

Accordingly the TFA micromechanical formulation underestimates the overall eigenstrain, μ_{ij}, during a strain-controlled loading condition or eigenstress, $\aleph_{ij}$, during a stress-controlled loading condition and consequently it results in too stiff stress-strain responses during an elasto-inelastic analysis. Chaboche et al. [17, 28] addressed this overestimation of mechanical responses during analysis of a metal matrix composite and he proposed a modification on the TFA model where the inelastic tangent stiffness is used to soften the mechanical responses. In this work two material parameters functions, $\chi^{(r)}\left(c^{(r)}\right)$ and $\chi'^{(r)}\left(c^{(r)}\right)$, are introduced in order to soften TFA. These parameters are captured from experimental results and they show an effective role on adjustment of the micromechanical simulations with the experimental results. The original TFA formulation is then modified in the following way:

$$\aleph_{ij}(t) = \sum_{r=1}^{N} c^{(r)}\left(A_{ijkl}^{(r)}\right)^{T} \chi'^{(r)} \aleph_{kl}^{(r)}(t),$$
$$\mu_{ij}(t) = \sum_{r=1}^{N} c^{(r)}\left(B_{ijkl}^{(r)}\right)^{T} \chi^{(r)} \mu_{kl}^{(r)}(t) \qquad (3\text{-}39)$$

where $\chi'^{(r)}$ and $\chi^{(r)}$ are functions of volume fractions $c^{(r)}$. These empirical functions are formulated based on experimental results and curve fitting techniques, as shown in section 7.

- Adding interfacial layer:

The active damaging processes in the interfacial layers between inclusions and matrix in the composite materials has been experimentally and theoretically investigated in the literature [85]. In order to include this debonding process during the multiscale analysis, an interfacial layer is considered between the matrix and inclusion. Fig. 3-2(a) represents a hypothetical RVE with embedded single elliptical inclusion and 2-2(b) shows the interfacial layer. The elastic properties in the interfacial layer are

assumed to vary linearly in this region. In the case of a spherical inclusion the following variable elastic stiffness tensor is enforced:

$$L_{ijkl}^{(IL)} - L_{ijkl}^{(1)} = \frac{L_{ijkl}^{(0)} - L_{ijkl}^{(1)}}{r_0 - r_{IL}}\left(r - r_{(IL)}\right) \tag{3-40}$$

where r shows the distance from the origin of the inclusion and $L_{ijkl}^{(IL)}$ is the variable interfacial layer stiffness tensor and $L_{ijkl}^{(0)}$ and $L_{ijkl}^{(1)}$ are respectively the matrix and inclusion stiffness tensors and r_o is the outer boundary of the inclusion and r_{IL} is the outer radius for the interfacial layer. This interfacial layer may contain material inherent or mechanical induced damages. The damage effect is added to the description of the L_{ijkl}^{IL} by the following expression [41]:

$$L_{ijkl}^{(IL)} = \left(I_{ijmn} - \kappa_{ijmn}\right)\overline{L}_{mnkl}^{(IL)} \tag{3-41}$$

where κ_{ijkl} is a fourth order anisotropic damage variable tensor proposed by Voyiadjis et al. [41] and $\overline{L}_{ijkl}^{(IL)}$ is the undamaged elasticity tensors. Debonding between the inclusion and the matrix may be captured by utilizing this concept in which the elastic modulus of this interfacial layer wanes with damage propagation. Thermodynamic consistent damage theories may be incorporated to evaluate the κ_{ijkl} in an incremental history dependent solution approach as discussed by Voyiadjis et al. [40-42].

- Atomic computation scheme:

The atomic computational approach, which is introduced within the micromechanics framework, provides computational competency to capture localized microscale mechanical responses over an RVE. This computational strategy can be considered as an alternative approach for FEA approaches in which a certain microstructural configuration is analyzed by tessellating unit cells [33, 47, 85-88]. Although Voronoi finite element method [89, 90] compensate for the huge computational difficulties in simulation of such a fine microstructures, these methods are still restricted by computational cost for large scale structural analysis.

The proposed atomic computation utilizes the generalized two-phase TFA solution, to solve a dilute multiphase system. In this approach a number of computational seeds are dispersed over a hypothetical computational layer and then this hypothetical layer is assembled over the RVE, as shown in Fig. 3-2(c). Then the underlying generalized two-phase TFA in the RVE is utilized to feed the required data to the computational layer in which inelastic analyses are implemented in each of the computational seeds. In other words in each computational seed the magnitude of the local strain, $\epsilon_{ij}^{(r)}(x_i, t)$, or local stress, $\sigma_{ij}^{(r)}(x_i, t)$, is given by the micromechanics solution. These values are then utilized in each of the computational seeds to compute the magnitude of the local inelastic strain and/or the damage parameter. Due to the fact that the micromechanics solution takes into account the compatibility in the deformation field and the equilibrium in the stress field, adding the computational layers over an RVE will not affect

these conditions. This atomic scheme provides the computational competency for localized evaluation of the inelastic and damage processes. Fig. 3-3 shows the outlines for the proposed atomic operation.

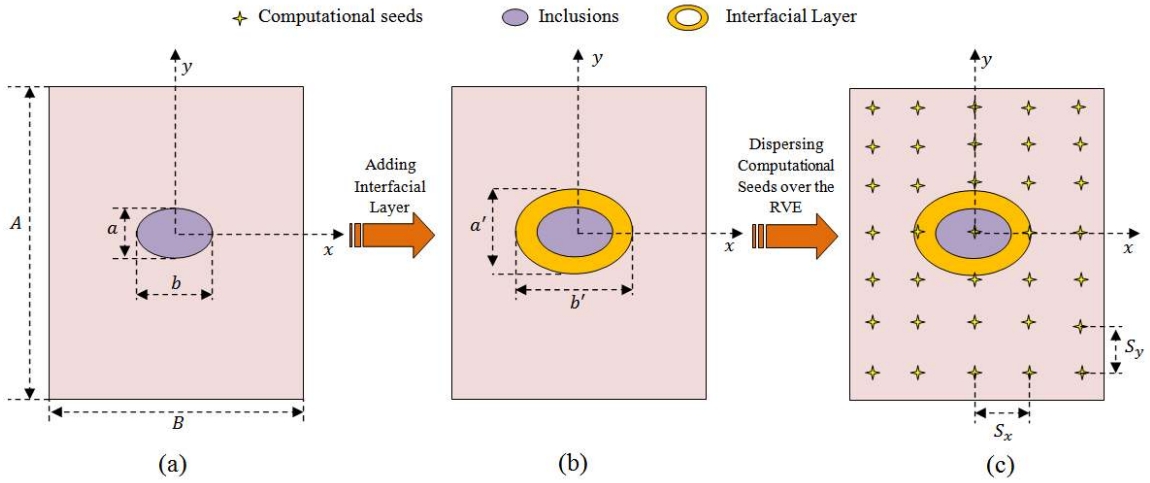

Figure 3-2(a) Two-phase RVE, (b) added interfacial layer between inclusion and matrix and (c) dispersing computational seeds over the RVE

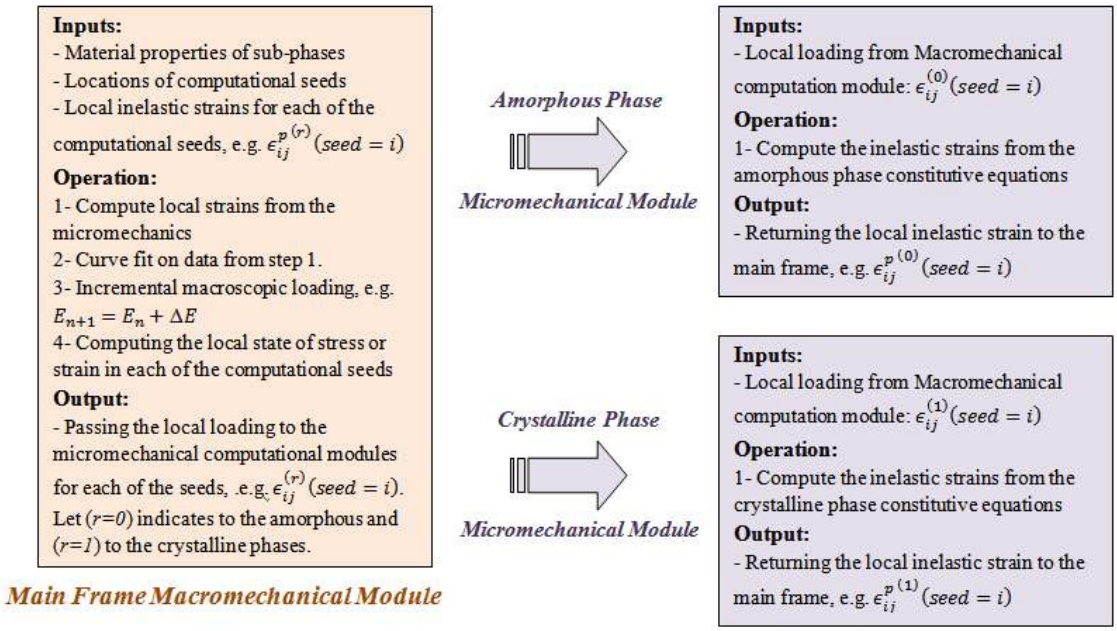

Figure 3-3 Flowchart for the multiscale analysis with proposed atomic computational strategy

- Generalized two-phase TFA solution:

The trivial two-phase TFA solution is generalized in this section in order to obtain the theoretical competency for a localized analysis within the RVE. In the micromechanics framework the microscale strain and stress fields are correlated to the macroscale strain and stress fields by concentration tensors, $A_{ijkl}^{(r)}(x_i)$ and $B_{ijkl}^{(r)}(x_i)$. The classical two-phase TFA solution removes the coordinate dependency in concentration tensors with averaging techniques [1-3]:

$$A_{ijkl}^{(r)} = \frac{1}{V}\int A_{ijkl}^{(r)}(x_i)dV \qquad \text{and} \qquad B_{ijkl}^{(r)} = \frac{1}{V}\int B_{ijkl}^{(r)}(x_i)dV \tag{3-42}$$

In this work, coordinate dependent descriptions for these concentration tensors are proposed which follow the basic micromechanics principals. Then the following expressions for the microscale stress, $\sigma_{ij}^{(r)}(x_i,t)$, and strain, $\epsilon_{ij}^{(r)}(x_i,t)$, fields are obtained:

$$\sigma_{ij}^{(r)}(x_i,t) = B_{ijkl}^{(r)}(x_i)\Sigma_{kl}(t) \qquad \text{and} \qquad \epsilon_{ij}^{(r)}(x_i,t) = A_{ijkl}^{(r)}(x_i)E_{kl}(t). \tag{3-43}$$

Accordingly, the solution for concentration tensors, $A_{ijkl}^{(r)}$ and $B_{ijkl}^{(r)}$, are trivial in elastic region, as shown in Eq. (3-41). Once the non-linear effects appears in sub-phases, such as the inelastic strain and residual stresses, these concentration tensors are affected by those effects [1-3].

Consequently, when the material behaves elastically, the state of microscale stress or strain in the RVE can be described by a primary curve fit on boundary values and trivial elastic solutions of these fields. Then the boundary of the macroscopic RVE, Γ, is decomposed into stress, Γ_σ, and displacement, Γ_u, defined boundaries in which $\Gamma_\sigma \cup \Gamma_u = \Gamma$ and $\Gamma_\sigma \cap \Gamma_u = \emptyset$. These concentration tensors should be equal to the fourth order identity tensor, I_{ijkl}, on their respective boundaries, i.e. $A_{ijkl}^{(r)}(x_i) = I_{ijkl}$ when $x_i \in \Gamma_u$ and $B_{ijkl}^{(r)}(x_i) = I_{ijkl}$ when $x_i \in \Gamma_\sigma$. In other words, the microscale stress and strain fields are equal to the loading conditions on boundaries of the macroscopic RVE to ensure that the microscale stress and strain fields conform to the macroscale loading conditions. On the other hand the trivial elastic solutions yield: $\epsilon_{ij}^{(r)}(t) = A_{ijkl}^{(r)}\epsilon_{kl}(t)$ and $\sigma_{ij}^{(r)}(t) = B_{ijkl}^{(r)}\sigma_{kl}(t)$. These values are assigned to the center of each of sub-phases ($r = 1\ to\ N$) in the RVE and then a curve is fitted on these data points in such a way that the resultant microscale stress, $\sigma_{ij}^{(r)}(x_i,t)$, and strain, $\epsilon_{ij}^{(r)}(x_i,t)$, fields follow the following micromechanics constrains:

$$\Sigma_{ij}(t) = \frac{1}{V}\int_V \sigma_{ij}^{(r)}(x_i,t)dV, \qquad E_{ij}(t) = \frac{1}{V}\int_V \epsilon_{ij}^{(r)}(x_i,t)dV. \qquad (3\text{-}44)$$

Once the non-linear process initiates, the microscale stress, $\sigma_{ij}^{(r)}(x_i,t)$, and strain, $\epsilon_{ij}^{(r)}(x_i,t)$, fields are then dependent on the microscale inelastic strains, $\epsilon_{ij}^{p\,(r)}(t)$, and residual stresses, $\sigma_{ij}^{Res\,(r)}(t)$, as shown by Eq. (3-36). Then the assigned elastic values of microscale stress and strain fields to the center of sub-phases are now are incrementally updated through Eq. (3-36) while constrain Eq. (3-48) are concurrently enforced. In such a way the curve fits always represents the latest microscale stress and strains in the RVE and these distributions can be a representation of local loading conditions on different portions of the RVE.

A three dimensional two-phase RVE under biaxial macroscale strain-controlled loading ($E_{xx} = E_{yy} = E$) is shown in 2- 4(a). The inclusion is shown by a purple ellipsoid and the assembled hypothetical computational seeds are depicted by yellow cubes. 2- 4(b) shows the local distribution of dimensionless microscale strain, $\epsilon_{ij}^{(r)}(x,y)/E$. This distribution results in $\epsilon_{ij}^{(r)}(x,y) = E$ on displacement defined boundaries of $x = \frac{B}{2}$ and $y = \frac{A}{2}$ and yields $\epsilon^{(1)} = A^{(1)}E$ and $\epsilon^{(0)} = A^{(1)}E$, which are the trivial elastic solutions for a two-phase RVE, at the center of inclusion and matrix phase which are $x = y = 0$ for inclusion $(r = (0))$ and $x^2 + y^2 = 0.625$ for matrix $(r = (1))$ in 3-4(b). Once the Eigen fields are introduced in the inclusion or matrix, Eq. (3-36) is the governing relation for obtaining $\epsilon^{(1)}$ and $\epsilon^{(0)}$. Then once in a load increment the non-linearity is introduced in one of the sub-phases, a new curve is fitted based on the following data points: (a) $\epsilon_{ij}^{(r)}(x,y) = E$ at boundaries $x = \frac{B}{2}$ and $y = \frac{A}{2}$ and (b) $\epsilon_{ij}^{(r)}(x,y,t) = A^{(r)}E + \sum_{s=1}^{2} D_{ijkl}^{(sr)}(x,y)\epsilon_{ij}^{p\,(r)}(x,y,t)$ at middle of each of the sub-phases. Consequently the microscale strain or stress distributions at each time increment monitor the latest non-linear effects in sub-phases while it satisfies the governing solid mechanics and micromechanics relations. In Section 7 a uniaxial loading problem for the two-phase and three-phase RVEs is evaluated to obtain the localized inelastic deformations.

- Generalized Eigen functions:

Dvorak et al. proposed the Eigen strain, $D_{ijkl}^{(sr)}$, and stress, $F_{ijkl}^{(sr)}$, influence functions in Eq. (3-36) to take into account the influence of adjacent and self-induced non-linear processes in the RVE domain [1-3]. Self-induced influences are captured when $r = s$ and non-linear effects from adjacent sub-phases are introduced by setting $r \neq s$. As shown in Eq. (3-39), the solution for a multi-phase material systems ($N > 2$) requires the knowledge of the self-induced tensors, i.e. $D_{ij}^{(rr)}$ for $r = 1\ to\ N$. These self-induced effects are experimentally difficult to capture or requires specific numerical approaches to be identified. For example for a multiphase system, $D_{ij}^{(rr)}$ may be obtained by FEA where a unit inelastic strain is introduced in each of the sub-phase and its effect on the neighboring domains is evaluated.

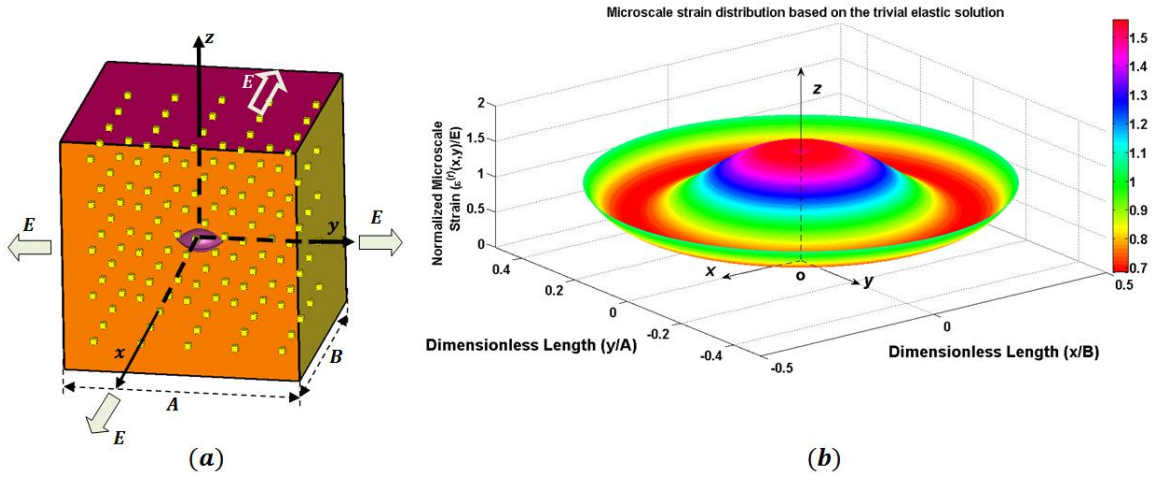

Figure 3-4 (a) two-phase RVE with embedded inclusion at center and assembled computational seeds in 3D configuration, (b) primary micro-strain distribution around the inclusion from the trivial elastic solution under the biaxial macroscale strain E (This distribution is updated after each load increment once the inelastic strain or damage is initiated in either of sub-phases.)

This processes needs to be implemented for $r = 1$ to N. Such a numerical approach encounters by some difficulties such as high volume computations and they are highly dependent on the microstructure of the RVE. In the case of a two-phase RVE, the solutions for these Eigen functions are trivial, as shown in Eq. (3-38).

One may assume a dilute distribution of inclusions in the RVE in which the two-phase localized RVEs are assembled to generate the multiphase RVE as shown in Fig. 3-5. In such a dilute regime the influence functions can still follow their analytical two-phase solution of Eq. (3-38). Then an alternative approach for dilute heterogeneous media is to utilize the trivial two-phase solution for local two-phase RVEs. In other words, for a statistically evenly dispersed inclusions in the RVE with a dilute distribution, one may assume a local two-phase media in which the analytical solution of Eq. (3-38) still holds in that localized region.

The Eigen functions, as shown in Eq. (3-38), are independent of coordinate system and consequently results in constant effect all over the two-phase RVE domain. This uniform distribution cannot monitor the reality where the Eigen influences should vanish for far sub-phases and has the maximum effect on the nearest sub-phases. In other words, once a non-linearity is introduced in one of the sub-phases its neighboring sub-phases should cease the major non-linearity influences while farther sub-phases receive less effects. The expressions for the Eigen influence function are then modified here to take into account such distance evanescent non-linearity effect. The distant evanescent Eigen influence functions for a two-phase RVE are then proposed as follows:

$$\text{self-induced: } \begin{cases} D_{ijkl}^{(11)}(x_i) = D_{ijkl}^{(11)}, & 0 < r < r_o \\ \text{adjacent-induced: } \begin{cases} D_{ijkl}^{(10)}(x_i) = D_{ijkl}^{(10)}\, log(r^a + b), & r_o < r < r_l \end{cases} \end{cases} \tag{3-45}$$

where $D_{ijkl}^{(11)}$ and $D_{ijkl}^{(10)}$ are given by Eq. (3-38) and, as depicted in Fig. 3-5, r shows the distant from the local origin on the center of inclusion and r_o and r_l correspond respectively to the outer boundary of inclusion and the furthest distant which influence function is assumed to be effective. Constant a and b are material dependent constants to represent the slop of changes and final limiting value of the influence function. The magnified view in Fig. 3-5 represents the influence region which is enclosed by a blue circular region. For computation efficiency one may assume that Eq. (3-49) is only effective on the computational seeds within a specified region and its effect is neglected for neighboring local two-phase RVEs.

Fig. 3-6 shows the normalized values for $D_{1111}^{(11)}(x,y)$ and $D_{1111}^{(10)}(x,y)$ in a local two-phase RVE with $a = -0.2$ and $b = 0.2$ when the inclusion contains the non-linearity effects. The inclusion size is assumed to be small compared to the RVE dimensions. The self-induced influences are assumed to be uniform over this small inclusion region ($D_{1111}^{(11)}(x,y) = D_{1111}^{(11)}$) while the adjacent influences are exponentially waned in the matrix region.

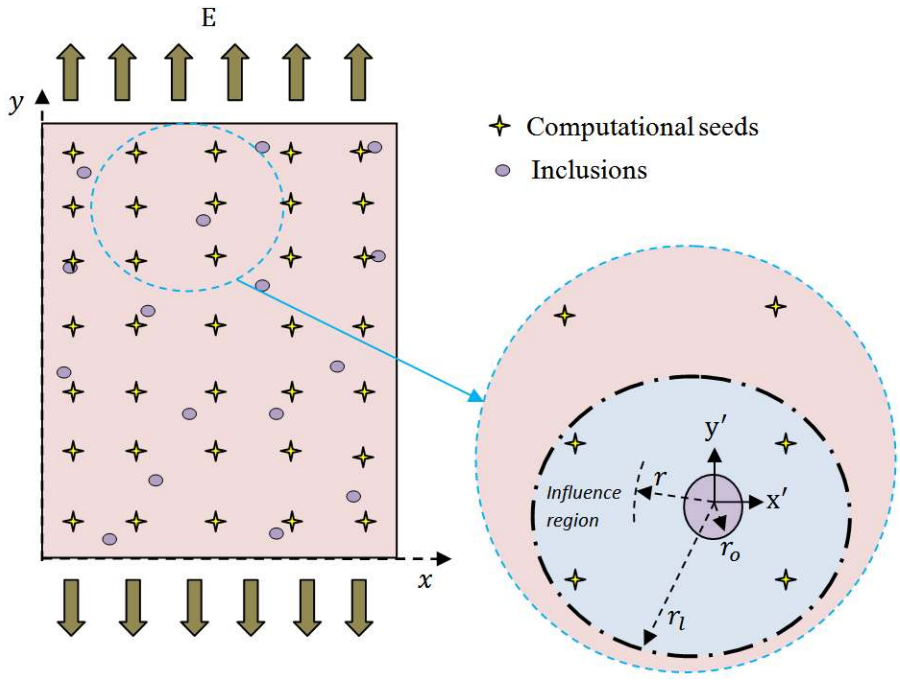

Figure 3-5 Dilute RVE with magnified view of influence region for Eigen influence functions

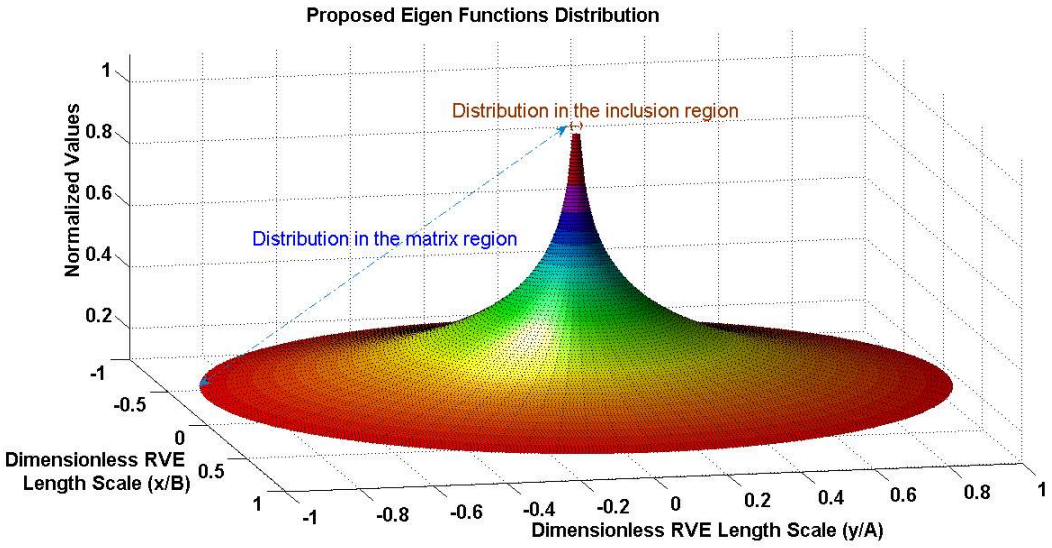

Figure 3-6 Distribution of the Eigen influence functions in 3D

- Regularization of a spare non-dilute heterogeneous media:

If the inclusions in an RVE are not dispersed statistically evenly, in certain cases the regularization techniques may be applicable to recast the dilute conformation. In such a case, the local dense distribution of inclusions in a certain region of the RVE is transformed into an equivalent inclusion. Then the local condense multiphase system is reduced to an equivalent local two-phase media and the dilute assumption for the macroscopic RVE is regained. For example in Fig. 3-7 the blue circle encloses a local dense distribution of inclusions. An equivalent inclusion is replaced in this local RVE in the magnified view. When these inclusions have different elastic properties, the equivalent inclusion may have averaged elastic properties as follows:

$$L_{ijkl}^{EQ-Inc} = \sum_{r=2}^{N} c^{(r)} L_{ijkl}^{(r)}$$
$$M_{ijkl}^{EQ-Inc} = \sum_{r=2}^{N} c^{(r)} M_{ijkl}^{(r)} \quad (3\text{-}46)$$

where L_{ijkl}^{EQ-Inc} and M_{ijkl}^{EQ-Inc} are equivalent elastic stiffness and compliance fourth order tensors. The dimension for this equivalent inclusion is obtained based on the distribution of dimensions in the local coordinate system. For example in the case of spherical or ellipsoidal inclusions, the projection of their

radii on local coordinate axes results in three components which are assembled in $\bar{R}_i^{(r)}$. The summation of these individual radii results in an equivalent ellipsoidal inclusion with the following radius:

$$\bar{R}_i = \sum_{r=1}^{N} \bar{R}_i^{(r)} \tag{3-47}$$

And the position of such an equivalent inclusion is obtained with respect to the local coordinate system as follows:

$$\overline{x}_i = \frac{\sum_{r=1}^{N} \left(\bar{R}_i^{(r)} \overline{x}_i^{(r)} \right)}{\bar{R}_i} \tag{3-48}$$

where $\overline{x}_i$ and $\overline{x}_i^{(r)}$ are respectively the origins for the equivalent and rth inclusions.

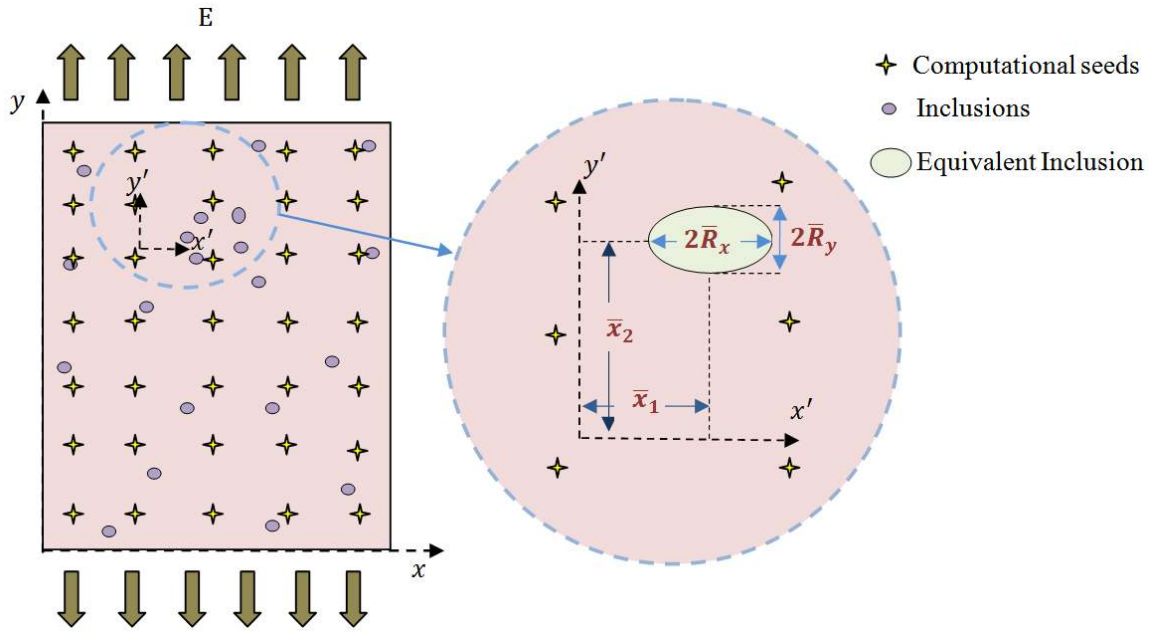

Figure 3-7 Regularization technique to reduce a spare RVE to an equivalent dilute media

3.7 Computational Aspect

The elasto-plastic multiscale analysis requires several computational modules including, (*i*) *microscale computation module:* which consists of a set of numerical solutions for the local constitutive equation of each sub-phases, *(ii) micromechanical computation module:* provides numerical tools to link the mechanical properties of each of the local sub-phases to the macroscopic responses, and *(iii) macroscale*

computation module: continuum mechanics governing equations are enforced in this module to simulate the overall mechanical response of the material and identifying the local loading conditions over the RVE. Each of these computational modules is discussed in the following.

3.7.1 Microscale Computation Module:

A schematic representation of an RVE for the semicrystalline polymeric system is depicted in Fig. 3-8(c). As discussed before, this material system is constituted from two phases including, amorphous and crystalline phases. At first step, regardless of the shape of each of these sub-phases, elasto-viscoplastic solutions should be enforced for each of them. In the microscale computation module, corresponding constitutive equations for each of these sub-phases are incorporated to obtain the local mechanical response of each of them. Inelastic constitutive equations for the crystalline and amorphous phases have been introduced in Section 3 and will be utilized here. In general, the RVE illustrates two length scales: (i) macro length scale: representing length for an RVE, see Fig. 3-8(c), and (ii) micro length scale: corresponding length to the smallest micro constituents which has a direct impact on the RVE behavior, see Fig. 3-8(a) and 3-8(b). Based on the polycrystalline multiscale analysis, in a semicrystalline SMP the crystals are treated as inclusions embedded in the amorphous phase [91].

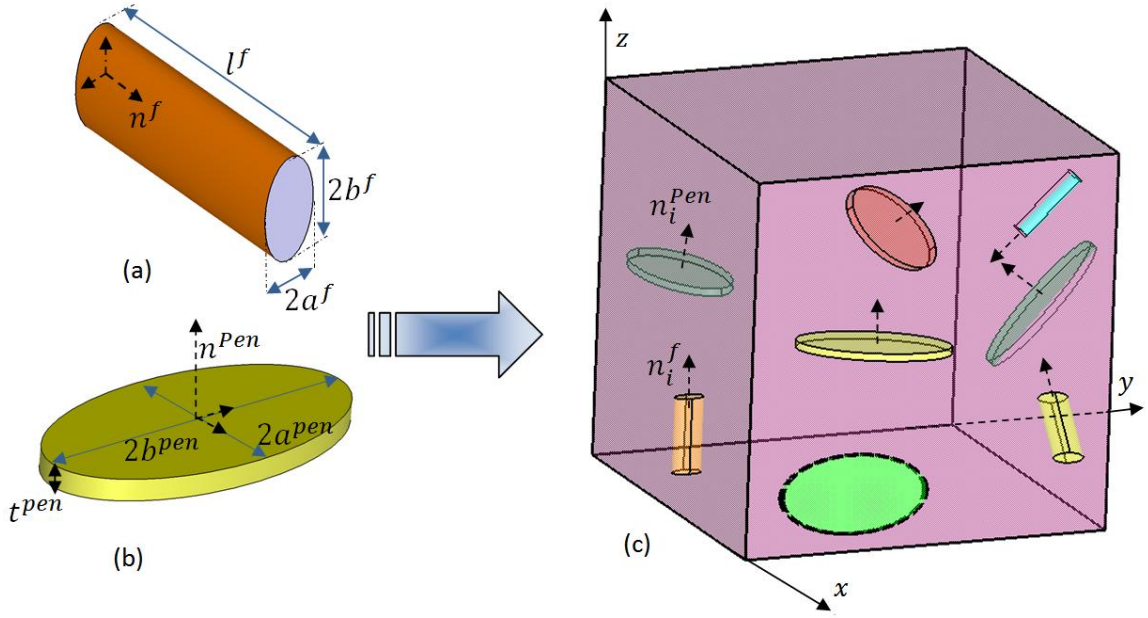

Figure 3-8 Schematic representations of (a) fibrous inclusion, (b) Penny-shape inclusion, and (c) Assembled RVE in a macro length scale.

The well-established elastic-predictor/plastic-corrector return mapping algorithm is utilized in this work to obtain the inelastic responses of the microscale amorphous and crystalline phases. This method is

outlined herein while a detailed description of this solution algorithm can be found in [52, 92, 93]. The return mapping technique is capable of handling associative and non-associative flow rules with variant tangent stiffness and results in a consistent solution approach [52, 59]. Based on the formulation of the objective finite deformation problem, this algorithm is applicable to the material, intermediate or spatial formulations. A detailed description of other finite deformation solution approaches may be found in [52, 57, 59, 94].

The return mapping techniques in inelastic solutions are natural consequence of splitting the total strain into elastic and inelastic strains. Let tensor, u_{ij}, be an incremental field to describe the deformation and its gradient, ∇u_{ij}, shows the deformation rate. Then the solution is carried out by *(i)* introducing a loading condition such as, $F_{ij}^{(n+1)} = (I_{ik} + \nabla u_{ik})F_{kj}^{(n)}$ where I_{ij} is the unity second rank tensor and superscripts n and $n+1$ indicates respectively to the previous and current load steps, *(ii)* elastically stretching the material by a "Trial Elastic" deformation gradient given by: $F_{ij}^{e\,(n+1)^{Trial}} = F_{ik}^{(n+1)} F_{kj}^{p\,(n)^{-1}}$ where superscripts "e" and "p" are referred to as "elastic" and "plastic" components, respectively; and $F_{ij}^{p\,(n)}$ shows frozen inelastic deformation gradient, *(iii)* relaxing the elastically stretched configuration until the state of stress satisfies the yield condition ($\psi = 0$). The return mapping relaxes the stresses along the steepest descent path which is defined based on yield function (associated flow rules) or potential functions (non-associated flow rules) [40]. The proposed microscale formulations are based on incompressibility assumption [60, 83] which is stated by: $\lambda_1\lambda_2\lambda_3 = 1$ where λ_i indicates the principal stretches. Simo et al. [95] introduced the isochoric assumption into the kinematic of large deformation by splitting the deformation gradient into the volume preserving and non-preserving parts as shown in the following:

$$\hat{F}_{ij} = J^{-\frac{1}{3}} F_{ij} \tag{3-49}$$

where hat symbol, $\widehat{\ }$, shows the isochoric components. Then $\hat{F}_{ij}$ is the volume-preserving deformation gradient and $J = \det(F_{ij})$. This decomposition holds for the elastic deformation too, $\hat{F}_{ij}^{e} = J^{-1/3} F_{ij}^{e}$. The proposed kinematic decomposition by Simo et al. [95] ensures that the computed inelastic deformation is isochoric, i.e. $\det(F_{ij}^{p}) \equiv 1$. The volume preservative right, $C_{ij} = F_{ik}^{T} F_{kj}$, and left, $b_{ij} = F_{ik}^{T} F_{kj}$, Cauchy-Green tensors are then evolved as follows:

$$\hat{C}_{ij} = J^{-\frac{2}{3}} C_{ij}\,;\; \hat{b}_{ij} = J^{-\frac{2}{3}} b_{ij} \tag{3-50}$$

To pertain the incompressibility assumption the volume-preserving part of the applied deformation gradient needs to be utilized in the t*rial elastic* part. Then the *trial elastic volume-preserving left and right Cauchy-Green* tensors are given by:

$$\hat{b}_{ij}^{e\,(n+1)^{Trial}} = \hat{F}_i^{e\,(n+1)^{Trial}} \left(\hat{F}_j^{e\,(n+1)^{Trial}}\right)^T = J^{(n+1)^{-\frac{2}{3}}} b_{ij}^{e\,(n+1)^{Trial}}$$
$$\hat{C}_{ij}^{e\,Trial} = J^{(n+1)^{-\frac{2}{3}}} C_{ij}^{e} \tag{3-51}$$

where $J^{(n+1)} = \det\left(F_{ij}^{(n+1)}\right)$. To relate the stress and strain states in a finite deformation problem there are a number of proposed stress-strain relations; see [57] for a list of these relations. Anand [96] proposed a relation between the Cauchy stress and Hencky strain which is used here to obtain the trial elastic stress as follows:

$$\sigma_{ij}^{(n+1)^{Trial}} = \frac{1}{J^{(n+1)}} L_{ijkl}^{e} \ln\left(U_{kl}^{e\,(n+1)^{Trial}}\right) \tag{3-52}$$

where $U_{ij}^{e\,(n+1)^{Trial}} = \sqrt{\hat{C}_{ij}^{e\,Trial}}$. The computed trial elastic stress is relaxed by the plastic-corrector method as described in Table 3-1. In Table 3-1, Q_{ij} is the hardening tensor and $|\dot{\lambda}|$ is the inelastic multiplier and shows the magnitude of inelastic deformation and μ is the shear modulus. The second order tensor $\hat{n}_{ij}$ defines the direction of the inelastic flow, for example in the case of associated formulation it is: $\hat{n}_{ij} = \partial\psi/\partial\sigma_{ij}$, where the yield surface is $\psi = 0$. The deviatoric stress and back stress tensors are respectively identified by, $s_{ij} = \sigma_{ij} - \frac{1}{3}\sigma_{mm} I_{ij}$ and $\alpha_{ij} = X_{ij} - \frac{1}{3} X_{mm} I_{ij}$.

Although the general outlines of this iterative solution algorithm hold for the inelastic analysis of the amorphous and crystalline phases, special cares should be given to implement this iterative solution algorithm precisely for both of these phases. A more detailed description of the implemented numerical method to obtain the inelastic response in these phases is respectively summarized in Table 3-2 and 3-3. The proposed crystalline solution algorithm is stable even in the case of activation of several slippage systems.

Fig. 3-9 shows the implementation of the proposed inelastic analysis approach for an SMP based particulate system [42]. The matrix is made from a polystyrene SMP (Veriflex, CRG Industries) with embedded thermoplastic particles (Abifor 501; ABIFOR Company). Table 3-3 shows the material constants for this SMP system.

3.7.2 Micromechanical Computation Module:

One of the most vital decisions in a micromechanical based analysis is the configuration of the RVE. An RVE should contain the most dominant phases with direct impact on overall mechanical responses, while it should result in a simple model. This configuration is obtained through examination of physical

facts and experimental results. Since during a large deformation the microstructure of an RVE may change an incremental formulation is required to capture these changes [21]. Dividing the local RVE into the several sub-phases requires specific numerical approach to develop the micromechanical related tensors. Due to the fact that inversing fourth order tensors encounter with some numerical difficulties, an alternative notation is adopted here to resolve this issue. In the context of the solid mechanics transferring the fourth order material tensors to a sixth order matrix is widely used [97]. In appendix A this conversion is elaborated in detail. In this computational module the micromechanics governing relations are enforced to obtain the local-overall relations.

Table 3-1 Iterative algorithm for an elastic-predictor/return mapping solution

1- Geometric update for a deformation controlled loading:

$u_{ij}\,;\, F_{ij}^{u} = I_{ij} + \nabla u_{ij}\,;\, F_{ij}^{(n+1)} = F_{ik}^{u} F_{kj}^{(n)}$;

2- **Elastic predictor:**

$F^{p}{}_{ij}^{(n+1)} = F^{p}{}_{ij}^{(n)}$; $F^{e}{}_{ij}^{(n+1)} = F_{ij}^{(n+1)} F^{p}{}_{ij}^{(n)^{-1}}$; $\psi = \psi\left(E_{ij}^{e\,(n+1)}, E_{ij}^{p\,(n)}, Q_{ij}\right)$

$\sigma_{ij}{}^{(n+1)^{Trial}}$;

3- Yield condition:

$\Psi\left(\sigma_{ij}{}^{(n+1)}, Q_{ij}^{(n+1)}\right) \leq 0$?

Yes: GO TO 1

No: continue to step 4,

4- **Plastic-corrector:**

$\sigma_{ij}^{(n+1)} = \sigma_{ij}{}^{(n+1)^{Trial}} - 2\mu\left|\dot{\lambda}^{(n+1,\Xi)}\right|\hat{n}_{i}^{(n+1)}$ and $\dot{Q}_{ij} = \dot{\lambda}^{(n+1,\Xi)} H_{ij}^{(n+1)}$; $\hat{n}_{ij}^{(n+1)} = \frac{\zeta_{ij}^{(n+1)}}{\left\|\zeta_{ij}^{(n+1)}\right\|}$;

$\zeta_{ij}^{(n+1)} = s_{ij}^{(n+1)} - \alpha_{ij}^{(n+1)}$,

where Ξ shows the iteration number and $\dot{\lambda}^{(n+1,\Xi)}$ is a primary value for the plastic multiplier and $\dot{\lambda}^{(n+1,\Xi+1)}$ is its updated value. The updated value is obtained by enforcing the consistency condition (inviscid flow) or viscoplastic potential (viscid flow) [40];

$\dot{\epsilon}_{ij}^{p\,(n+1,\Xi+1)} = \sqrt{\frac{2}{3}}\left|\dot{\lambda}^{\,(n+1,\Xi+1)}\right|\hat{n}_{ij}^{(n+1)}$,

5- Convergence check: $error = \frac{\left|\dot{\lambda}^{\,(n+1,\Xi+1)} - \dot{\lambda}^{\,(n+1,\Xi)}\right|}{\dot{\lambda}^{\,(n+1,\Xi)}} < TOL$???

YES:

(a) store $\sigma_{ij}^{(n+1)}$, (b) compute $F_{ij}^{e\,(n+1)}$ from updated stress state $\sigma_{ij}^{(n+1)}$, (c) $F_{ij}^{p\,(n+1)} = F_{ij}^{(n+1)} F_{ij}^{e\,(n+1)^{-1}}$, (d) store $Q_{ij}^{(n+1)}$, (e) $\epsilon_{ij}^{p\,(n+1)} = \epsilon_{ij}^{p\,(n)} + \dot{\epsilon}_{ij}^{p\,(n+1)}$, (f) $\alpha_{ij}^{(n+1)} = \alpha_{ij}^{(n)} + \dot{\alpha}_{ij}^{(n+1)}$, (g) $\dot{\lambda}^{(n+1,\Xi)} = \dot{\lambda}^{(n+1,\Xi+1)}$ and GO TO NEXT LOAD STEP

NO:

GO TO STEP 4 WITH $\dot{\lambda}^{(n+1,\Xi)} = \dot{\lambda}^{(n+1,\Xi+1)}$

Table 3-2 Outlines for a finite strain elasto-viscoplastic strain controlled elastic-predictor/plastic-corrector solution for the amorphous phase. (Superscripts "(n)" and "(n+1)" indicate respectively the previous and current load steps.)

Elastic Predictor:

1-The stretch is given through the loading condition:

$\lambda_1^{(n+1)} = 1 + \sum_{t=0}^{N} \Delta\epsilon_1$

2- Incompressibility assumption, $\lambda_1^{(n+1)}\lambda_2^{(n+1)}\lambda_3^{(n+1)} = 1$, together with isotropy or anisotropy conditions are enforced to obtain $\lambda_2^{(n+1)}$ and $\lambda_3^{(n+1)}$. Then the resultant stretches due to uniaxial tension and isotropy assumption together with the right Cauchy-Green tensors are given by:

$\lambda_2^{(n+1)} = \lambda_3^{(n+1)} = \sqrt{1/\lambda_1^{(n)}}$ and $C_{ij}^{(n+1)} = F_{ik}^{(n+1)^T} F_{kj}^{(n+1)}$

3-Updated deformation gradient and right Cauchy-Green tensor are computed as:

$F_{ij}^{(n+1)} = (I_{ik} + \Delta\epsilon_{ik})F_{kj}^{(n)}$, and $C_{ij}^{(n+1)} = F_{ik}^{(n+1)^T} F_{kj}^{(n+1)}$

4- The previous, $\sigma_{ij}^{(n)^{Trial}}$, and current, $\sigma_{ij}^{(n+1)^{Trial}}$, trial elastic stress tensor are captured by incorporating the Anand relation [96]:

$\sigma_{ij}^{(n)^{Trial}} = \frac{1}{\left|F_{ij}^{(n)}\right|} E_{ijkl} * log\left(\sqrt{C_{kl}^{(n)}}\right)$, $\sigma_{ij}^{(n+1)^{Trial}} = \frac{1}{\left|F_{ij}^{(n+1)}\right|} E_{ijkl} * log\left(\sqrt{C_{kl}^{(n+1)}}\right)$,

5- The stress increment tensor, $\Delta\sigma_{ij}$, and the updated deviatoric stress tensor, $s_{ij}^{(n+1)}$, are respectively given by:

$\Delta\sigma_{ij} = \sigma_{ij}^{(n+1)} - \sigma_{ij}^{(n)}$, $s_{ij}^{(n+1)} = \sigma_{ij}^{(n+1)} - \frac{1}{3}\sigma_{kk}^{(n+1)}\delta_{ij}$,

Plastic Corrector:

6- Plastic gradient, $F_{ij}^{p\,(n+1)}$, plastic right Cauchy-Green tensors, $C_{ij}^{p\,(n+1)}$, and $\sigma_{ij}^{(n+1)}$ and $s_{ij}^{(n+1)}$ are updated by a primary plastic strain $\epsilon_{ij}^{p\,(n+1,\Xi)}$ where Ξ shows the number of iteration:

$F_{ij}^{p\,(n+1)} = \left(I_{ij} + \epsilon_{ij}^{p\,(n+1,\Xi)}\right)$, $C_{ij}^{p\,(n+1)} = F_{ik}^{p\,(n+1)^T} F_{kj}^{(n+1)}$,

$\sigma_{ij}^{(n+1)} = \sigma_{ij}^{(n+1)^{Trial}} - \frac{1}{\left|F_{ij}^{p\,(n+1)}\right|} E_{ijkl}\ \log\left(\sqrt{C_{kl}^{p\,(n+1)}}\right)$, $s_{ij}^{p\,(n+1)} = \sigma_{ij}^{p\,(n+1)} - \frac{1}{3}\sigma_{kk}^{p\,(n+1)}\delta_{ij}$,

7- Plastic strain is updated from primary value $\epsilon_{ij}^{p\,(n+1,\Xi)}$ to a more updated value $\epsilon_{ij}^{p\,(n+1,\Xi+1)}$. This is accomplished by incorporating the corrected stress, $\sigma_{ij}^{(n+1)}$, in the associated inelastic constitutive equations. The convergence error is checked by two inelastic strains resulted from two subsequent iteration numbers Ξth and $(\Xi+1)$th as stated in the following:

$e = \frac{\left|\epsilon_{ij}^{p\,(n+1,\Xi+1)} - \epsilon_{ij}^{p\,(n+1,\Xi)}\right|}{\epsilon_{ij}^{p\,(n+1,\Xi)}} < TOL\,???$,

8- **YES**:

GO TO THE NEXT LOAD STEP.

NO:

GO TO STEP 6 with: $\epsilon_{ij}^{p\,(n,\Xi)} = \epsilon_{ij}^{p\,(n,\Xi+1)}$ and repeat the iteration with this updated plastic strain.

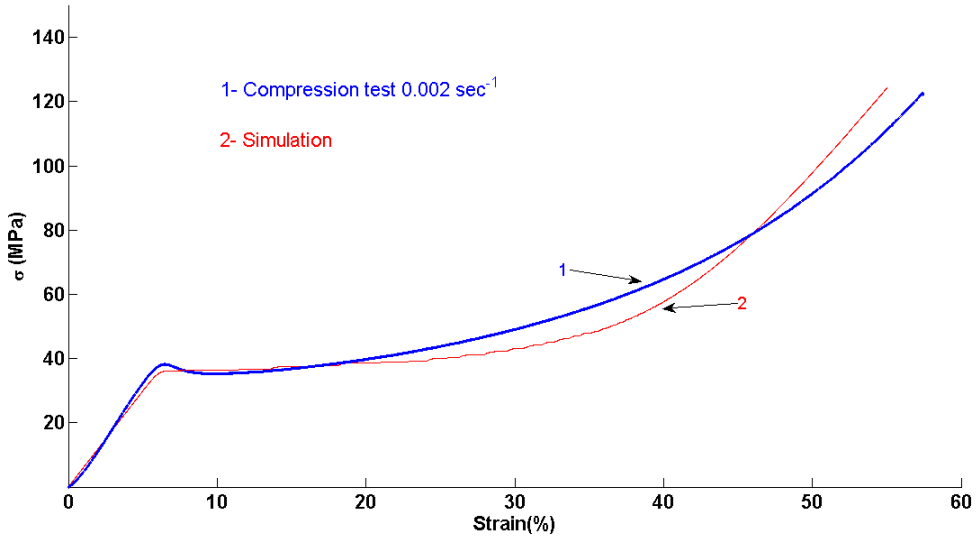

Figure 3-9 Simulation and experimental results for a SMP system with embedded thermoplastic particles [42]

Table 3-3 Material constants for the SMP system presented in Fig. 3-9

nkT	$\dot{\gamma}_0(\text{sec}^{-1})$	A	h	λ_L	k	T (K)	σ_y(MPa)
3.5	1	3.31e-27	50	1.73	1.38e-23	298	40

3.7.3 Macroscale Computation Module:

The micromechanical based analysis may be utilized to find the overall behavior of the macroscale RVE as a function of the predefined incremental surface boundary conditions on the microscale sub-phases. Or vice-versa it can be used to establish the local mechanical behaviors based on predefined macroscale loading condition on the RVE surface. The microscale surface tractions should result in a self-equilibrating traction field on the boundary of macroscopic RVE or microscale surface deformations should yield a self-compatible displacement field in the macroscopic RVE. The macroscale stress and strain state in a continuum media are respectively denoted with tensors Σ_{ij} and E_{ij} herein. In micromechanics it is assumed that averaged uniform stress, $\bar{\sigma}_{ij}$, and strain, $\bar{\epsilon}_{ij}$, tensors in an RVE are equal to those applied on the continuum media, $\Sigma_{ij} = \bar{\sigma}_{ij}$ and $E_{ij} = \bar{\epsilon}_{ij}$. Then $\bar{\sigma}_{ij}$ and $\bar{\epsilon}_{ij}$ should satisfy the continuum equilibrium equations and strain-displacement relations. Then the computed microscale

mechanical responses are enforced to (i) build the macroscale constitutive behavior and (ii) ensure the compatibility between all sub-phases.

Table 3-4 Inelastic solution algorithm based on elastic-predictor/plastic-corrector for the crystalline phase (Superscripts "(n)" and "(n+1)" indicate respectively the previous and current load steps.).

1- Chain slip systems are introduced to the computation module, **Elastic Predictor:** 2- Same loading condition as outlined in Table 3-2 is applied. Due to the incremental form of constitutive equation of the crystalline phase the incremental form of Cauchy stresses is utilized to integrate over the loading path, *i.e.* $\Delta\sigma_{ij}^{(n+1)} = E_{ijkl}\,\Delta\epsilon_{kl}$, **Plastic Corrector:** 3- Let Ξ indicates the iteration number. The stress increment is updated based on a primary value of inelastic strain rate: $\Delta\sigma_{ij}^{(n+1)} = E_{ijkl}\left(\Delta\epsilon_{kl} - \Delta\epsilon_{kl}^{p\ (n+1,\Xi)}\right)$, 4- For every slip systems values of $R_{ij}^{(\alpha)}$, $A_{ij}^{(\alpha)}$, C_{ij}, S_{ij}^{c*}, $\tau^{(\alpha)}$ and $\dot{\gamma}^{(\alpha)}$ are computed to obtain $D_{ij}^{c\ (n+1,\Xi+1)}$. Maximum $\tau^{(\alpha)}$ shows the dominant slip mechanism and its corresponding $\dot{\gamma}^{(\alpha)}$ in a two subsequent iteration numbers Ξth and $(\Xi+1)$th is stored to compute the error as: $e = \frac{\left\lvert \dot{\gamma}^{(\alpha)^{(\Xi+1)}} - \dot{\gamma}^{(\alpha)^{(\Xi)}} \right\rvert}{\dot{\gamma}^{(\alpha)^{(\Xi)}}}$, 5- If converged go to the step 6, if not converged go to the step 3 with $\Delta\epsilon_{kl}^{p\ (n+1,\Xi)} = D_{ij}^{c\ (n+1,\Xi+1)}$, 6- Update the crystallographic axes, c_i, and lattice spin tensor, W_{ij}^{*}, and then go to the next load step.

The TFA model utilizes the Eshelby inclusion analytical solutions to compose the macroscopic RVE and to describe the size and shape of inclusions. These inclusions are assumed to be perfectly bonded to the matrix and have standard geometries, e.g. ellipsoidal, fibrous or penny shape inclusions. The macroscale mixed boundary conditions are introduced as applied macro strain, E_{ij}, on displacement defined boundary, Γ_u, and macro stress, Σ_{ij}, on stress defined boundary, Γ_Σ, in which $\Gamma_u \cap \Gamma_\Sigma = \emptyset$ and $\Gamma_u \cup \Gamma_\Sigma = \Gamma$. The strain, $A_{ijkl}^{(r)}$, and stress, $B_{ijkl}^{(r)}$, concentration tensors are known from trivial elastic solution of Eq. (3-41); and they are utilized to derive the microscale loading condition, e.g. microscale local stress tensors, $\sigma_{ij}^{(0)}$ and $\sigma_{ij}^{(1)}$, or strain tensors, $\epsilon_{ij}^{(0)}$ and $\epsilon_{ij}^{(1)}$. These solutions ensure the compatibility in the

deformation field and equilibrium in the stress field. These solutions are utilized to find the microscale loading conditions. Once the non-linearity is introduced to the material system the updated values based on Eq. (3-36) is used to update the curve fit results. The configuration of the inclusion in the RVE (morphological texture) is evaluated with respect to Eqs. (25) and (26) where interfacial vectors are updated base on the deformation gradients. Fig. 3-10 shows an overall representation of proposed computational approach, described in Section 6.

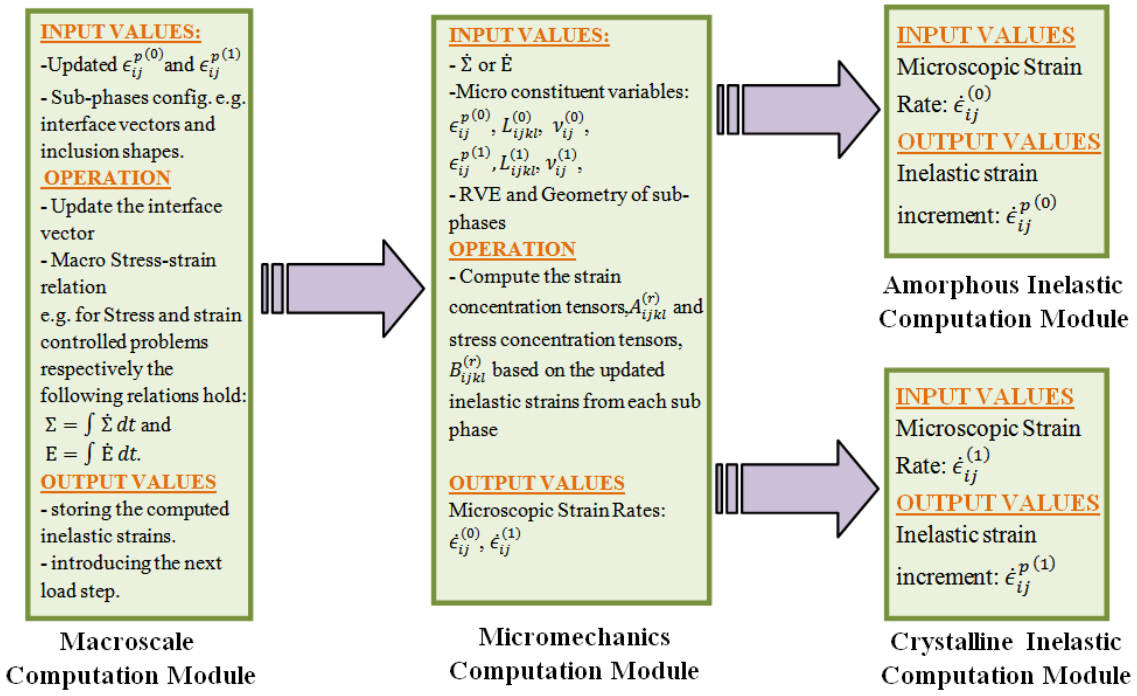

Figure 3-10 A simplified flowchart for the implementation of the proposed computational strategy

Fine load increments together with running several iterative numerical processes result in a computationally stiff problem. A petascale programming may be required to empower the computational resources with incorporating parallel processing techniques. The proposed numerical approach allows the designers to maximize the parallel code resources and allocate several computational threads to solve the problem. This numerical methodology may reduce the computational time significantly especially when a complex structure is evaluated.

3.8 Experimental observations and numerical implementations

The mechanical properties of a semicrystalline copolymer made from poly (tetramethyleneoxide) (PTMO) as the soft segment in conjunction with crystallizable poly (trimethyleneterephthalate)(PTT) as

the hard segment has been investigated by [45]. Table 3-5 gives the reported material properties for different volume fractions of hard and soft segments [45]. The crystalline micromechanical computational module is adjusted to capture the 100 wt% hard segment and the amorphous micromechanical computational module is designed to capture the 20 wt% hard segment sample (nearest experimental result to the 100wt% soft segment). Table 3-5 shows the related material parameters for these simulations and Table 3-6 presents the slippage systems in a crystalline polymeric system with hypothetical resistances where notations "{}" and "<>" shows respectively the family of planes and directions.

Table 3-5 The tensile properties of PTT–PTMO copolymer [45]

Sample	E(MPa)
100 wt% Hard Segment	2102.8
80 wt% Hard Segment	711.2
40 wt% Hard Segment	130.2
20 wt% Hard Segment	15.9

Table 3-6 Material parameters for soft and hard segments computational modules

Amorphous Computational Module (Soft Segment (0))								
nkT (MPa)	$\dot{\gamma}_0$(sec-1)	A	ζ	λ_L	k	T (K)	σ_y(MPa)	E(MPa)
20	1e-4	3.31e-27	1e-5	0.316	1.38e-23	298	5	16
Crystalline Computational Module (Hard Segment (1))								
n	$\dot{\gamma}_0$ (sec-1)	Reference Cry. Axes			Slippage Systems		σ_y(MPa)	E(MPa)
4.5	3	(0.5,0.5,0.5)			See Table (3-7)		70	2102.8

Table 3-7 Hypothetical crystalline slippage systems [98]

Slippage Type	Indicial Notation	Normalized resistance (g^{α}/τ_0)
Chain Slip	(100)[001]	1
	(010)[001]	2.5
	{110}[001]	2.5
Transverse Slip	(100)[010]	1.6
	(010)[100]	2.5
	{110}<1$\bar{1}$0>	2.5

Figs. 11 and 12 show the simulation results together with the tension test results [98] for the mentioned two phase semicrystalline copolymer system. These experimental test results are utilized to obtain the $\chi^{(0)}$ and $\chi^{(1)}$ for the two volume fractions as shown in each graph. Then a linear curve is fitted on these correction parameters to obtain the following empirical relations:

$$\chi^{(0)} = -1.05 \times c^{(0)} + 1.71$$
$$\chi^{(1)} = 0.375 \times c^{(1)} + 0.58 \tag{3-53}$$

Eq. (3-57) is then utilized to capture the mechanical responses of the semicrystalline polymeric material systems with different volume fractions of the hard and soft segments, as shown in Fig. 3-13.

Next experimental test result corresponds to the polyurethane SMP reported by Tobushi et al. [99]. Due to the lack of the experimental results for the individual micro constituents of this semicrystalline polymer-based material system, two hypothetical mechanical responses are assumed for the amorphous and crystalline phases to show the capability of the proposed micromechanical theory. The behaviors of these micro constituents are suggested respectively with red and black lines in Fig. 3-14 while blue line shows a semicrystalline system with 40 wt% degree of crystallinity. The correction parameters are $\chi^{(0)} = 0.73$ and $\chi^{(1)} = 0.8$ for this set of test results. The material parameters for the amorphous and crystalline phases are presented in Table 3-8.

Fig. 3-15 shows the micromechanical simulation results for a semicrystalline polyurethane SMP with different content of crystalline volume fractions and with fixed values for correction parameters $\chi^{(0)}$ and

$\chi^{(1)}$. These hypothetical simulations in Fig. 3-15 confirm the role of crystalline segment volume fraction in stiffening the mechanical responses. As shown in this figure, the higher the amorphous phase content the softer the mechanical responses.

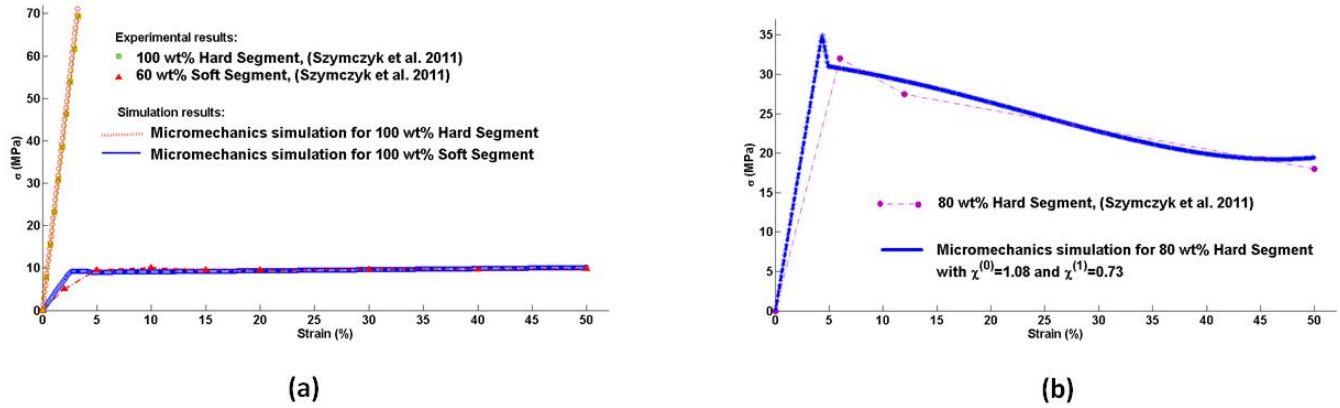

Figure 3-11 simulation and experimental results for a two-phase semicrystalline copolymer, experiments are after [45]

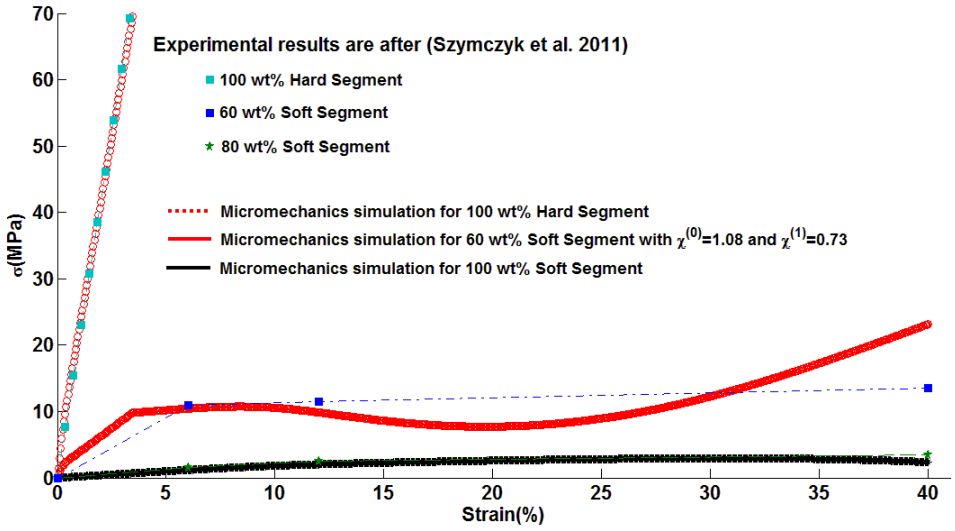

Figure 3-12 simulation and experimental results for a two-phase semicrystalline copolymer, experiments are after [45]

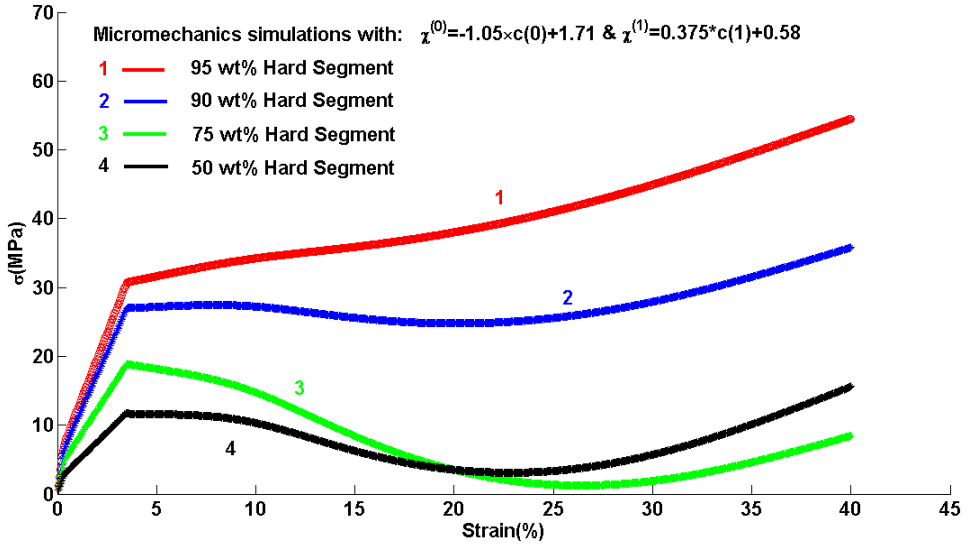

Figure 3-13 micromechanical simulations based on obtained empirical relations for correction factors $\chi^{(0)}$ and $\chi^{(1)}$

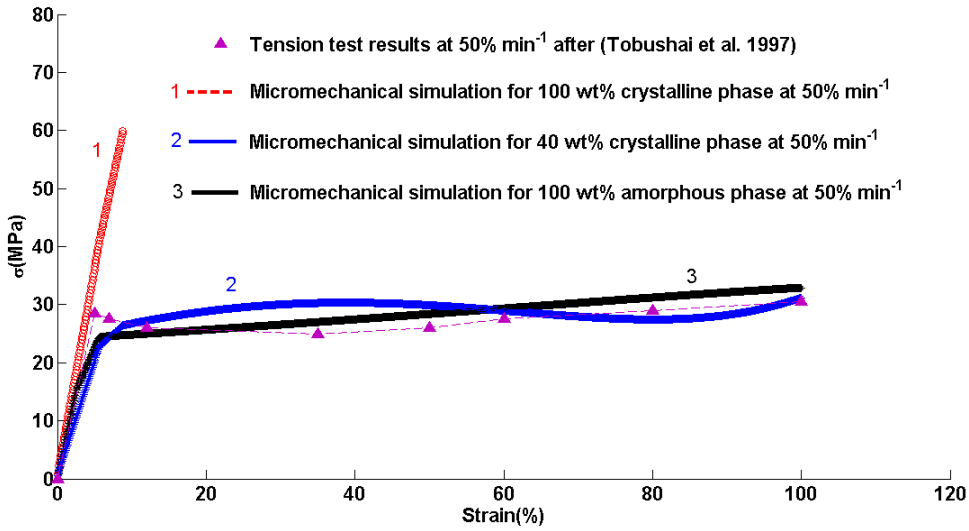

Figure 3-14 simulation and experimental results for a two phase semicrystalline polyurethane SMP (experiments are after [99])

The simulation results of the proposed micromechanical theory heavily depend on (i) material parameters in each sub-phase, (ii) volume fraction of each micro constituent and (iii) correction factors. The material parameters for each sub-phase are obtained based on the standard procedures available in the literature [60, 65, 79, 83]. While the volume fractions is a known data from the experimental procedures, the correction factors are required to be established based on the numerical curve fitting

techniques. Here an algorithm is developed to iterate the solutions with different values of correction factors until the deviation from the experimental data and the simulation bounds in an acceptable range.

Table 3-8 Material parameters for crystalline and amorphous computational modules

Amorphous Computational Module (Soft Segment (0))								
nkT (MPa)	$\dot{\gamma}_0(\sec^{-1})$	A	ζ	λ_L	k	T (K)	σ_y(MPa)	E(MPa)
10	1e-6	3.31e-27	1e-2	0.9747	1.38e-23	308	15	300
Crystalline Computational Module (Hard Segment (1))								
n	$\dot{\gamma}_0$ ($\sec^{-1}$)	Reference Cry. Axes		Slippage Systems			σ_y(MPa)	E(MPa)
4	5	(0.5,0.5,0.5)		See Table (3-7)			60	700

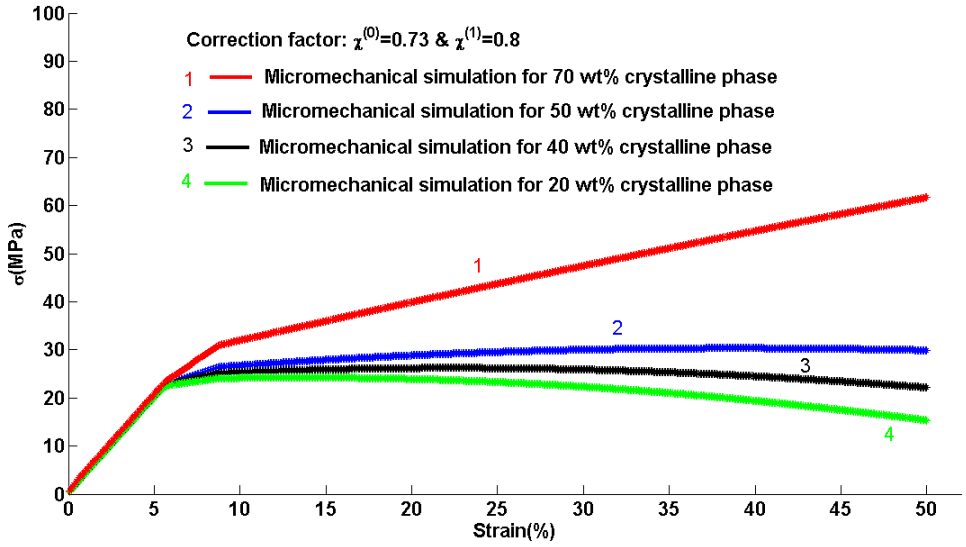

Figure 3-15 Micromechanical simulation for semicrystalline polyurethane SMP with different crystalline volume fraction content

In the case of localized evaluation of inelastic fields within the RVE, for the first example a simple two-phase RVE under uniaxial strain-controlled loading along the *x* direction is considered, as shown in Fig. 3-16. The matrix is made from amorphous phase and the ellipsoidal inclusion is made from crystalline phase. Each of these phase follow its respective constitutive relations as discussed before. Six

computational seeds are assembled on the middle plane of the RVE and the proposed atomic operation is applied on this system. The primary microscale strain distribution for this configuration is given by a 4^{th} degree curve fit, as depicted in Fig. 3-16, which is fitted on boundary and primary elastic solution of local strains. The data point for the curve fitting are extreme values of elastic solution for local strains, given by the micromechanics elastic solutions, i.e. $A^{(0)}E$ and $A^{(1)}E$ and boundary values which are E at $x = 0$ and $x = B$. This curve fitting is introduced as the local loading condition to the main computational module and once the non-linear effects are introduced into the system this 4^{th} degree polynomial curve is updated based on the latest local inelastic strains.

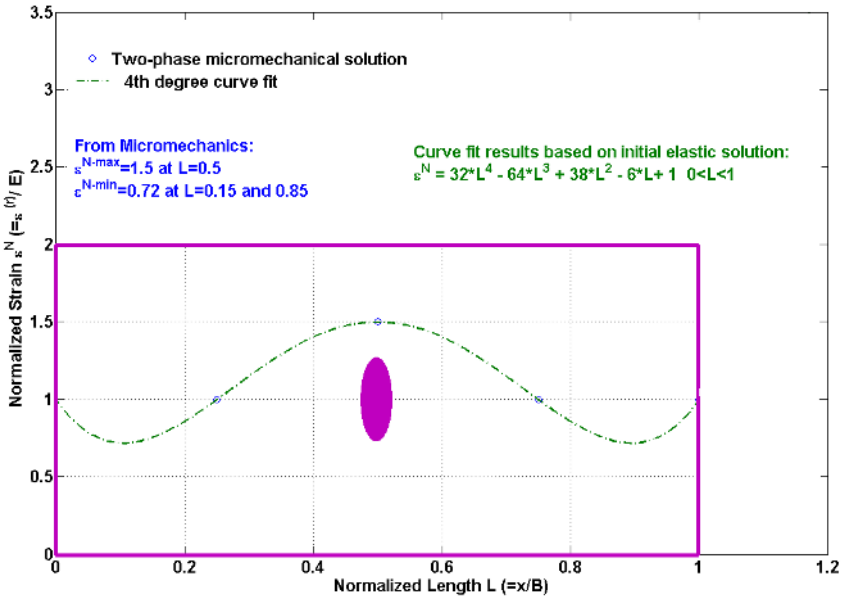

Figure 3-16 Microscale strain distribution for a two-phase RVE with schematic RVE configuration

The proposed atomic computation resolves the deficiency of the classical two-phase TFA solution which results in the uniform inelastic strain distributions over the sub-phases. The local distribution of inelastic strain is depicted at the mid-plane of the RVE, $y/A = 0.5$, in Fig. 3-17 where three level of macroscale strain E are shown. The magnitudes of the local inelastic strains are gradually increased in all seeds while at higher strain levels the gap between inelastic strains in the inclusion and matrix enlarges. These localized data can easily be utilized for defining debonding criteria between matrix and inclusion.

In a more general case the curve fit results for a two-phase RVE is shown in Fig. 3-18, where the primary microscale strain distribution from micromechanics elastic solution and the 6^{th} degree curve fit is depicted in the RVE. Fig. 3-19 shows the local inelastic strain distribution at middle plane of the RVE in which two macroscale strain levels are depicted.

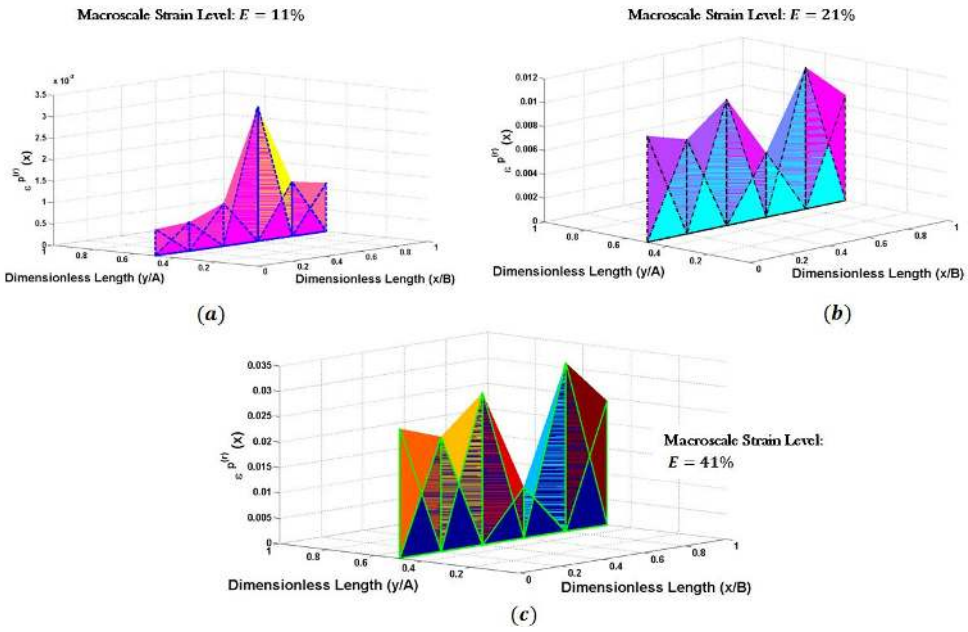

Figure 3-17 Microscale inelastic strain distribution for a two-phase RVE with 6 computational seeds placed at the middle plane of the RVE, y/A=0.5. The macroscale strain levels are: (a) $E = 11\%$, (b) $E = 21\%$ and (c) $E = 41\%$

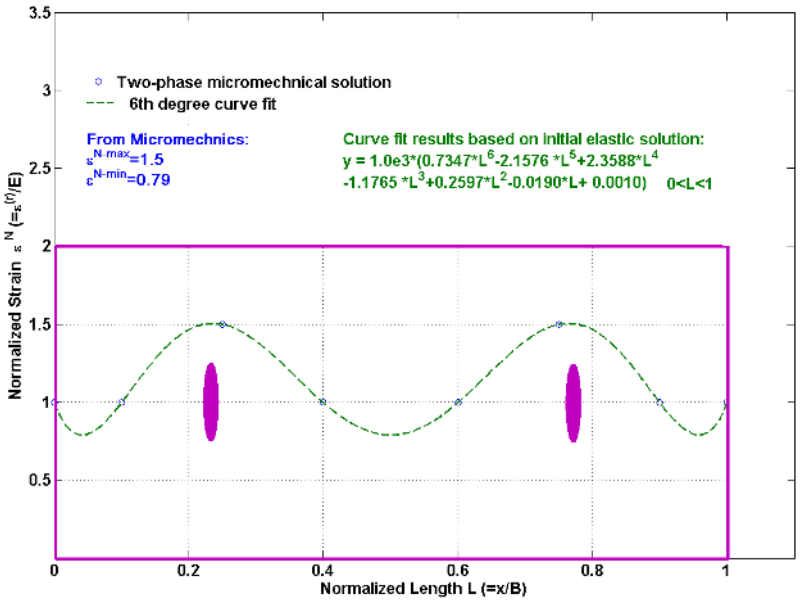

Figure 3-18 Microscale strain distribution for a three-phase RVE with schematic RVE configuration

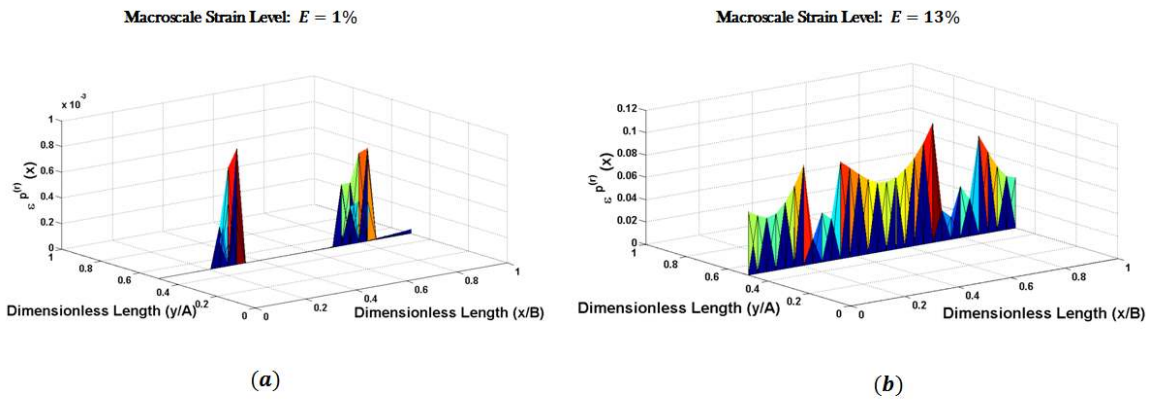

(a) (b)

Figure 3-19 Microscale inelastic strain distribution for a three-phase RVE with 30 computational seeds placed at the middle plane of the RVE, y/A=0.5. The macroscale strain levels are (a) $E = 1\%$ and (b) $E = 13\%$

At $E = 1\%$ the dominant inelastic strains are accumulated in inclusions while in $E = 13\%$ the gap between inelastic strain in matrix and inclusion is getting significant. These data can provide the necessary insight for local failure analysis within a multiphase material system.

3.9 Conclusions

The multiscale analysis within the micromechanics framework is refined in order to obtain the computational competency for a localized inelastic and damage analysis within the RVE. In the case of dilute heterogeneous media, the classical two-phase TFA solution is generalized in order to apply it on local two-phase RVEs. The atomic computation concept is then introduced where a hypothetical computational layer is assembled over the RVE. This hypothetical layer consists of a series of computational seeds which are dispersed systematically over this layer. The mentioned local two-phase RVEs in the dilute heterogeneous media utilize this generalized two-phase TFA solution to identify the microscale strain or stress distributions. While the material is responding elastically these microscale stress and strain distributions are trivial and for each of the local two-phase RVEs, the maximum and minimum strains or stresses are defined by the trivial elastic solution. A basic curve fit over these data and their corresponding boundary values approximately monitors the microscale stress and strain distribution over the macroscopic RVE. Once the non-linearity is introduced into the material systems these microscale fields are updated incrementally based on the latest local inelastic deformation. Hence the curve fit results can monitor the state of microscale stress and strain distributions over the macroscopic RVE. The computational seeds are fed by these microscale strain and stress distributions which are provided by modified TFA solution. The position of these computational seeds defines the corresponding governing equations to be utilized for updating the local inelastic strain or residual stress. In other words, the local loading on each of these seeds are passed to their corresponding constitutive

equations to update the local state of inelastic strain or residual stress. This atomic computational approach competes with FEA approach where these localized evaluations are obtainable by fine meshes. While several mesh refinement are required in an FEA analysis to ensure that the stress singularities are not involved, these methods are highly dependent on the microstructure of the RVE and once the configuration of the RVE is changed a new FEA needs to be implemented. This fact promotes the TFA based micromechanics multiscale analysis in which the constitutive equations of the system are established and the microstructure of the RVE is easily changed when the corresponding Eshelby inclusion tensor is substituted. The stiff inelastic TFA responses are then addressed. The modified TFA method softens the TFA results and provides the mathematical competency to capture the irregular inelastic deformation of glassy polymers.

This scheme is then applied on the semicrystalline glassy polymer-based material systems where the spherulite crystalline phases are embraced with the amorphous phase. An RVE within the micromechanics is defined where matrix is constituted from the amorphous phase and the crystalline phase are introduced as inclusions in this matrix. Each of these phases follows their respective constitutive equations where molecular alignment in the amorphous phase and crystalline texture updates in the crystalline phase are taken into account. The crystalline inclusion may undergo deformation and rotation during a finite deformation process which results in a morphological texture changes. This texture update is considered based on a predefined normal vector on the interface of the inclusion where changes in the magnitude and direction of this interfacial vector represent the morphological changes. The interfacial vector is updated by enforcing the deformation compatibility at the boundary surface of the inclusion and matrix.

The proposed generalized two-phase micromechanics solution together with atomic computation scheme appears to be applicable on multiscale analysis of a very general multiphase dilute system. This multiscale analysis scheme assists the designers to foretell the mechanical responses of the multiphase material system and reduce the trial manufacturing costs substantially, while computational expensive FEA are avoided. The developed atomic computation scheme, which provides the localized evaluation of the inelastic deformation or damage, provides a supplementary competency for the multiscale analysis within the micromechanics framework. While these simulations are of utmost importance to optimize the material system design, the localized data aid analyzers to find the microscale failure modes and to prevent or heal the damages at their initiation stage.

3.10 References

[1] Dvorak, G.J., On Uniform Fields in Heterogeneous Media. Proceedings of the Royal Society of London. Series A: Mathematical and Physical Sciences, 1990. 431(1881): p. 89-110.

[2] Dvorak, G.J., Transformation Field Analysis of Inelastic Composite Materials. Proceedings of the Royal Society of London. Series A: Mathematical and Physical Sciences, 1992. 437(1900): p. 311-327.

[3] Dvorak, G.J. and Y. Benveniste, On Transformation Strains and Uniform Fields in Multiphase Elastic Media. Proceedings of the Royal Society of London. Series A: Mathematical and Physical Sciences, 1992. 437(1900): p. 291-310.

[4] Seefried, C.G., J.V. Koleske, and F.E. Critchfield, Thermoplastic urethane elastomers. II. Effects of variations in hard-segment concentration. Journal of Applied Polymer Science, 1975. 19(9): p. 2503-2513.

[5] Brunette, C.M., S.L. Hsu, and W.J. MacKnight, Hydrogen-bonding properties of hard-segment model compounds in polyurethane block copolymers. Macromolecules, 1982. 15(1): p. 71-77.

[6] Ferguson, J., et al., Mechanical relaxations in a series of polyurethanes with varying hard to soft segment ratio. European Polymer Journal, 1972. 8(3): p. 369-383.

[7] Huh, D.S. and S.L. Cooper, Dynamic mechanical properties of polyurethane block polymers. Polymer Engineering & Science, 1971. 11(5): p. 369-376.

[8] Ferguson, J. and D. Patsavoudis, Chemical structure-physical property relationships in polyurethane elastomeric fibres; property variations in polymers containing high hard segment concentrations. European Polymer Journal, 1972. 8(3): p. 385-396.

[9] Ping, Peng, Wang, Wenshou, Chen, Xuesi and Jing, Xiabin, Poly(ε-caprolactone) Polyurethane and Its Shape-Memory Property†. Biomacromolecules, 2005. 6(2): p. 587-592.

[10] Kim, B.K., S.Y. Lee, and M. Xu, Polyurethanes having shape memory effects. Polymer, 1996. 37(26): p. 5781-5793.

[11] Rabani, G., H. Luftmann, and A. Kraft, Synthesis and characterization of two shape-memory polymers containing short aramid hard segments and poly([epsilon]-caprolactone) soft segments. Polymer, 2006. 47(12): p. 4251-4260.

[12] Niesten, M.C.E.J., J. Feijen, and R.J. Gaymans, Synthesis and properties of segmented copolymers having aramid units of uniform length. Polymer, 2000. 41(24): p. 8487-8500.

[13] Niesten, M. C. E. J., Harkema, S., van der Heide, E. and Gaymans, R. J., Structural changes of segmented copolyetheresteramides with uniform aramid units induced by melting and deformation. Polymer, 2001. 42(3): p. 1131-1142.

[14] Clough, S.B. and N.S. Schneider, Structural studies on urethane elastomers. Journal of Macromolecular Science, Part B, 1968. 2(4): p. 553-566.

[15] Clough, S.B., N.S. Schneider, and A.O. King, Small-angle X-Ray scattering from polyurethane elastomers. Journal of Macromolecular Science, Part B, 1968. 2(4): p. 641-648.

[16] Nemat-Nasser, S., Plasticity - A Treatise on Finite Deformation of Heterogeneous Inelastic Materials. 2004: Cambridge University Press.

[17] Kruch, S. and J.-L. Chaboche, Multi-scale analysis in elasto-viscoplasticity coupled with damage. International Journal of Plasticity, 2011. In Press, Corrected Proof, doi:10.1016/j.ijplas.2011.03.007.

[18] McDowell, D.L., A perspective on trends in multiscale plasticity. International Journal of Plasticity, 2010. 26(9): p. 1280-1309.

[19] Lissenden, C.J., Experimental investigation of initial and subsequent yield surfaces for laminated metal matrix composites. International Journal of Plasticity, 2010. 26: p. 1606-1628.

[20] Kruch, S. and J.L. Chaboche, Multi-scale analysis in elasto-viscoplasticity coupled with damage International Journal of Plasticity, 2011. In press.

[21] Nemat-Nasser, S. and M. Hori, Micromechanics: Overall Properties of Heterogeneous Materials. 1993, Amsterdam: Elsevier

[22] Ponte Castañeda, P., Second-order homogenization estimates for nonlinear composites incorporating field fluctuations: I--theory. Journal of the Mechanics and Physics of Solids, 2002a. 50(4): p. 737-757.

[23] Ponte Castañeda, P., Second-order homogenization estimates for nonlinear composites incorporating field fluctuations: II--applications. Journal of the Mechanics and Physics of Solids, 2002b. 50(4): p. 759-782.

[24] Balendran, B. and S. Nemat-Nasser, Bounds on elastic moduli of composites. Journal of the Mechanics and Physics of Solids, 1995. 43(11): p. 1825-1853.

[25] Eshelby, J.D., The Determination of the Elastic Field of an Ellipsoidal Inclusion, and Related Problems. Proceedings of the Royal Society of London. Series A. Mathematical and Physical Sciences, 1957. 241(1226): p. 376-396.

[26] Fotiu, P.A. and S. Nemat-Nasser, Overall properties of elastic-viscoplastic periodic composites. International Journal of Plasticity, 1996. 12(2): p. 163-190.

[27] Hori, M. and S. Nemat-Nasser, On two micromechanics theories for determining micro-macro relations in heterogeneous solids. Mechanics of Materials, 1999. 31(10): p. 667-682.

[28] Chaboche, J. L., Kruch, S., Maire, J. F. and Pottier, T., Towards a micromechanics based inelastic and damage modeling of composites. International Journal of Plasticity, 2001. 17(4): p. 411-439.

[29] Berveiller, M. and A. Zaoui, An extension of the self-consistent scheme to plastically-flowing polycrystals. Journal of the Mechanics and Physics of Solids, 1979. 26(5-6): p. 325-344.

[30] Hill, R., Continuum micro-mechanics of elastoplastic polycrystals. Journal of the Mechanics and Physics of Solids, 1965. 13(2): p. 89-101.

[31] Hutchinson, J.W., Bounds and Self-Consistent Estimates for Creep of Polycrystalline Materials. Proceedings of the Royal Society of London. A. Mathematical and Physical Sciences, 1976. 348(1652): p. 101-127.

[32] Chaboche, J.L., P. Kanoute, and A. Roos, On the capabilities of mean-filed approaches for the description of plasticity in metal matrix composites International Journal of Plasticity, 2005. 21: p. 1409-1434.

[33] Doghri, I., L. Adam, and N. Bilger, Mean-field homogenization of elasto-viscoplastic composites based on a general incrementally affine linearization method. International Journal of Plasticity, 2010. 26(2): p. 219-238.

[34] Doghri, I., et al., A second-moment incremental formulation for the mean-field homogenization of elasto-plastic composites. International Journal of Plasticity, 2011. 27(3): p. 352-371.

[35] Masson, R. and A. Zaoui, Self-consistent estimates for the rate-dependentelastoplastic behaviour of polycrystalline materials. Journal of the Mechanics and Physics of Solids, 1999. 47(7): p. 1543-1568.

[36] Chu, T.Y. and Z. Hashin, Plastic behavior of composites and porous media under isotropic stress. International Journal of Engineering Science, 1971. 9(10): p. 971-994.

[37] Masson, R., et al., An affine formulation for the prediction of the effective properties of nonlinear composites and polycrystals. Journal of the Mechanics and Physics of Solids, 2000. 48(6-7): p. 1203-1227.

[38] Feyel, F. and J.L. Chaboche, FE2 multi-scale approach for modelling the elasto-viscoplastic behaviour of long fiber SiC/Ti composite materials. Computer Methods in Applied Mechanics and Engineering 2000. 183: p. 309-330.

[39] Ghosh, S., Micromechanical Analysis and Multi-Scale Modeling Using the Voronoi Cell Finite Element Methods 2010: CRC Press.

[40] Voyiadjis, G.Z., A. Shojaei, and G. Li, A Generalized Coupled Viscoplastic- Viscodamage-Viscohealing Theory for Glassy Polymers. International Journal of Plasticity, 2012b. 28(1): p. 21-45.

[41] Voyiadjis, G. Z., Shojaei, A, Li, G. and Kattan, P.I., A Theory of Anisotropic Healing and Damage Mechanics of Materials. Proceeding of The Royial Society A, 2011a. available online: p. doi:10.1098/rspa.2011.0326.

[42] Voyiadjis, G.Z., A. Shojaei, and G. Li, A thermodynamic consistent damage and healing model for self healing materials. International Journal of Plasticity, 2011a. 27(7): p. 1025-1044.

[43] Li, G. and W. Xu, Thermomechanical behavior of thermoset shape memory polymer programmed by cold-compression: Testing and constitutive modeling. Journal of the Mechanics and Physics of Solids, 2011. 59(6): p. 1231-1250.

[44] Xu, W. and G. Li, Constitutive modeling of shape memory polymer based self-healing syntactic foam. International Journal of Solids and Structures, 2010. 47(9): p. 1306-1316.

[45] Lee, E.H., Closure to ``Discussion of `Elastic-Plastic Deformation at Finite Strains'" (1970, ASME J. Appl. Mech., 37, pp. 243--244). Journal of Applied Mechanics, 1970. 37(1): p. 244-244.

[46] Lee, E.H. and D.T. Liu, Finite-Strain Elastic---Plastic Theory with Application to Plane-Wave Analysis. Journal of Applied Physics, 1967. 38(1): p. 19-27.

[47] Lee, E.H., R.L. Mallett, and T.B. Wertheimer, Stress Analysis for Anisotropic Hardening in Finite-Deformation Plasticity. Closure to ``Discussion of `Elastic-Plastic Deformation at Finite Strains'" (1970, ASME J. Appl. Mech., 37, pp. 243--244). Journal of Applied Mechanics, 1983. 50(3): p. 554-560.

[48] Kleiber, M., Kinematics of deformation processes in materials subjected to finite elastic-plastic strains. International Journal of Engineering Science, 1975. 13(5): p. 513-525.

[49] Green, A.E. and P.M. Naghdi, A general theory of an elastic-plastic continuum. Archive for Rational Mechanics and Analysis, 1965. 18(4): p. 251-281.

[50] Naghdi, P.M. and J.A. Trapp, RESTRICTIONS ON CONSTITUTIVE EQUATIONS OF FINITELY DEFORMED ELASTIC-PLASTIC MATERIALS. The Quarterly Journal of Mechanics and Applied Mathematics, 1975. 28(1): p. 25-46.

[51] Nagtegaal, J.C. and J.E. De Jong, Some computational aspects of elastic-plastic large strain analysis. International Journal for Numerical Methods in Engineering, 1981. 17(1): p. 15-41.

[52] Simo, J.C. and T.J.R. Hughes, Computational Inelasticity. 1997, New York: Springer.

[53] Nemat-Nasser, S., Decomposition of strain measures and their rates in finite deformation elastoplasticity. International Journal of Solids and Structures, 1979. 15(2): p. 155-166.

[54] Nemat-Nasser, S., On finite deformation elasto-plasticity. International Journal of Solids and Structures, 1982. 18(10): p. 857-872.

[55] Nemat-Nasser, S. and T. Iwakuma, Elastic-plastic composites at finite strains. International Journal of Solids and Structures, 1985. 21(1): p. 55-65.

[56] Green, A.E. and P.M. Naghdi, Some remarks on elastic-plastic deformation at finite strain. International Journal of Engineering Science, 1971. 9(12): p. 1219-1229.

[57] Nemat-Nasser, S., Plasticity: A Treatise on Finite Deformation of Heterogeneous Inelastic Materials. 2006, Cambridge: Cambridge University Press.

[58] Marsden, J.E. and T.J.R. Hughes, Mathematical Foundation of Elasticity. 1983, New Jersey: Prentice-Hall.

[59] Simo, J.C. and M. Ortiz, A unified approach to finite deformation elastoplastic analysis based on the use of hyperelastic constitutive equations. Computer Methods in Applied Mechanics and Engineering, 1985. 49(2): p. 221-245.

[60] Lee, B.J., D.M. Parks, and S. Ahzi, Micromechanical modeling of large plastic deformation and texture evolution in semi-crystalline polymers. Journal of the Mechanics and Physics of Solids, 1993. 41(10): p. 1651-1687.

[61] Mikdam, A., Makradi, A., Ahzi, S., Garmestani, H., Li, D. S. and Remond, Y., Effective conductivity in isotropic heterogeneous media using a strong-contrast statistical continuum theory. Journal of the Mechanics and Physics of Solids, 2009. 57(1): p. 76-86.

[62] Boyce, M.C., D.M. Parks, and A.S. Argon, Plastic flow in oriented glassy polymers. International Journal of Plasticity, 1989. 5(6): p. 593-615.

[63] Ayoub, G., Zaïri, F., Naït-Abdelaziz, M. and Gloaguen, J. M., Modelling large deformation behaviour under loading-unloading of semicrystalline polymers: Application to a high density polyethylene. International Journal of Plasticity, 2010. 26(3): p. 329-347.

[64] Regrain, C., Laiarinandrasana, L., Toillon, S. and Saï, K., Multi-mechanism models for semi-crystalline polymer: Constitutive relations and finite element implementation. International Journal of Plasticity, 2009. 25(7): p. 1253-1279.

[65] Parks, D.M. and S. Ahzi, Polycrystalline plastic deformation and texture evolution for crystals lacking five independent slip systems. Journal of the Mechanics and Physics of Solids, 1990. 38(5): p. 701-724.

[66] G'Sell, C. and A. Dahoun, Evolution of microstructure in semi-crystalline polymers under large plastic deformation. Materials Science and Engineering: A, 1994. 175(1-2): p. 183-199.

[67] Bowden, P.B. and R.J. Young, Deformation mechanisms in crystalline polymers. Journal of Materials Science, 1974. 9(12): p. 2034-2051.

[68] Ahzi, S., D.M. Park, and A.S. Argon, Estimats of the overall elastic properties in semi-crystalline polymers. AMD- Vol. 203, Current Research in the Thermo-Mechanics of Polymers in the Rubbery-Glassy Range 1995: p. 31-44.

[69] Schoenfeld, S.E., S. Ahzi, and R.J. Asaro, Elastic-plastic crystal mechanics for low symmetry crystals. Journal of the Mechanics and Physics of Solids, 1995. 43(3): p. 415-446.

[70] Lin, L. and A.S. Argon, Rate Mechanism of Plasticity in the Crystalline Component of Semicrystalline Nylon 6. Macromolecules, 1994. 27(23): p. 6903-6914.

[71] Ward, I.M. and J. Sweeney, An Introduction to the Mechanical Properties of Solid Polymers. 2004: John Wiley & Sons.

[72] Barham, P.J. and R.G.C. Arridge, A fiber composite model of highly oriented polyethylene. Journal of Polymer Science: Polymer Physics Edition, 1977. 15(7): p. 1177-1188.

[73] Stevenson, A., Effetc of crystallization on the mechanical properties of elastomers under large deformation in Current Research in the Thermo-Mechanics of Polymers in the Rubbery-Glassy Range. 1995, ASME.

[74] Asaro, R.J., Geometrical effects in the inhomogeneous deformation of ductile single crystals. Acta Metallurgica, 1979. 27(3): p. 445-453.

[75] Asaro, R.J. and A. Needleman, Overview no. 42 Texture development and strain hardening in rate dependent polycrystals. Acta Metallurgica, 1985. 33(6): p. 923-953.

[76] Asaro, R.J. and J.R. Rice, Strain localization in ductile single crystals. Journal of the Mechanics and Physics of Solids, 1977. 25(5): p. 309-338.

[77] Argon, A.S., A theory for the low-temperature plastic deformation of glassy polymers. Philosophical Magazine, 1973. 28(4): p. 839 – 865.

[78] Boyce, M.C., D.M. Parks, and A.S. Argon, Large inelastic deformation of glassy polymers. part I: rate dependent constitutive model. Mechanics of Materials, 1988. 7(1): p. 15-33.

[79] Boyce, M.C. and E.M. Arruda, An experimental and anaiytical investigation of the large strain compressive and tensile response of glassy polymers. Polymer Engineering & Science, 1990. 30(20): p. 1288-1298.

[80] Boyce, M.C., D.M. Parks, and A.S. Argon, Large inelastic deformation of glassy polymers. Part II: numerical simulation of hydrostatic extrusion. Mechanics of Materials, 1988. 7(1): p. 35-47.

[81] Dupaix, R.B. and M.C. Boyce, Constitutive modeling of the finite strain behavior of amorphous polymers in and above the glass transition. Mechanics of Materials, 2007. 39(1): p. 39-52.

[82] Arruda, E.M. and M.C. Boyce, Evolution of plastic anisotropy in amorphous polymers during finite straining. International Journal of Plasticity, 1993. 9(6): p. 697-720.

[83] Arruda, E.M. and M.C. Boyce, A three-dimensional constitutive model for the large stretch behavior of rubber elastic materials. Journal of the Mechanics and Physics of Solids, 1993. 41(2): p. 389-412.

[84] Arruda, E.M., M.C. Boyce, and H. Quintus-Bosz, Effects of initial anisotropy on the finite strain deformation behavior of glassy polymers. International Journal of Plasticity, 1993. 9(7): p. 783-811.

[85] Dvorak, G.J. and J. Zhang, Transformation field analysis of damage evolution in composite materials. Journal of the Mechanics and Physics of Solids, 2001. 49(11): p. 2517-2541.

[86] Hamelin, C.J., B.J. Diak, and A.K. Pilkey, Multiscale modelling of the induced plastic anisotropy in bcc metals. International Journal of Plasticity, 2011. 27(8): p. 1185-1202.

[87] Hasanpour, K., S. Ziaei-Rad, and M. Mahzoon, A large deformation framework for compressible viscoelastic materials: Constitutive equations and finite element implementation. International Journal of Plasticity, 2009. 25(6): p. 1154-1176.

[88] Lee, M. G., Lim, H., Adams, B. L., Hirth, J. P. and Wagoner, R. H., A dislocation density-based single crystal constitutive equation. International Journal of Plasticity, 2010. 26(7): p. 925-938.

[89] Moorthy, S. and S. Ghosh, Particle cracking in discretely reinforced materials with the voronoi cell finite element model. International Journal of Plasticity, 1998. 14(8): p. 805-827.

[90] Watanabe, O., H.M. Zbib, and E. Takenouchi, Crystal plasticity: micro-shear banding in polycrystals using voronoi tessellation. International Journal of Plasticity, 1998. 14(8): p. 771-788.

[91] Hershey, A.V., The elasticity of an isotropic aggeregate of anisotropic cubic crystal Journal of Applied Mechanics, 1954. 21: p. 236-241.

[93] Simo, J.C. and R.L. Taylor, A return mapping algorithm for plane stress elastoplasticity. International Journal for Numerical Methods in Engineering, 1986. 22(3): p. 649-670.

[94] Simo, J.C. and K.S. Pister, Remarks on rate constitutive equations for finite deformation problems: computational implications. Computer Methods in Applied Mechanics and Engineering, 1984. 46(2): p. 201-215.

[95] Simo, J.C., R.L. Taylor, and K.S. Pister, Variational and projection methods for the volume constraint in finite deformation elasto-plasticity. Computer Methods in Applied Mechanics and Engineering, 1985. 51(1-3): p. 177-208.

[96] G'Sell, C., Dislocations in glassy polymers do they exist? Are they useful? Materials Science and Engineering A, 2001. 309-310: p. 539-543.

[97] Fung, Y.C. and P. Tong, Classical and Computational Solid Mechanics. Vol. 1. 2001, Singapore: World Scientific.

[98] Lee, B.J., S. Ahzi, and R.J. Asaro, On the plasticity of low symmetry crystals lacking five independent slip systems. Mechanics of Materials, 1995. 20(1): p. 1-8.

[99] Tobushi, H., Hashimoto, T., Hayashi, S. and Yamada, E., Thermomechanical Constitutive Modeling in Shape Memory Polymer of Polyurethane Series. Journal of Intelligent Material Systems and Structures, 1997. 8(8): p. 711-718.

CHAPTER 4 A MULTISCALE VISCOPLASTIC THEORY OF SHAPE MEMORY POLYMER FIBERS*

4.1 Nomenclature

$A_{ij}^{(\alpha)}$ skwe-symmetry part of the Schmid tensor

$A_{ijkl}^{(r)}$ strain concentration tensor

$B_{ijkl}^{(r)}$ stress concentration tensor

c_i crystallographic axes vector

d_{ij} Lagrangian strain tensor

d_{ij}^{e} Lagrangian elastic strain tensor

d_{ij}^{p} Lagrangian plastic strain tensor

D_{ij} Eulerian strain tensor

D_{ij}^{e} Eulerian elastic strain tensor

D_{ij}^{p} Eulerian plastic strain tensor

$\dot{D}_{ij}^{c}$ inelastic crystalline stretch rate tensor

F_{ij} total deformation gradient tensor

F_{ij}^{e} elastic deformation gradient tensor

F_{ij}^{p} plastic deformation gradient tensor

L_{ij}^{c} crystalline velocity gradient tenor

L_{ijkl} stiffness tensor

M_{ijkl} compliance tensor

σ_{ij} Cauchy stress tensor

ϵ_{ij} strain tensor

* Accepted paper in PROCEEDINGS OF THE ROYAL SOCIETY A

τ_{ij}^{p} first Piola-Kirchhoff tensor

$\tau^{(\alpha)}$ crystalline phase Cauchy shear stress, associated with the αth slippage system

$|\tau|$ amorphous phase shearing stress

μ shear modulus

ν Poisson's ratio

α_{ij} amorphous phase back stress tensor

X_{ij} amorphous phase deviatoric back stress tensor

S_{ij}^{p} second Piola-Kirchhoff tensor

S_{ij}^{c} deviatoric Cauchy stress tensor

S_{ij}^{c*} crystalline deviatoric Cauchy stress tensor, projected at the c_i direction

S_{ij}^{cp} deviatoric Cauchy stress tensor, projected perpendicular to the c_i direction

s_{ij}^{*} driving stress tensor in the amorphous phase

s amorphous athermal shear strength

R_{ij} rotation tenor

U_{ij} stretch tensor

$R_{ij}^{(\alpha)}$ symmetric part of the Schmid tensor

$\dot{\gamma}^{(\alpha)}$ crystalline shearing strain rate associated with αth slippage system

$|\dot{\gamma}^{p}|$ amorphous shearing strain rate

W_{ij}^{c} spin tensor

W_{ij}^{c*} lattice spin tensor

4.2 Introduction

Damage healing in thermoset polymer composite structures has become a popular topic recently [1]. Several healing schemes have been reported in the literature primarily for healing microcracks with narrow opening, including incorporation of external healing agent such as liquid healing agent by microcapsules [2], hollow fibers [3], and microvascular networks [4], and solid healing agent such as

embedded thermoplastic particles [5, 6]. Some polymers such as ionomers [7, 8] and thermally reversible covalent bonds (TRCB) [9] by themselves possess healing capabilities. A combination of microcapsule and shape memory alloy (SMA) wire has also been studied [10]. Because some damages, such as impact damages, are usually in the structural-length scale, the main challenge to heal these macrocracks remains the closure of such a wide opening. The existing healing systems are unable to very effectively heal macroscopic cracks. For instance, in the case of the microencapsulated liquid healing agent, a large amount of healing agent is needed in order to heal macrocracks. However, incorporation of a large amount of healing agent will significantly alter the physical/mechanical properties of the host structure. Also, large capsules/thick hollow fibers themselves may become potential defects when the encased healing agent is released. For ionomers and TRCB polymers, they need external help to bring the fractured surfaces in contact before chemical bonds can be established. While Kirkby et al. [10] proposed a very smart idea, one limitation is that the SMA is expensive, heavy weight, and most critically, its recovery force cannot be effectively transferred because the polymer matrix becomes soft at the SMA recovery temperature while the SMA is very stiff. Also, the "run-off" of the liquid monomer in wide-opened crack is another challenge before polymerization occurs. Therefore, the grand challenge facing the scientific community is how to heal structural-length scale damage such as impact damage repeatedly, efficiently, and molecularly.

Recently, a bio-mimetic healing scheme has been proposed and validated to repeatedly and molecularly heal macroscopic crack [11-13]. It utilizes the confined shape recovery of the SMP matrix for the purpose of sealing or closing cracks and the incorporated thermoplastic particles for molecular length-scale healing. The key for the success of this scheme is that the volume of the SMP matrix must be reduced during programming and external confinement must be provided during shape recovery [11]. It has been proved that volume reduction can be realized through compression programming [11, 14] and external confinement can be provided through architectural design of composite structures such as grid stiffened SMP cored sandwich [15], 3-D woven fabric reinforced SMP composite [16], or even the sandwich skin [17]. In order to speed up the programming process, cold-compression programming of thermoset SMP has been proposed, tested, and modeled [18]. However, this bio-inspired scheme cannot be extended to healing of conventional thermoset polymers because regular thermoset polymers do not have the shape memory capabilities.

In order to repeatedly and molecularly heal macroscopic cracks in conventional thermoset polymers, we propose a new bio-mimetic scheme: a SMP fiber z-pinned, continuous SMP fiber reinforced polymer grid skeleton that is filled in with conventional thermosetting polymer dispersed with thermoplastic particles. We envision the proposed composite will work similar to the two-step healing of human skin: close then heal (CTH), i.e., close the wound by bleeding and clotting or surgery (suture or sew the skin together) before new cells gradually grow. Particularly, we propose to use the constrained shape recovery of SMP ribs and z-pins for the purpose of narrowing/closing the macroscopic crack (Step 1) and molten thermoplastic particles for healing molecularly (Step 2). The basic idea is that the SMP fibers are strain hardened through cold-drawing programming before fabrication. When an impact is identified (by surface indentation, portable non-destructive testing such as ultrasound, etc.), localized

heating surrounding the impact damaged bay(s) or cell(s) will be conducted using contact or non-contact heating such as infrared light. Once the local temperature in the SMP ribs and z-pins are higher than the transition temperature, the SMP ribs and z-pins surrounding the damaged bay(s) remember their original shape and tend to shrink. Due to the constraints by the neighboring "cold" bays (which have high stiffness), the shrinkage of the SMP ribs and z-pins are not free. A 3-D compressive force will be applied to the boundary of the damaged bay(s), leading to narrowing or closing of the cracks with wide opening. This is the Step 1 of the bio-mimetic scheme. Further heating leads to melting of the embedded thermoplastic particles, and the molten thermoplastic will be sucked into the narrowed crack through capillary force and diffused into the fractured thermoset polymer matrix due to concentration gradient and recovery compressive force. When cooling down, the thermoplastic hardens and glues the crack molecularly. This completes one molecular damage-healing cycle. As indicated by Li and Uppu [41], each constrained shape recovery process also represents a new training cycle to the SMP ribs and z-pins, suggesting that SMP fibers only need to be programmed one time before fabrication. Subsequent programming will be autonomous by coupling with shape recovery (healing) of the sandwich. Together with the fact that the thermoplastic particles can also be repeatedly melted and hardened, the damage-healing cycle is repeatable. The working principle can be visualized by Fig. 4-2. It is noted that while the bio-inspired self-healing is cited as two steps, it actually just needs one step in practice – heating up all the way to the melting temperature of the thermoplastic particles; the SMP ribs and z-pins will shrink during the course of heating. In Fig. 4-1, T_g denotes the glass transition temperature of the SMP fiber; T_m represents the melting temperature of thermoplastic particles (TPs); T_{gp} indicates the glass transition temperature of the thermoset polymer; and T_c denotes the curing temperature of the thermoset polymer. The basic requirement for the designed healing system is: $T_{gp}>T_m>T_g>T_c$ (Color change visualizes temperature change in the figure).

In order to validate the healing scheme in Fig. 4-1, a finite element analysis was conducted on a SMP orthogrid stiffened thermoset polymer composite; see a schematic in Fig. 4-2(a). The central bay in Fig. 4-2(a) contains a macroscale crack which is an ellipsoidal hole with major diameter of 20 mm, minor diameter of 5 mm, and height of 5 mm. Heating is conducted locally on the central bay and its surrounding four ribs. The following parameters were assumed: the SMP fiber reinforced rib has a modulus of 600MPa and maximum recovery stress of 10MPa, and the polymer composite in the bay has a modulus of 1,000MPa. Solid Tetrahedral elements with 10 nodes are used with the number of elements of 8,420. Once the localized recovery stresses overcome the stiffness of the bay the walls of the crack is collapsed together, as shown in magnified view in Fig. 4-2(b). Also the displacement field in Y direction is shown in Fig. 4-2(b), which confirms that the walls of the crack march towards each other due to the applied localized stresses from the SMP ribs. Fig 4-2(c) to 4-2(f) show respectively the normal stress at x, y directions and shear stress τ_{xy} and von-Mises equivalent stress. The state of stress confirms that the recovered stresses are within yield limit of the matrix and they will not cause more damages. Furthermore, due to the elevated temperature the matrix is expected to be softened and released stresses by SMP fibers will not induce any further damage within the material system. A more elaborated FEA simulation can address the stress singularities at the crack tip during the closing process.

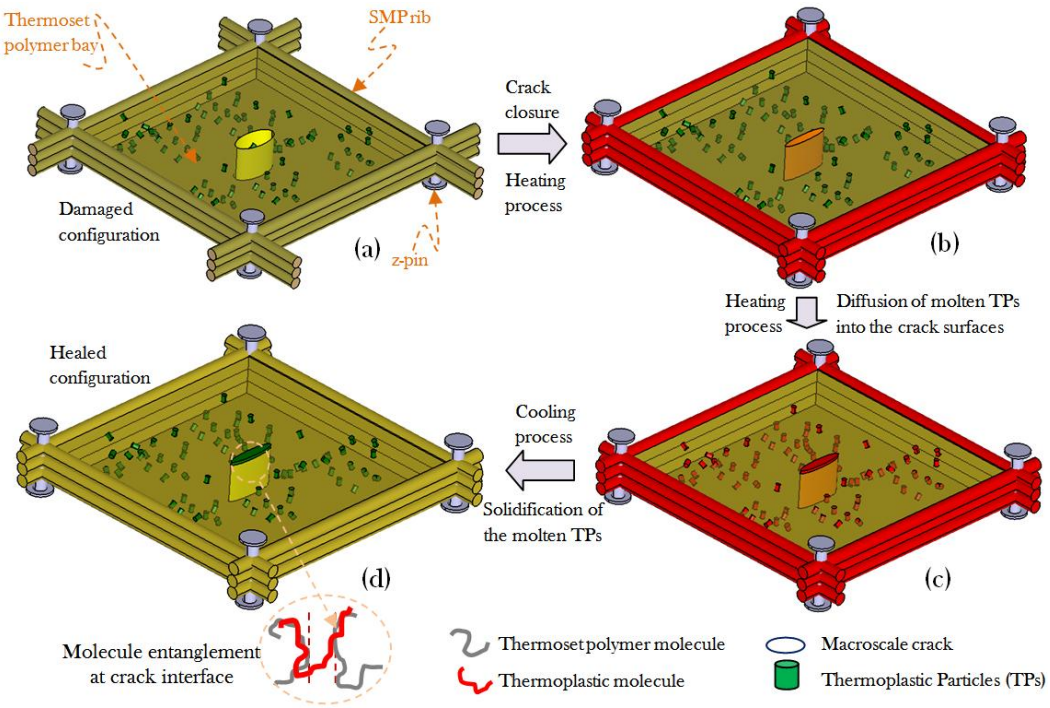

Figure 4-1 Schematic of the bio-inspired healing process of the proposed composite (3-D view) (a) a unit cell (bay) of SMP grid (ribs and z-pins) stiffened conventional thermoset polymer dispersed with thermoplastic particles. A macroscopic crack is introduced in the unit cell, which can be identified by visual or non-destructive inspections(T< Tg), (c) crack closure process through recovery of the SMP fiber ribs and z-pins, when local heating is applied (T> Tg), (d) further temperature rising melts the thermoplastic particles which flow into the crack by capillary force and diffuse into the fractured surface by concentration gradient (T> Tm), (e) cooling down to below the glassy temperature, solid wedge can be formed and molecular entanglement will be established (T< Tg), magnified view shows the molecule entanglement at the crack interface.

It is noted that, as compared to the previous bio-mimetic healing scheme proposed by Li and Uppu (2010), the scheme illustrated in Fig. 4-1 has fundamental differences and is considered to be more realistic and feasible. The comparisons are summarized in Table 4-1.

Currently, SMP fibers are primarily made of thermoplastic SMPs, particularly polyurethane [19].The polyurethane semicrystalline SMP fibers are constituted from the crystalline hard phase and amorphous soft phase and they show excellent solution ability, melting, diffusion, processability, and repeatability of the Shape Memory (SM) cycle [20]. Soft segment may consist of the amorphous (e.g. polyester and polyether) or the semi-crystalline (e.g. poly(ε-caprolactone) (PCL)) structures while the hard segments (e.g. diisocyanate (TDI), aromatic urethane or aramid) may be dispersed over the soft segment to form thermally stable chemical or physical cross links .

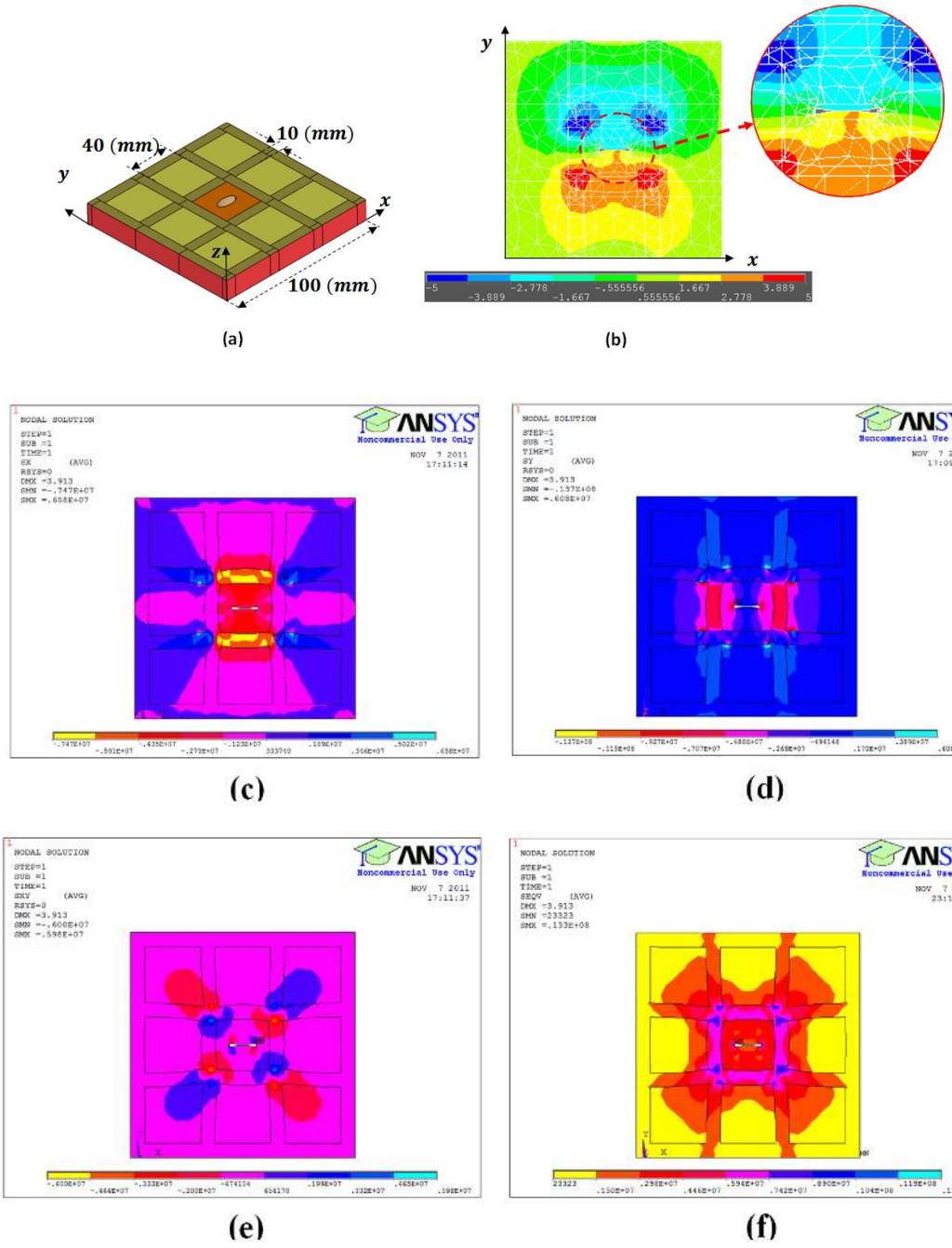

Figure 4-2 Closing of macroscopic crack due to shape recovery of the SMP grid skeleton through localized heating , (a) a SMP orthogrid stiffened thermoset polymer composite with a macroscopic crack at the center of the central bay, (b) FEA results for the displacement field at Y direction when stored stresses in SMP fibers are released by a local heating process. Magnified view shows closure of the macroscopic crack, (c) normal stress at x direction, (d) normal stress at y direction, (e) shear stress in xy plane, (f) equivalent von-Mises stress.

Table 4-1 Fundamental difference between the previous study and the current study

Items for comparison	Previous bio-mimetic scheme proposed by [11]	The current study
Matrix	SMP.	Conventional thermosetting polymer.
Fiber	No.	Yes. Continuous SMP fiber.
Programming	Volume reduction by compression.	Strain hardening by cold-tension.
Mechanism for crack closing	Confined shape recovery by resisting free expansion of the SMP matrix (need external confinement).	Constrained shape recovery by resisting free shrinking of SMP grid skeleton (does not need external confinement).
Cost	High. Large volume fraction of SMP as the continuous phase.	Low. Small volume fraction of SMP fibers as the dispersed phase.

Existence of the distinguishable hard phases in the polyurethane elastomers provides the physical basis for a micromechanics approach toward the multiscale analysis of these materials [21-23]. The stress induced crystallization process in the semicrystalline polymers has been well studied in the literature [24, 25]. Accordingly during this process, the spherulite morphology is changed upon stretching and the crystalline molecular chains orient in the direction of the applied macroscopic loads. In the case of polyurethane SMP fibers, this process results in the enhanced mechanical properties along the fiber direction.

In this work, we will experimentally investigate the strain hardening of polyurethane fibers through cold-drawing programming, in order to achieve the required recovery stress in Fig. 4-2. We will then investigate the thermomechanical cycle (programming and shape recovery) of the strain-hardened SMP fibers. Microstructure change and anisotropic behavior due to programming will be examined by Polarized Optical Microscope (POM), Fourier Transform Infrared Spectroscopy (FTIR), Small Angle X-ray Scattering (SAXS), and Dynamic Mechanical Analysis (DMA). After that, a Representative Volume Element (RVE) is utilized to correlate the microstructure of the SMP fiber to the macroscopic loading conditions. The soft and hard segments are assumed to follow respectively the amorphous and crystalline constitutive relations. The well-established micromechanics averaging techniques are then incorporated to average the micro-stress and micro-strain fields in these sub-phases and the macroscale mechanical response of the SMP fiber is then estimated. This approach was proposed formerly by Eshelby and later it has been developed to the Mori-Tanaka and self-consistent methods [26, 27]. The local-global relations between the applied macroscale and the resulting microscale mechanical fields can be established analytically when the medium behaves elastically. Once the non-linearity is introduced in

one of the sub-phases a history dependent solution algorithm should be enforced in order to update these relations. Shojaei and Li discussed in detail the solution algorithm for such a multiscale analysis incrementally [23]. In section 2 experimental characterizations of the SMP fibers are discussed. In section 3 the constitutive relations for the amorphous and crystalline phases together with the texture updates are elaborated. Furthermore, the constitutive relations for the stress recovery and the stress induced crystallization process are proposed. In section 4 the kinematics of the finite deformation together with the required numerical algorithms are elaborated. In section 5 simulation results are presented.

4.3 Experimental characterization of shape memory polymer fibers

In this study, polyurethane was synthesized from poly(butylene adipate)-600 (Mn) (PBA), 4'4 - diphenylmethane diisocyanate (MDI) and 1,4-butanediol (BDO). On average, the mole ratio of (MDI+BDO): PBA=3:1. The average formula weight ratio of (MDI+BDO): PBA=1021:650. The hard segment, soft segment, and their contents were selected to prepare polyurethane with amorphous soft segment phase and crystalline hard segment phase. The polyurethane fiber was spun by melt spinning. The fiber passed three pairs of rollers with the same rotation speed before being wound up. In this work two types of single SMP fibers (filaments) are characterized in which their microstructure changes upon cold drawing process are evaluated. Fig. 4-3 shows the optical microscopy picture for a single SMP fiber with an initial diameter of 0.04 mm, which is called sample #1 hereinafter. The non-stretched SMP fiber #1 is shown in Fig. 4-3(a) in which the microstructure of the fiber is almost random; when the fiber is highly stretched, the microstructure aligns along the fiber direction, see Fig. 4-3(b). Fig. 4-4 shows similar pictures for the SMP fiber with an initial diameter of 0.002 mm, which is denoted as sample #2 hereinafter. The oriented microstructures along the fiber direction are obvious when the fiber is cold drawn as shown in Fig. 4-4(b). The samples #1 and #2 are respectively cyclic stretched up to 350 % and 200% level of strains before taking the pictures in Figs. 4-3(b) and 4-4(b).

Using an MTS Alliance RT/5 machine, which is specified for fiber tension tests, the SMP fiber #1 is cyclically stretched and the results are shown in Fig. 4-5(a). The elastic stiffness of the SMP fiber is increased gradually while the final strength of the fiber is increased significantly. Obviously, cyclic cold-drawing leads to strain hardening of the SMP fibers. The reason for this is the alignment of the amorphous phase and crystalline phase along the loading direction up on cold-tension, as evidenced in Figs. 4-3 and 4-4.

The fully constrained (zero strain) stress recovery response of these fibers with respect to time is depicted in Fig. 4-6. In this process the programmed fiber is kept by the load cells while the heating process is controlled by a digital furnace. An initial stretch within the elastic region, e.g. $\epsilon = 10\ \%$, is applied to ensure that the fibers remain zero strain before the shape recovery process starts, which needs a temperature rising process and causes thermal expansion and thus loose of the fiber between the grips. It is worthwhile to note that this pre-stretch is found in a *trial-and-error* process in which the stress recovery is set to start from almost zero stress. In fact both of these fibers show a sudden stress

relaxation before activation of the shape recovery process. In other words, the pre-tension is fully consumed by the stress relaxation and thermal expansion before the stress recovery starts.

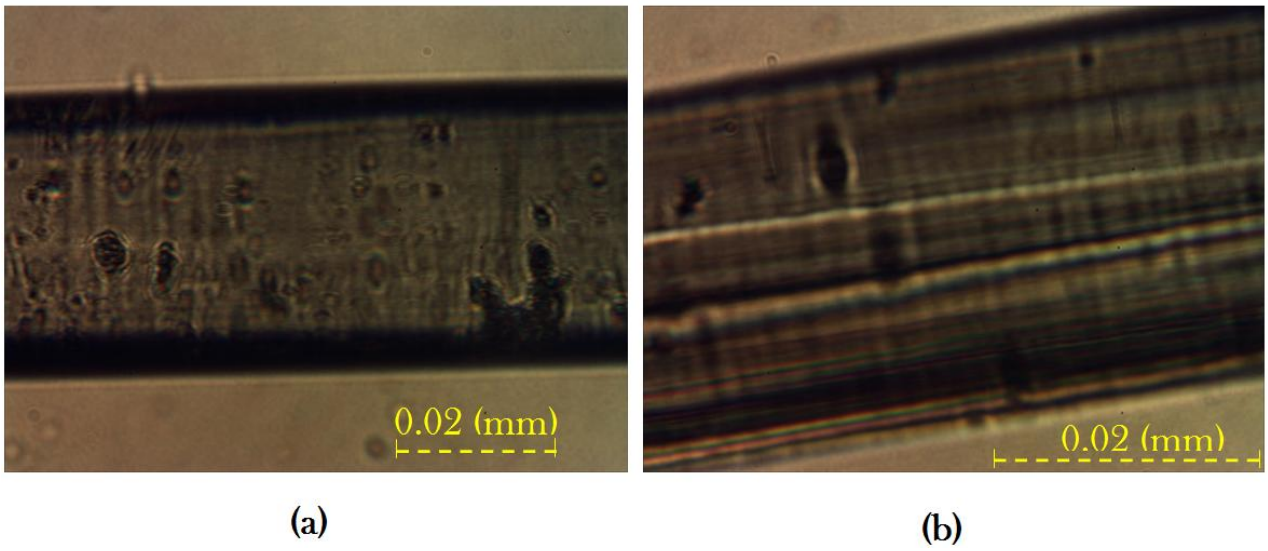

Figure 4-3 Polarized optical microscope image of the side view of the SMP fiber sample #1 with 0.04mm diameter (a) non-stretched fiber and (b) after 3rd cyclic load where the sample is stretched up to 350% of strain level

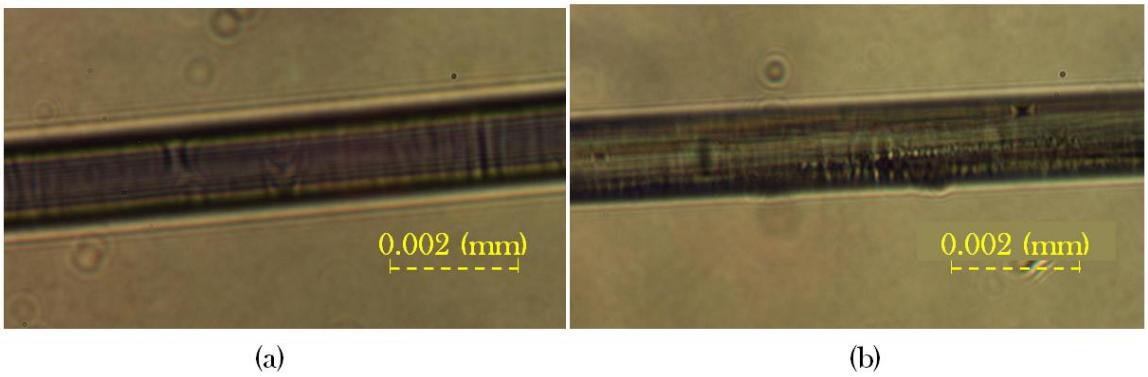

Figure 4-4 Polarized optical microscope image of the side view of the SMP fiber sample #2 with 0.002 mm diameter (a) non-stretched fiber and (b) after 3rd cyclic load where the sample is stretched up to 200% of strain level

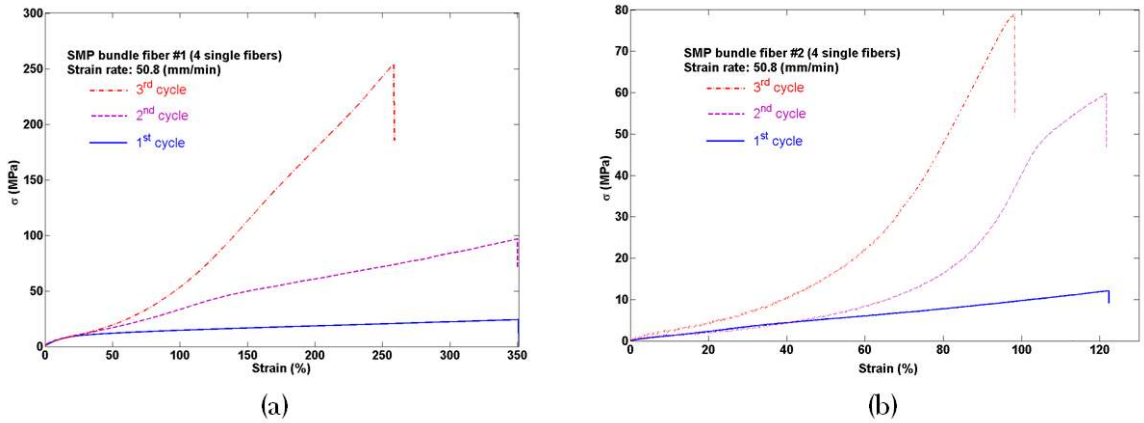

Figure 4-5 Cyclic loading tests for a bundle of SMP fibers (a) 4 simple fiber #1 and (b) 4 simple fiber #2.

Therefore, the pre-stretch does not affect the stress recovery. In this study, the heating rate is 0.35 ^{o}C/sec and the final temperature is set to 90 ^{o}C in the digital furnace. From Fig. 4-6, the pre-tension stress is relaxed to zero at about 20 s. Because the starting temperature of the fiber is about 20^{o}C, the temperature becomes 30^{o}C after 20s of heating. As shown in Fig. 4-7, this is the temperature when the glass transition starts. Therefore, as expected, the 10% pre-tension is fully used up by stress relaxation and thermal expansion of the fiber. The pre-stretch is a technique to compensate for the inability for the machine to measure the stress when the fiber is loose.

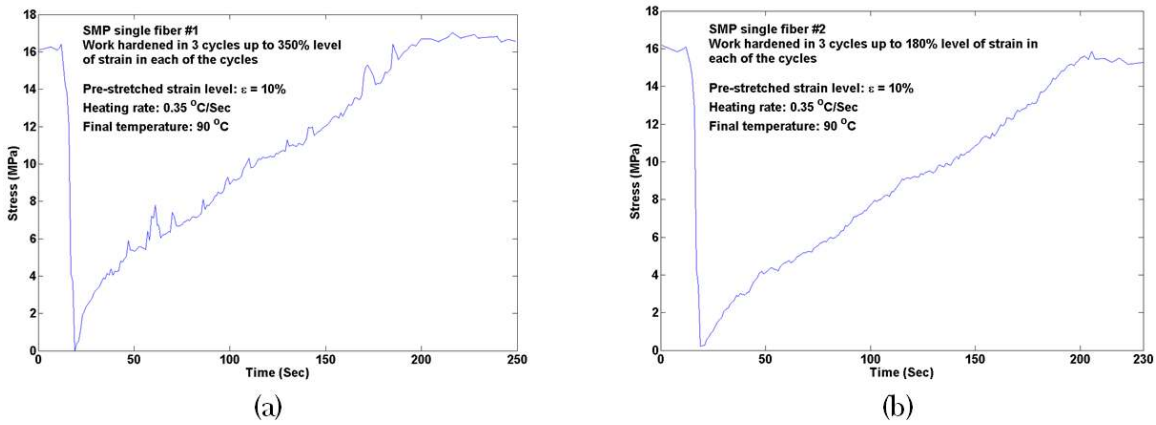

Figure 4-6 Stress recovery test results with heating rate 0.35 oC/Sec and up to 90 oC (a) SMP fiber #1 after 3 strain controlled cyclic loads each of them up to 350% of the strain level with 50.8 (mm/min) strain rate, and (b) SMP fiber #2 after 3 strain controlled cyclic loads each of them up to 180% of the strain level with 50.8 (mm/min) strain rate

From Fig. 4-6, the stabilized recovery stress is about 16MPa. Based on Fig. 4-2, it is seen that the fiber after cyclic cold-drawing programming is able to provide the required recovery stress (10MPa in Fig. 4-2) for close the macroscopic crack. We also tested the stress recovery of non-stretched (as received) SMP fiber using the same procedure. The stress recovery is almost zero.

Fig. 4-7 shows the DMA experiments (with heating rate 5^{o}C/min and frequency 1 Hertz) in which both the non-stretched and cold-drawn SMP fibers #1 are tested to investigate the changes in their glass transition temperature, T_g, upon work hardening process. The SMP fiber#1 with 30mm length and initial diameter of 0.04 mm is mounted on the DMA machine (Rheometric Scientific, RSA III) at room temperature. Fig. 4-7 (a), the cold-drawn SMP fiber shows a small shift in its T_g towards higher temperature. The glass transition starts at about 30^{o}C, which echoes the claim in Fig. 4-6. From Fig. 4-7 (b), it is clear that the storage modulus of the strain hardened SMP fibers is much higher than the as received counterparts, and plateaus in a wide range of temperature, suggesting significant increase in stiffness and its thermal stability. Fig. 4-7(c) shows the loss modulus experimental results.

In order to better understand the microstructure due to strain hardening by cold-drawing, the change in the microstructure of the SMP fiber is further investigated.

Using TENSOR 27, the Fourier Transform Infrared Spectroscopy (FTIR) test is implemented on two samples to check the microstructural changes during cold stretching process of SMP fibers. Fig. 4-8 shows the FTIR test results for the sample #2 in which the blue line shows the non-stretched SMP fiber #2 and the red line represents the SMP fiber #2 which is stretched up to 180% strain level prior to the FTIR test. The synchronized peaks confirm that the chemical compositions of the two fibers are the same and there are no new chemical bonds upon cold drawing. The change in the intensity after strain hardening by cold-drawing programming may indicate the change in density and molecular alignment.

Using Small Angle X-ray Scattering (SAXS) facilities in the Center for Advanced Microstructures and Devices (CAMD) at Louisiana State University the microstructure of the non-stretched and stretched SMP fibers (sample #1) is investigated. As shown in Fig. 4-9(a) the SAXS image for the non-stretched fiber shows a non-oriented microstructure while in the case of the stretched fiber, the SAXS image shows orientational changes in the microstructure in Fig. 4-9(b).

Based on the above test results and microstructural examination, it is evident that both the soft segments and hard segments in the semicrystalline SMP fiber align along the loading direction after cyclic cold-drawing programming, which also leads to considerable increase in stress recovery. This suggests that the polyurethane fibers, after strain hardening through cold-drawing programming, may have a potential to be used in load-bearing structural applications, particularly in the bio-mimetic healing scheme proposed in Fig. 4-1. However, an in-depth understanding of the thermomechanical behavior of the semicrystalline polyurethane fiber needs constitutive modeling.

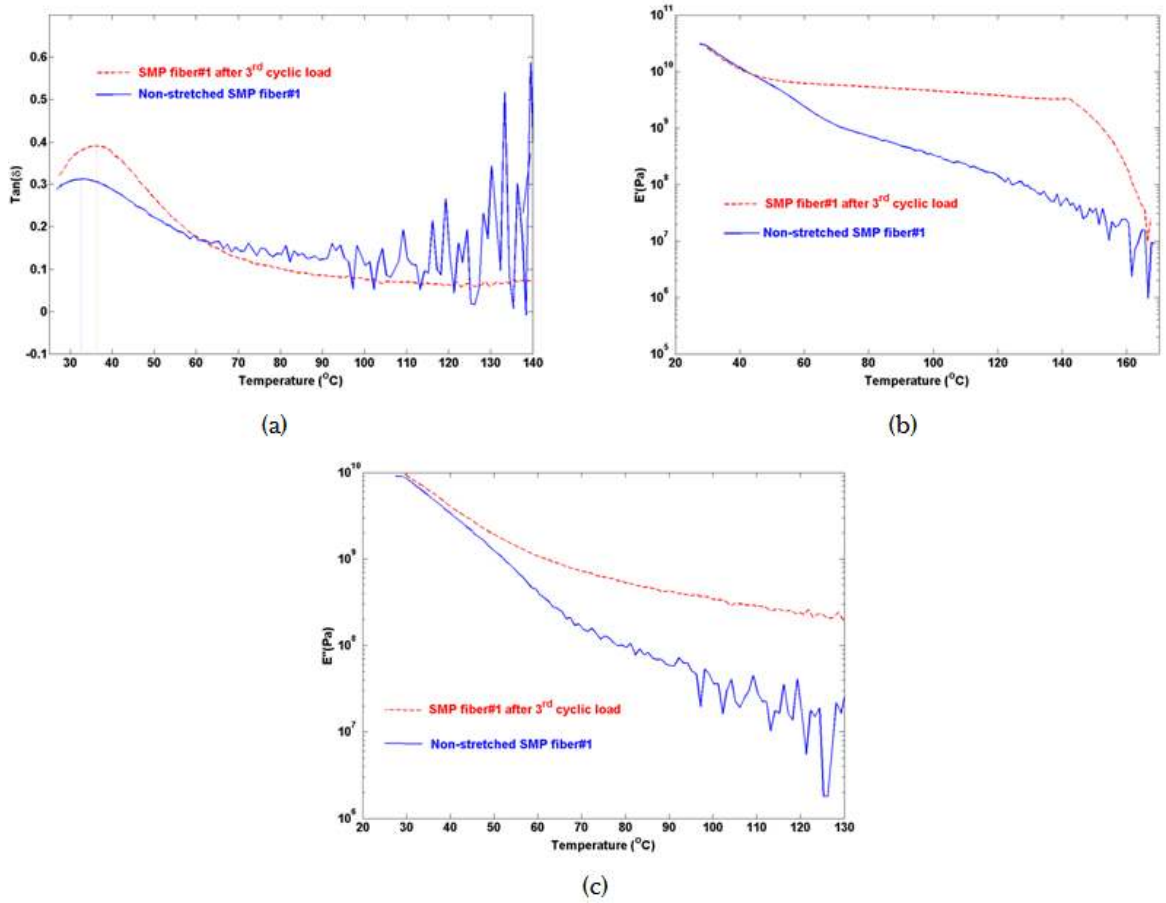

Figure 4-7 DMA test results (a) Phase angle Tan δ and (b) Storage modulus E′ (c) Loss modulus E"

4.4 Constitutive behaviors of semicrystalline shape memory polymer fibers

The proposed viscoplastic theory in this work considers the governing relations for each of the individual micro-constituents and establishes the microscale state of the stress and strain in each of the sub-phases. These microscale fields are then averaged through the micromechanics framework to demonstrate the macroscale constitutive mechanical behaviors. This multiscale approach incorporates more realistic material inputs as compared to the pure phenomenological models. Speaking in general the individual micro-constituents mechanical behaviors may vary when they are packed in a multiphase material system and a certain deviation in their mechanical responses may exist between the individual and their assembled configurations. In the following two well-established viscoplastic theories for the amorphous and crystalline polymers are presented. These theories are based on certain physical description of the viscoplastic deformation mechanisms in the glassy polymers.

4.4.1 Amorphous phase constitutive relation:

The well-established Boyce model for the inelastic deformation of the amorphous glassy polymers is assumed to be held for the amorphous phase of the semicrystalline SMP fiber.

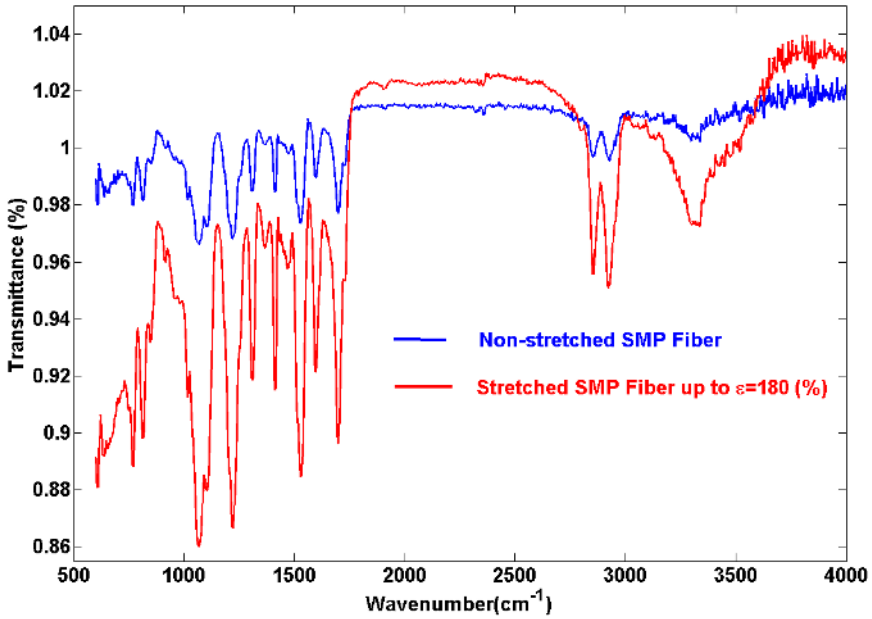

Figure 4-8 FTIR test results for the SMP fiber #2

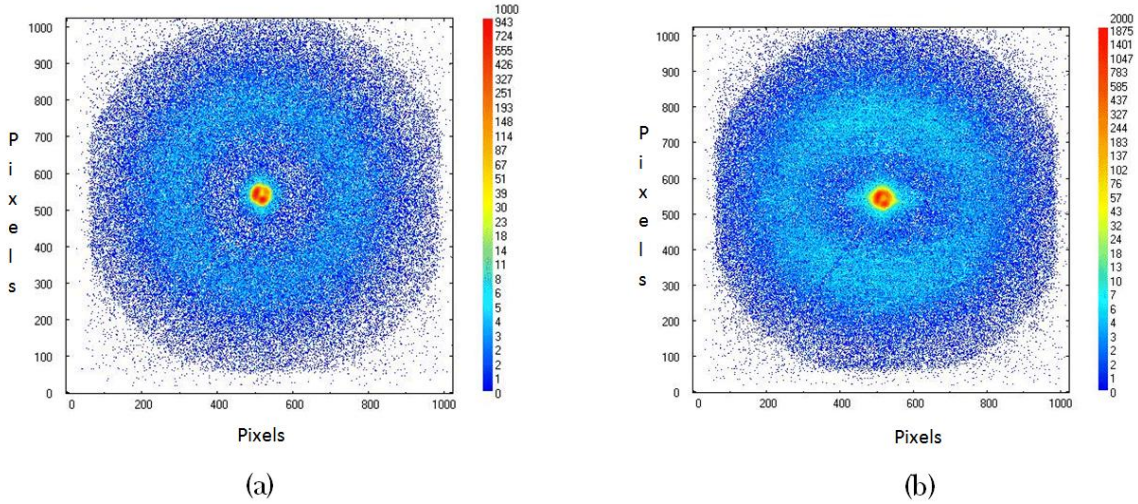

Figure 4-9 SAXS image for SMP fiber #1 (a) non-stretched fiber and (b) stretched fiber up to 350% of the strain level

The plastic multiplier in this model is introduced as follows (Boyce et al., 1989):

$$|\dot{\gamma}^p| = \dot{\gamma}_0^a \exp\left[-A\,\frac{s + a\,p}{\Theta}\left(1 - \left(\frac{|\tau|}{s + a\,p}\right)^{5/6}\right)\right] \qquad (4\text{-}1)$$

where a is a material parameter, p is pressure and s is the athermal shear strength. The material parameter A and the evolution law for s are defined as follows:

$$A = \frac{39\pi\omega^2\bar{a}^3}{16k}\,;\ \dot{s} = h\left(1 - \frac{s}{s_{ss}(\theta,|\dot{\gamma}^p|)}\right)|\dot{\gamma}^p|. \tag{4-2}$$

where ω and $\bar{a}$ are material parameters and k is the Boltzmann's constant (Argon, 1973). The material parameter h shows the rate the strain softening and s_{ss} represents the asymptotic preferred structure. The initial value of s for the annealed material is: $s_0 = \frac{0.077\mu}{1-\nu}$, where μ is the elastic shear modulus and ν is the Poisson's ratio.

The material constant $\dot{\gamma}_0^a$, in Eq. (4-1), is called amorphous pre-exponential inelastic strain rate, and $|\dot{\gamma}^p|$ is the effective equivalent inelastic deformation rate of a glassy polymer subjected to the effective equivalent shear stress, $|\tau|$, which is defined at the absolute temperature, Θ, as follows:

$$|\tau| = \sqrt{\frac{1}{2}s_{ij}^* s_{ij}^*} \tag{4-3}$$

where $s_{ij}^* = s_{ij} - X_{ij}$ in which $s_{ij} = \sigma_{ij} - \frac{1}{3}\sigma_{kk}\delta_{ij}$ is the deviatoric Cauchy stress and $X_{ij} = \alpha_{ij} - \frac{1}{3}\alpha_{mm}\delta_{ij}$ is the back stress tensor which is defined as follows [28-30]:

$$\alpha_{ij} = nk\Theta\frac{\lambda^L}{3}\left[\lambda_i^p\mathcal{L}^{-1}\left(\zeta\frac{\lambda_j^p}{\lambda^L}\right) - \frac{1}{3}\lambda_k^p\mathcal{L}^{-1}\left(\zeta\frac{\lambda_k^p}{\lambda^L}\right)\delta_{ij}\right] \textit{ no sum on } i \tag{4-4}$$

where n is the number of chains per unit volume, k is the Boltzmann's constant, and λ^L is the limit of chain extensibility and ζ is a viscoplastic related material constant which controls the magnitude of the hardening with respect to the inelastic stretches [23, 31]. In limit analysis Langevin function, $L(\beta) = \coth(\beta) - 1/\beta$, is used extensively and it imposes a limiting case in the evolution of the back stress tensor. Eq. (4-4) represents the magnitude of the amorphous inelastic strain rate; while the direction of the amorphous inelastic flow rate, $\dot{D}_{ij}^{ap}$, is governed by the deviatoric driving stress, s_{ij}^* . The following flow rule is then proposed for the inelastic deformation in the amorphous phase (Argon, 1973):

$$\dot{D}_{ij}^{ap} = |\dot{\gamma}^p|\frac{s_{ij}^*}{\sqrt{2}|\tau|} \tag{4-5}$$

4.4.2 Crystalline phase constitutive relation:

Inelastic deformation of the crystalline phase in semicrystalline polymers includes three different mechanisms: (a) crystallographic slip, (b) twining and (c) Martensite transformations (Stevenson, 1995). In this work the slippage mechanism is assumed to be the dominant influencing mechanism. A reference vector, c_i, is aligned with the crystallographic texture to show its evolution with deformation while two active slip mechanisms in the polymeric slippage system have been taken into account which are: (a) *chain slip*: the burgers vector is aligned with c_i and (b) *transverse slip*: the burgers vector is perpendicular to c_i [23, 31]. There are only four linearly independent crystalline slip systems, which are indicated by the unit vectors in the direction of the slip and normal to the slip planes including: (i) chain slip: (100)[001] and (010)[001], and (ii) transverse slip: (100)[010] and (010)[100] (Lee et al., 1993[23]). Vector $s_i^{(\alpha)}$ denotes the slip direction and $n_i^{(\alpha)}$ represents the unit normal vector to the slip plane, where $\alpha = 1$ to 4 is the number of the slip systems. The inelastic crystalline stretch rate tensor, $\dot{D}_{ij}^{cp}$, is introduced by the following relation (Lee et al., 1993):

$$\dot{D}_{ij}^{cp} = \sum_{\alpha=1}^{K} \dot{\gamma}^{(\alpha)} R_{ij}^{(\alpha)}, \tag{4-6}$$

where $R_{ij}^{(\alpha)}$ is the symmetric part of the Schmid tensor as defined by: $R_{ij}^{(\alpha)} = \frac{1}{2}\left\{s_i^{(\alpha)} n_j^{(\alpha)} + n_i^{(\alpha)} s_j^{(\alpha)}\right\}$, and it represents the α^{th} crystalline slip plane and the shear rate, $\dot{\gamma}^{(\alpha)}$, is defined as follows (Asaro, 1979; Asaro and Needleman, 1985; Hutchinson, 1976; Lee et al., 1993):

$$\dot{\gamma}^{(\alpha)} = \dot{\gamma}_0^c \frac{\tau^{(\alpha)}}{g^{(\alpha)}} \left|\frac{\tau^{(\alpha)}}{g^{(\alpha)}}\right|^{n^c - 1}, \tag{4-7}$$

where $\dot{\gamma}_0^c$ is the crystalline reference inelastic strain rate and $g^{(\alpha)}$ is the shear strength for the α^{th} slip system, and n^c is the rate sensitivity factor. The effective shear stress, $\tau^{(\alpha)}$, at the α^{th} slippage system, is given by [23]:

$$\tau^{(\alpha)} = S_{ij}^{c*} R_{ij}^{(\alpha)}, \tag{4-8}$$

where S_{ij}^{c*} is the projected deviatoric Cauchy stress, $s_{ij} = \sigma_{ij} - \frac{1}{3}\sigma_{kk}\delta_{ij}$, at the direction of the deviatoric part of the dyadic $c_i c_j$, i.e. $C_{ij}^{'} = c_i c_j - \frac{1}{3} I_{ij}$. This constraint is enforced based on the inextensibility of the crystalline chain together with the incompressibility assumption [31]. The lattice spin which controls the rate of changes of the direction of c_i is introduced as follows (Asaro and Rice, 1977; Lee et al., 1993):

$$\dot{W}_{ij}^{*} = \dot{W}_{ij}^{cp} - \sum_{\alpha=1}^{K} \dot{\gamma}^{(\alpha)} A_{ij}^{(\alpha)}, \tag{4-9}$$

where $A_{ij}^{(\alpha)} = \frac{1}{2}\left\{s_i^{(\alpha)} n_j^{(\alpha)} - n_i^{(\alpha)} s_j^{(\alpha)}\right\}$ is the skew part of the Schmid tensor and $\dot{W}_{ij}^{cp}$ is the skew part of the velocity gradient L_{ij}^{cp} in which $L_{ij}^{cp} = \dot{D}_{ij}^{cp} + \dot{W}_{ij}^{cp}$.

4.4.3 Cyclic texture update:

It is experimentally confirmed that the amorphous and crystalline polymers undergo the morphological texture changes in their polymeric networks upon stretching [28, 30, 32]. Then the strain hardening phenomenon in the SMP fiber is influenced by the textures changes in the crystalline and amorphous phases. In the following the governing relations for texture updates in each of these sub-phases are brought forward.

(i) Crystalline phase texture update:

The crystallographic texture is updated based on the applied lattice spins as discussed in Eq. (4-9) and it is expressed in the following form [33]:

$$\dot{c}_i = W_{ij}^{*} c_j, \tag{4-10}$$

where

$$c_i(t + \Delta t) = \exp\left(W_{ij}^{*} \Delta t\right) c_j(t), \tag{4-11}$$

Based on the Cayley-Hamilton expression for exponential term, one may find [23, 31]:

$$\exp\left(W_{ij}^{*} \Delta t\right) = I_{ij} + \frac{\sin w}{w} W_{ij}^{*} \Delta t + \left(\frac{1 - cosw}{w^2}\right) W_{ik}^{*} W_{kj}^{*} \Delta t^2 \tag{4-12}$$

with $w^2 = -tr\left(W_{ik}^{*} W_{kj}^{*} \Delta t^2\right)/2$.

(ii) Amorphous phase texture update:

In the case of amorphous phase one may only take into account the influence of the inelastic deformation on molecular chain rotations and the subsequent strain hardening effects. Boyce et al. relates the initial values of the back stress tensor, α_{ij}, athermal shear resistance, s, network stretch vector, Λ_i, and residual stress tensor, σ_{ij}, to the strain hardening effect in the amorphous phase and it is

shown that setting these parameters can effectively monitor the hardening phenomenon in the amorphous phase [34].

4.4.4 Recoverable stresses:

One of the vital parameters in designing the bio-inspired Close-Then-Heal healing systems is the available amount of the crack closure force which is necessary to close the macroscale cracks. As shown in Fig. 4-6, the SMP fibers show considerable recovery stresses which are in general dependent on the amount of the induced strain hardening during the cold-drawing process. Basically upon the cold-drawing process, the crystalline phase of the semicrystalline polyurethane SMP fibers undergoes the stress induced crystallization process, and it stores the applied deformations through the entropy changes in the crystalline network. Once the temperature exceeds the glass transition temperature of the semicrystalline polymer, the viscosity of the polymeric network drops and the frozen crystalline network is allowed to release the stored energy and achieve its minimum energy level. In other words upon heating, the stored energy in the crystalline phase is released and the polymeric network returns to its minimum level of internal energy. As shown in Fig. 4-6 after a few cold-drawing cycles the amount of the recoverable stresses is considerably aggrandized. Then one may relate the amount of the recoverable stresses to the loading history and stress induced crystallization process. In this study, the recoverable stress is assumed to be a function of the stress induced crystallization process and with the accumulated inelastic strains in the amorphous phase. Basically a portion of these induced inelastic entropic and energetic changes in the SMP molecular network is recoverable upon heating where the viscosity of the frozen network drops and the recoverable inelastic strains are restored. Then the proposed evolution law for the stress recovery takes into account the history of the loading, including the inelastic strains in the sub-phases. The kinematic and isotropic hardening relations in the classical continuum plasticity context provide a suitable governing equation form to explain the stress recovery process [35-37]. The stress recovery evolution relation is then proposed as follows:

$$\sigma^{rec} = R\big(1 - \exp\big(-\eta(T - T_{room})\big)\big) \tag{4-13}$$

where η is a material constant that controls the rate of saturation of the recovery stress to its final value which is R, and T and T_{room} are respectively elevated and room temperatures. Parameter R takes into account the history of the loading which includes the inelastic deformation, texture updates and residual stresses due to the cyclic hardening and this parameter is defined in the following. Taking time derivative of Eq. (4-13) results in the following incremental relation for the stress recovery computations:

$$\dot{\sigma}^{rec} = \dot{T} R\eta \, exp\big(-\eta(T - T_{room})\big) \tag{4-14}$$

where $\dot{T}$ shows the rate of the heating process. As shown in Fig. 4-4(b) the maximum stress recovery is achieved after reaching T_g and the rate of heating controls this peak time. The heating process is

controlled by time integration of the heating rate as: $T = \int \dot{T} dt + T_{room}$, and during the simulation once the temperature reaches its final value the heating rate is set to zero. The saturation limit, R, for the stress recovery is related to the loading history and the amount of the plastic strain by the following expression:

$$\dot{R} = \omega(\aleph - R)|\dot{\epsilon}^p| \tag{4-15}$$

where ω and $\aleph$ are two material parameters for controlling the saturation parameter, R, and $|\dot{\epsilon}^p| = \sqrt{\frac{2}{3}\dot{\epsilon}_{ij}^{p\,(c)}\dot{\epsilon}_{ij}^{p\,(c)}}$ is the equivalent plastic strain rate. Then during each of the cyclic loadings the magnitude of R is updated incrementally and its final value is introduced in Eq. (4-13) for the stress recovery computation. Eq. (4-15) represents a monotonically increasing value for the parameter R up to a certain saturation limit which is enforced by $\aleph$. The underlying physical background for Eqs. (13) and (15) is that the recoverable stress in a SMP fiber is a function of the recoverable microstructural changes during the cold drawing process and this stress recovery should saturates to a certain limit due to the limit in reversibility in these microstructural changes. In other words certain amounts of the microstructural changes are reversible in an SMP fiber and after certain limit these microstructural changes may results in failure of the polymeric networks and produce non-reversible defects. In this study, it is assumed that the recovery stress saturates to a certain limit as a function of the microstructural changes through Eqs. (13) and (15) and the physical parameter to control these changes is the accumulated inelastic strain and its rate.

4.4.5 Stress induced crystallization

The stress induced crystallization is a phenomenon which is experimentally investigated by many researchers [25, 38]. Here a phenomenological constitutive relation for the stress induced crystallization process is introduced. Fig. 4-10(a) shows the Representative Volume Element of the microstructure of the manufactured SMP fiber where a thin layer of initially formed crystalline phase is parallelized with the amorphous phase. Fig. 4-10(b) shows the enlarged cross section of the crystalline phase due to the applied stretches. Then one may assume that the microstructural changes are governed by the crystalline phase formation upon stretching. In order to take into account this fact into the governing relations of the semicrystalline polymers one may propose the following relations which related the initial inner, $\bar{r}_0^{ic}$, and outer, $\bar{r}_0^{oc}$, radii and the final inner, $\bar{r}_f^{ic}$, and outer, $\bar{r}_f^{oc}$, radii of the crystalline phase to the magnitude of the inelastic strains as follows:

$$\begin{aligned} r^{oc} &= \left(\bar{r}_f^{oc} - \bar{r}_0^{oc}\right)(1 - \exp(-q\,|\epsilon^p|)) + \bar{r}_0^{oc}, \\ r^{ic} &= \left(\bar{r}_0^{ic}\right)(\exp(-q'\,|\epsilon^p|)) + \bar{r}_f^{ic}. \end{aligned} \tag{4-16}$$

where $q$and $q^{'}$ are material parameters and $|\epsilon^p| = \sqrt{\frac{2}{3}\epsilon_{ij}^p \epsilon_{ij}^p}$ is the effective accumulated plastic strains and the outer, r^{oc}, and inner, r^{ic}, crystalline radii start from their initial values and they converge to their final values. Eq. (4-16) provides a smooth transition between highly amorphous to a highly crystalline microstructure while the history of loading is incorporated by formulating this process based on the inelastic strains. Then crystalline inner and outer radii change rates are given by the time derivation of Eq. (4-16) as follows:

$$\dot{r}^{oc} = q\,|\dot{\epsilon}^p|\left(\bar{r}_f^{oc} - \bar{r}_0^{oc}\right) exp(-q\,|\epsilon^p|),$$
$$\dot{r}^{ic} = -q^{'}\,|\dot{\epsilon}^p|\left(\bar{r}_0^{ic}\right)(\exp(-q^{'}\,|\epsilon^p|)). \tag{4-17}$$

The volume fraction of the crystalline, c^{cry}, and amorphous phases are then given by the following relations:

$$c^{cry} = \frac{(r^{oc} - E_z \nu_{12}^c r^{oc})^2 - \left(r^{ic} - E_z \nu_{12}^c r^{ic}\right)^2}{\left(r_0^a - E_z \nu_{12}^a r_0^a\right)^2}, \text{ and } c^{amr} = 1 - c^{cry}. \tag{4-18}$$

where E_z is the macroscopic strain at the fiber direction and ν_{12}^c and ν_{12}^a are respectively the crystalline and amorphous phases Poison's ratio. The fiber is assumed to be transversely isotropic, i.e. $\nu_{12}^{\#} = \nu_{13}^{\#}$.

4.4.6 Micromechanics:

It is experimentally confirmed in section 2 that the crystalline phase of the semicrystalline polyurethane in a SMP fiber is aligned with the loading direction after a few rounds of cyclic hardening. Due to the fact that the manufactured fibers are assumed to be transversely isotropic, one may assume that the amorphous and crystalline phases in the SMP fibers are assembled in a parallel configuration. While other micromechanics configurations, such as series or rule of mixture, are easily applicable without affecting the theory, the parallel configuration simplifies the numerical simulations significantly. Then the states of the stress and strain are given by the following basic micromechanics relations:

$$E_z = \epsilon_z^a = \epsilon_z^c,$$
$$\Sigma_z = \sigma_z^a + \sigma_z^c. \tag{4-19}$$

where E_z and Σ_z are respectively the longitudinal macroscopic strain and stress and ϵ_z^a and ϵ_z^c are the microscale strain fields in the amorphous and crystalline phases, respectively; and σ_z^a and σ_z^c are respectively the local stresses in the amorphous and crystalline phases. One may assume that the loading condition is strain controlled, then the strain in all phases are equal to the macroscale applied strain while the local stresses are computed from the respective microscale constitutive relations.

The representative volume element is chosen based on the experimental observations of the microstructure of the SMP fibers. As shown in section 2 the non-stretched fiber is initially non-oriented and upon cold drawing the microstructure of the SMP fiber varies. In this work an asymmetric mechanical properties is assumed for both of the stretched and non-stretched fibers while the microstructural changes are assumed to be stress induced crystallization and morphological texture changes upon loading. Fig. 4-10(a) shows the status of the microstructure for the manufactured SMP fiber. Upon loading the stress induced crystallization process results in larger volume fraction of the oriented crystalline phase as shown in Fig. 4-10(b). The morphological texture updates for the amorphous and crystalline phases however are implicitly accounted in their respective governing constitutive relations. In this way the simulations can monitor two significant microstructural changes which are texture updates in the amorphous and crystalline phases and the stress induced crystallization process. The SAXS picture for the cold drawn SMP fiber #1 is shown in Fig. 4-9 (b) which confirms the oriented microstructure after a few cycles of the cold drawing process.

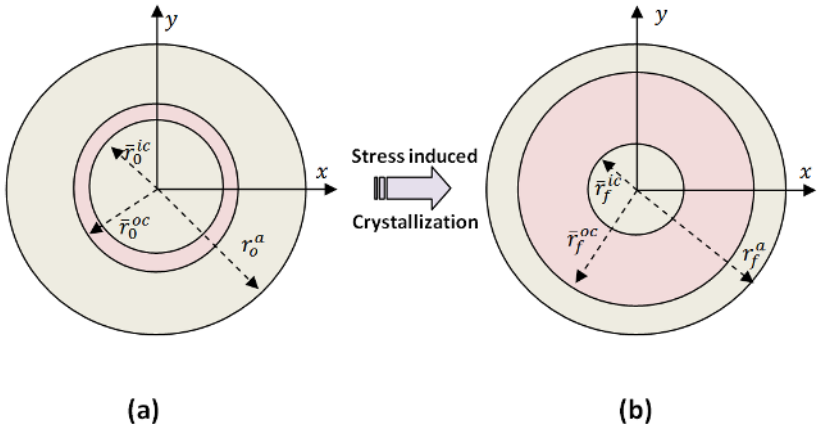

Figure 4-10 Microstructural representation for the SMP fiber (a) primary microstructure of the SMP fiber which contains some crystalline phase, (b) cold drawn SMP fiber results in stress induced crystalline phase.

4.5 Kinematic and Computational Aspect of Finite Stain

In the case of the finite deformation the strain description based on the displacement gradients become non-linear which may results in some computational difficulties for elasto-plastic analysis. To avoid such phenomenon the gradients of the elastic and plastic deformations are decomposed multiplicatively. This is called *multiplicative decomposition* proposed previously by Lee [39, 40]:

$$F_{ij} = F_{ik}^{e} F_{kj}^{p} \tag{4-20}$$

where F_{ij} is the total deformation gradient which correlates the material and deformed configurations, F_{ij}^{e} is the elastic deformation gradient and it is obtained by elastically unloading the deformed configuration to stress free status; this unloaded state is called *intermediate configuration,* and F_{ij}^{p} is the plastic deformation gradient. Additive decomposition of the Lagrangian strain tensor, d_{ij}, which is measured in the material configuration, was proposed by Green and Naghdi [41, 42] as follows:

$$d_{ij} = d_{ij}^{e} + d_{ij}^{p} \tag{4-21}$$

where d_{ij}^{e} and d_{ij}^{p} are Lagrangian elastic and plastic strain tensors, respectively. This additive assumption which follows the basic thermodynamic principals [43] of solids provides the basis for the *elastic predictor-plastic corrector* elasto-plastic solutions as discussed by Simo et al. [44-46]. The resulting return mapping algorithms are the direct consequence of the additive decomposition, Eq. (4-21). Let the second order displacement tensor, u_{ij}, describe an incremental deformation field and its second order gradient tensor, ∇u_{ij}, shows the deformation rate. The outline for the return mapping algorithm is as follows: *(i)* an increment of the deformation gradient is introduced as, $F_{ij}^{(n+1)} = (I_{ik} + \nabla u_{ik})F_{kj}^{(n)}$ where I_{ij} is the unity second rank tensor and the superscripts n and $n+1$ indicate respectively the previous and current load steps, *(ii)* a "Trial-Elastic" deformation gradient is introduced subsequently to elastically stretching the material configuration with $F_{ij}^{e\,(n+1)^{Trial}} = F_{ik}^{(n+1)}F_{kj}^{p\,(n)^{-1}}$ where superscripts "e" and "p" denote to the "elastic" and "plastic" components, respectively; and $F_{ij}^{p\,(n)}$ shows the frozen inelastic deformation gradient, *(iii)* the elastically stretched configuration is then relaxed until the state of the stress returns to the yield surface. The return mapping relaxes the stresses along the steepest descent path which is defined based on the yield function (associated flow rules) or potential functions (non-associated flow rules) [37]. In this work an isochoric condition is assumed for the large deformation process which is stated by $\lambda_1\lambda_2\lambda_3 = 1$, where λ_i denotes the principal stretches. Then the volume preserving part of the deformation gradient, F_{ij}, the elastic deformation gradient, F_{ij}^{e}, right, $C_{ij} = F_{ik}^{T}F_{kj}$, and left, $b_{ij} = F_{ik}^{T}F_{kj}$, Cauchy-Green tensors are given as follows [23, 44]:

$$\hat{F}_{ij} = J^{-\frac{1}{3}}F_{ij},\ \hat{F}_{ij}^{e} = J^{-1/3}F_{ij}^{e},\ \hat{C}_{ij} = J^{-\frac{2}{3}}C_{ij};\ \hat{b}_{ij} = J^{-\frac{2}{3}}b_{ij}. \tag{4-22}$$

where $\widehat{\ }$ shows the volume preserving components for its respective tensor parameter and $J = \det(F_{ij})$. This kinematic decomposition approach results in the isochoric inelastic deformation in which $det(F_{ij}^{p}) \equiv 1$. The isochoric assumption should be extended for all three steps of the return mapping algorithm as discussed by Shojaei and Li [23]. To declare the stress-strain relation in the finite deformation process, the proper stress definition should be chosen. Accordingly, the Cauchy stress

tensor, σ_{ij}, is assigned to the deformed body and it is defined as force per unit deformed area. To obtain a more convenient description of the stress the *first Piola-Kirchhoff* (PK) stress, τ_{ij}^{p}, is computed which is the force per unit undeformed area that is still allocated in the deformed configuration. If the first Piola-Kirchhoff stress is pulled-back to the material configuration then the second PK stress tensor, S_{ij}^{p}, is achieved [23, 44]. Anand [47] proposed a relation between the Cauchy stress and the Hencky strain as follows:

$$\sigma_{ij} = \frac{1}{J} L_{ijkl}^{e} \ln(U_{kl}^{e}) \tag{4-23}$$

where $U_{ij}^{e} = \sqrt{\hat{C}_{ij}^{e}}$ and L_{ijkl}^{e} is the fourth order elastic stiffness tensor. The multiscale analysis in this work requires different computational modules to compute the microscale state of the stress and strain in each of the sub-phases with respect to their constitutive relations and then these microscale mechanical fields are correlated to their macroscale fields through the micromechanics framework. The configuration of such a multiscale computational module is depicted in Fig. 4-11, where the general outlines for a micromechanics-based multiscale analysis are shown.

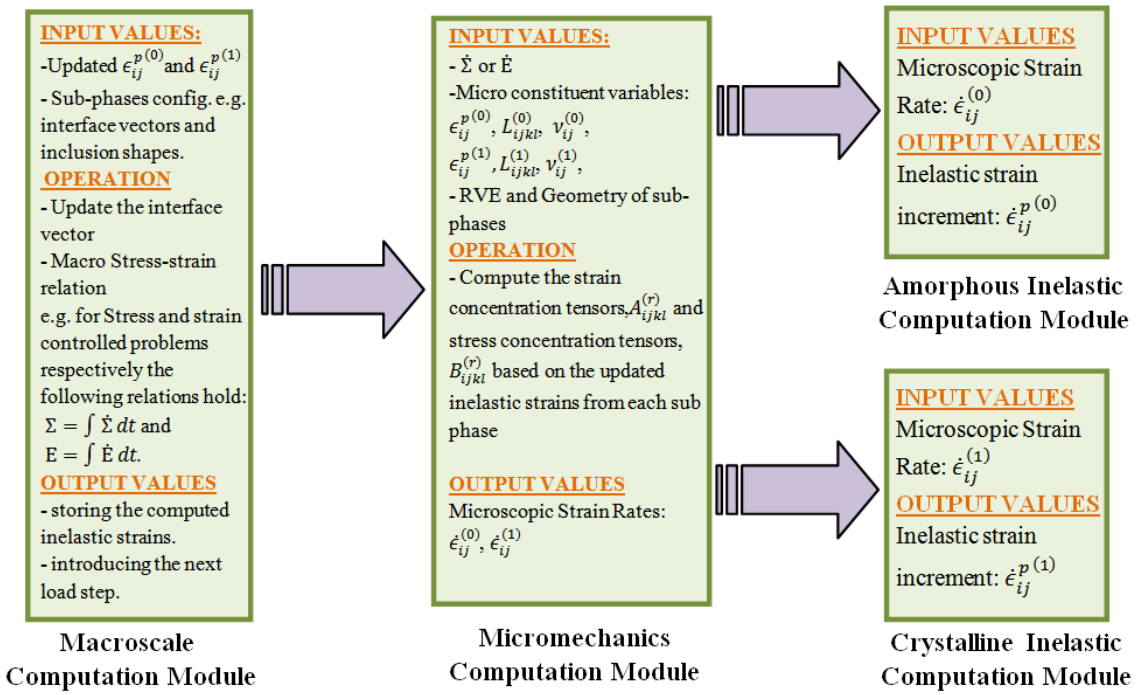

Figure 4-11 Computation algorithm for a micromechanics based multiscale analysis [23]

4.6 Results and Discussion

The stress recovery test result is demonstrated in Fig. 4-12. The evolution of the parameter R controls the saturation limit of the recoverable stress based on the loading history and basically this parameter identifies the amount of the recoverable stress based on the cyclic strain hardening and accumulated inelastic strains. Then the established stress recovery results in Fig. 4-12 takes into account the heating rate, initial and final temperatures and history of the loading. As it is obvious from this figure the slower heating rates are associated with longer response time for the SMP fiber to reach its maximum stress recovery response. Table 4-2 denotes the necessary material constants for the stress recovery and the stress induced crystallization simulations.

Table 4-2 Material parameters for the stress recovery and cyclic hardening simulations

η	T_{room} (°C)	T_{final} (°C)	ω	$\aleph$ (MPa)	q	q'	$\bar{r}_f^{oc}$	$\bar{r}_0^{oc}$	$\bar{r}_0^{ic}$
0.0294	25	90	1	200	0.2	0.1	0.65	0.5	0.2

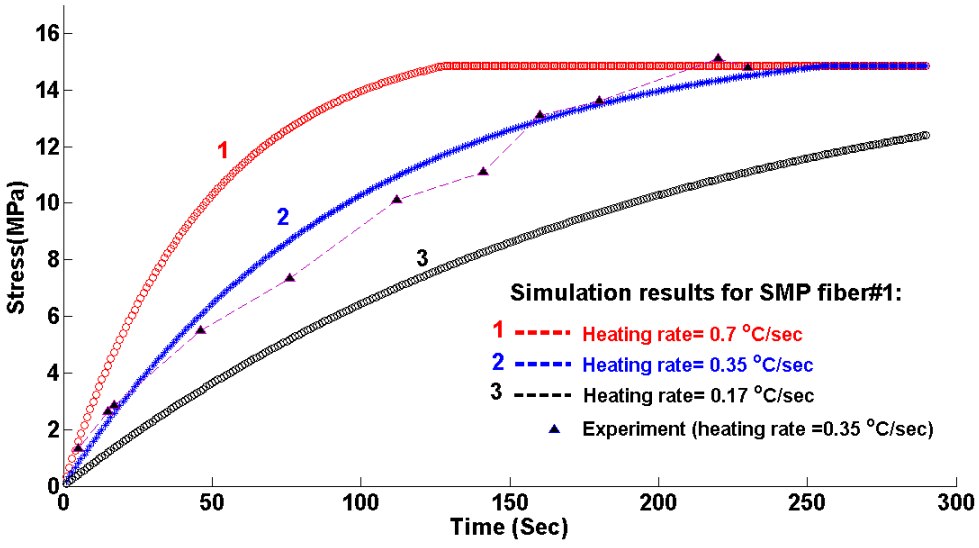

Figure 4-12 Simulation and experimental results for stress recovery of SMP fiber#1 based on different heating rates

Due to the fact that the proposed multiscale viscoplastic analysis incorporates the individual constitutive equations for each of the sub-phases, it can easily capture a vast variety of the microstructural

configurations, such as 100 wt% amorphous or crystalline fibers or any microstructure configuration which lies between these two extreme cases. In Fig. 4-13, three cyclic tension test results for the single SMP fiber #1 together with the simulation results are depicted. The simulation for the 10 wt% crystalline phase volume fraction shows perfect correlation with the experimental results. In the second and third cyclic tensions, the SMP fiber is work hardened and shows stiffer mechanical responses. The proposed theory can capture the second cycle while in the third cycle it shows some deviation from the experiments. The changes in mechanical responses of the SMP fiber may relies on the fact that the fiber undergo large deformation and more accurate strain measurements are required to take into account the transverse deformation effects which narrows the fibers in high strain levels. The theory may then still hold its genuinely for larger cycles if the higher order accuracy stress-strain measurements, such as image processing measurement techniques [48], are utilized.

In reality the fiber structure is a non-homogenous state of material and this fact should be incorporated during assembling the stiff matrix for these fibers. Here it is assumed that the fiber is transversely isotropic and the primarily non-hardened elastic properties are assumed for the transverse direction while the properties along the fiber direction are updated based on the strain hardening process. These transient changes in the elastic stiffness at the fiber direction are clearly depicted in Fig. 4-13, where the elastic modulus varies gradually from a pure amorphous to a crystalline dominant phase. Once the related material parameters for the amorphous and the crystalline phases are established the volume fraction of the crystalline phase, which is controlled by the stress induced crystallization governing equations, is introduced to the computational module and the resultant macroscale mechanical responses are captured subsequently. Table 4-3 shows the amorphous and crystalline related material parameters. The crystalline slippage system for the polymeric network is given in Table 4-4.

Table 4-3 Material parameters for crystalline and amorphous computational modules

Amorphous Computational Module (Soft Segment)									
nkT (MPa)	$\dot{\gamma}_0$ (sec^{-1})	A	ζ	λ_L	k	T (K)	σ_y (MPa)	E_z (MPa)	E_t (MPa)
0.5	0.03	3.31e-27	0.1	0.1	1.38e-23	298	20	100	70
Crystalline Computational Module (Hard Segment)									
n	$\dot{\gamma}_0$ (sec^{-1})	Reference Cry. Axes			Slippage Systems		σ_y (MPa)	E_z (MPa)	E_t (MPa)
5	0.05	(0.5,0.5,0.5)			See Table (4-3)		100	70	70

Table 4-4 Hypothetical crystalline slippage systems [23]

Slippage Type	Indicial Notation	Normalized resistance (g^{α}/τ_0)
Chain Slip	(100)[001]	1
	(010)[001]	2.5
	{110}[001]	2.5
Transverse Slip	(100)[010]	1.6
	(010)[100]	2.5
	{110}<1$\bar{1}$0>	2.5

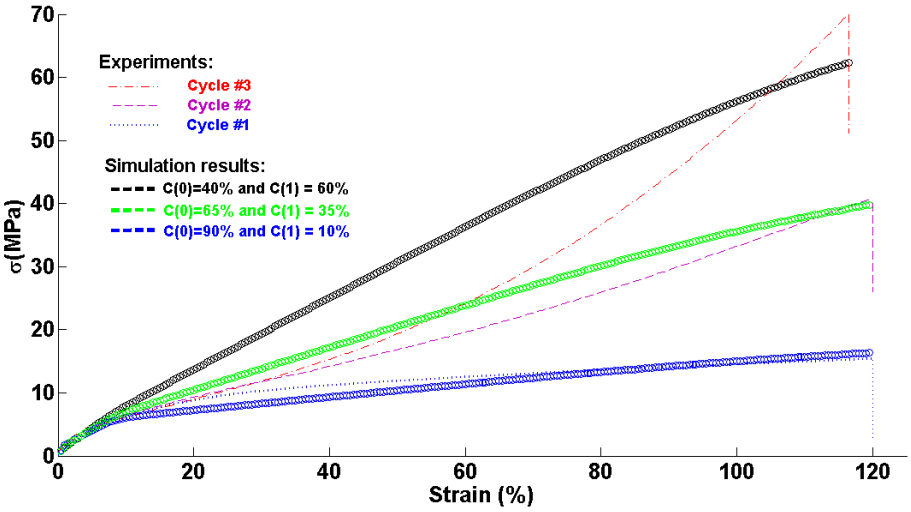

Figure 4-13 Simulation results for various volume fractions of the crystalline and amorphous phases together with cyclic tension test results for the SMP fiber #1 up to 120% strain level with 50.8 mm/min strain rate

The stress induced crystallization process is simulated in Fig. 4-14 based on the proposed governing relations. The crystallization microstructural change is assumed to follow the SAXS picture in which the crystalline microstructure is embraced with the amorphous phase. The inner and outer radii of this crystalline annulus are expanded and shrank respectively during the cold drawing process to show the

stress induced crystallization microstructural changes. Then upon loading the volume fraction of the oriented crystalline phase is gradually increased and the fiber becomes stiffer.

4.7 Concluding remarks

A bio-inspired healing scheme is proposed in this study through architectural design of a composite structure, which is constructed by SMP fiber z-pinned, continuous SMP fiber grid reinforced thermoset polymer embedded with thermoplastic particles. The scheme is demonstrated through experimental testing and finite element modeling. It is found that the polyurethane thermoplastic fibers, upon strain hardening by cold-drawing programming, can achieve the required recovery stress to close macroscopic cracks. Further, the microstructure changes due to the cold-drawing programming are characterized by instrumented microstructural analysis, which provides fundamental understanding and parameters for the constitutive modeling.

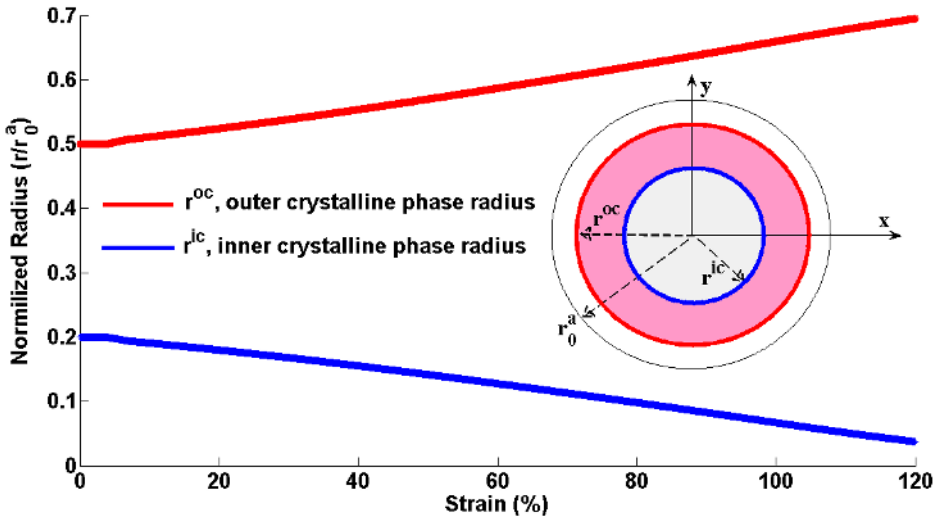

Figure 4-14 Simulation of the stress induced crystallization process in which internal and outer radii of the crystalline phase evolves with loading process

Due to the fact that the polyurethane SMP fibers are categorized in the class of the semicrystalline polymers, the enhanced mechanical responses of the cold drawn fibers are correlated to the stress induced crystallization process and the morphological texture changes in the amorphous and crystalline phases in this work. A micromechanical multiscale viscoplastic theory is developed to link the microscale mechanical responses of the amorphous and crystalline sub-phases to the macroscale mechanical behaviors of the SMP fibers including the cyclic hardening, and stress recovery responses.

The proposed theory takes into account the stress induced crystallization process and the initial morphological texture while the polymeric texture is updated based on the applied stresses. The cyclic loading and the thermomechanical responses of the SMP fibers are experimentally investigated in which the proposed theory is utilized to capture these phenomena. The proposed viscoplastic theory together with the material characterizations of the SMP fibers assist designers to predict the final strength, stress recovery and life of the self-healing structures made from the semicrystalline SMP fibers. This study may open new opportunities for the application of SMP fibers in load-bearing and healing composite structures.

4.8 References

[1] Voyiadjis, G.Z., A. Shojaei, and G. Li, A thermodynamic consistent damage and healing model for self healing materials. International Journal of Plasticity, 2011a. **27**(7): p. 1025-1044.

[2] White, S. R. , Sottos, N. R. , Geubelle, P. H. , Moore, J. S. , Kessler, M. R. , Sriram, S. R. , Brown, E. N. and Viswanathan, S. ,Autonomic healing of polymer composites. Nature, 2001. **409**(6822): p. 794-797.

[3] Pang, J.W.C. and I.P. Bond, A hollow fibre reinforced polymer composite encompassing self-healing and enhanced damage visibility. Composites Science and Technology, 2005. **65**(11-12): p. 1791-1799.

[4] Toohey, K.S., Sottos, N.R., Lewis, J.A., Moore, J.S. and White, S.R., Self-healing materials with microvascular networks. Nat Mater, 2007. **6**(8): p. 581-585.

[5] Zako, M. and N. Takano, Intelligent Material Systems Using Epoxy Particles to Repair Microcracks and Delamination Damage in GFRP. Journal of Intelligent Material Systems and Structures, 1999. **10**(10): p. 836-841.

[6] Voyiadjis, G. Z., Shojaei, A, Li, G. and Kattan, P.I., A Theory of Anisotropic Healing and Damage Mechanics of Materials. Proceeding of The Royial Society A, 2012, **468**(2137): 163-183.

[7] Varley, R.J. and S. van der Zwaag, Towards an understanding of thermally activated self-healing of an ionomer system during ballistic penetration. Acta Materialia, 2008. **56**(19): p. 5737-5750.

[8] Plaisted, T.A. and S. Nemat-Nasser, Quantitative evaluation of fracture, healing and re-healing of a reversibly cross-linked polymer. Acta Materialia, 2007. **55**(17): p. 5684-5696.

[9] Liu, Y.L. and Y.W. Chen, Thermally reversible cross-linked polyamides with high toughness and self-repairing ability from maleimide and furan-functionalized aromatic polyamides. Macromol. Chem. Phys., 2007. **208**(2): p. 224.

[10] Kirkby, E. L., Michaud, V. J., Månson, J. A. E., Sottos, N. R. and White, S. R., Performance of self-healing epoxy with microencapsulated healing agent and shape memory alloy wires. Polymer, 2009. **50**(23): p. 5533-5538.

[11] Li, G. and N. Uppu, Shape memory polymer based self-healing syntactic foam: 3-D confined thermomechanical characterization. Composites Science and Technology, 2010. **70**(9): p. 1419-1427.

[12] Nji, J. and G. Li, A biomimic shape memory polymer based self-healing particulate composite. Polymer, 2010a. **51**(25): p. 6021-6029.

[13] Xu, W. and G. Li, Constitutive modeling of shape memory polymer based self-healing syntactic foam. International Journal of Solids and Structures, 2010. **47**(9): p. 1306-1316.

[14] Li, G. and D. Nettles, Thermomechanical characterization of a shape memory polymer based self-repairing syntactic foam. Polymer, 2010. **51**(3): p. 755-762.

[15] John, M. and G. Li, Self-Healing of Sandwich Structures with Grid Stiffened Shape Memory Polymer Syntactic Foam Core. Smart Materials and Structures, 2010. **19**(7): p. 1-12.

[16] Nji, J. and G. Li, A self-healing 3D woven fabric reinforced shape memory polymer composite for impact mitigation. Smart Mater. Struct., 2010b. **19**(3): p. 1-9.

[17] Li, G. and M. John, A self-healing smart syntactic foam under multiple impacts. Composites Science and Technology, 2008. **68**(15-16): p. 3337-3343.

[18] Li, G. and W. Xu, Thermomechanical behavior of thermoset shape memory polymer programmed by cold-compression: Testing and constitutive modeling. Journal of the Mechanics and Physics of Solids, 2011. **59**(6): p. 1231-1250.

[19] Meng, Q.H. and J.L. Hu, The Influence of Heat Treatment on Properties of Shape Memory Fibers: I. Crystallinity, Hydrogen Bonding and Shape Memory Effect. Journal of Applied Polymer Science, 2008. **109**: p. 2616-2623.

[20] Ping, Peng, Wang, Wenshou, Chen, Xuesi and Jing, Xiabin, Poly(ε-caprolactone) Polyurethane and Its Shape-Memory Property†. Biomacromolecules, 2005. **6**(2): p. 587-592.

[21] Clough, S.B. and N.S. Schneider, Structural studies on urethane elastomers. Journal of Macromolecular Science, Part B, 1968. **2**(4): p. 553-566.

[22] Clough, S.B., N.S. Schneider, and A.O. King, Small-angle X-Ray scattering from polyurethane elastomers. Journal of Macromolecular Science, Part B, 1968. **2**(4): p. 641-648.

[23] Shojaei, A. and G. Li, A Multiscale Finite Strain Inelastic Theory for Semicrystalline Glassy Shape Memory Polymers. Journal of the Mechanics and Physics of Solids, (under review).

[24] Guo, J. and K.A. Narh, Simplified model of stress-induced crystallization kinetics of polymers. Advances in Polymer Technology, 2002. **21**(3): p. 214-222.

[25] Bowden, P.B. and R.J. Young, Deformation mechanisms in crystalline polymers. Journal of Materials Science, 1974. **9**(12): p. 2034-2051.

[26] Eshelby, J.D., The Determination of the Elastic Field of an Ellipsoidal Inclusion, and Related Problems. Proceedings of the Royal Society of London. Series A. Mathematical and Physical Sciences, 1957. **241**(1226): p. 376-396.

[27] Nemat-Nasser, S. and M. Hori, Micromechanics: Overall Properties of Heterogeneous Materials. 1993, Amsterdam: Elsevier

[28] Arruda, E.M. and M.C. Boyce, Evolution of plastic anisotropy in amorphous polymers during finite straining. International Journal of Plasticity, 1993. **9**(6): p. 697-720.

[29] Arruda, E.M. and M.C. Boyce, A three-dimensional constitutive model for the large stretch behavior of rubber elastic materials. Journal of the Mechanics and Physics of Solids, 1993. **41**(2): p. 389-412.

[30] Arruda, E.M., M.C. Boyce, and H. Quintus-Bosz, Effects of initial anisotropy on the finite strain deformation behavior of glassy polymers. International Journal of Plasticity, 1993. **9**(7): p. 783-811.

[31] Ahzi, S., D.M. Park, and A.S. Argon, Estimats of the overall elastic properties in semi-crystalline polymers. AMD- Vol. 203, Current Research in the Thermo-Mechanics of Polymers in the Rubbery-Glassy Range 1995: p. 31-44.

[32] Lee, B.J., S. Ahzi, and R.J. Asaro, On the plasticity of low symmetry crystals lacking five independent slip systems. Mechanics of Materials, 1995. **20**(1): p. 1-8.

[33] Asaro, R.J. and J.R. Rice, Strain localization in ductile single crystals. Journal of the Mechanics and Physics of Solids, 1977. **25**(5): p. 309-338.

[34] Dupaix, R.B. and M.C. Boyce, Constitutive modeling of the finite strain behavior of amorphous polymers in and above the glass transition. Mechanics of Materials, 2007. **39**(1): p. 39-52.

[35] Chaboche, J.L., On some modifications of kinematic hardening to improve the description of ratchetting effects. International Journal of Plasticity, 1991. **7**(7): p. 661-678.

[36] Shojaei, A., M. Eslami, and H. Mahbadi, Cyclic loading of beams based on the Chaboche model. International Journal of Mechanics and Materials in Design, 2010. **6**(3): p. 217-228.

[37] Voyiadjis, G.Z., A. Shojaei, and G. Li, A Generalized Coupled Viscoplastic- Viscodamage-Viscohealing Theory for Glassy Polymers. International Journal of Plasticity, 2012b. **28**(1): p. 21-45.

[38] Bowden, P.B. and S. Raha, The formation of micro shear bands in polystyrene and polymethylmethacrylate. Philosophical Magazine, 1970. **22**(177): p. 463 – 482.

[39] Lee, E.H. and D.T. Liu, Finite-Strain Elastic---Plastic Theory with Application to Plane-Wave Analysis. Journal of Applied Physics, 1967. **38**(1): p. 19-27.

[40] Lee, E.H., Closure to ``Discussion of `Elastic-Plastic Deformation at Finite Strains'" (1970, ASME J. Appl. Mech., 37, pp. 243--244). Journal of Applied Mechanics, 1970. **37**(1): p. 244-244.

[41] Green, A.E. and P.M. Naghdi, A general theory of an elastic-plastic continuum. Archive for Rational Mechanics and Analysis, 1965. **18**(4): p. 251-281.

[42] Green, A.E. and P.M. Naghdi, Some remarks on elastic-plastic deformation at finite strain. International Journal of Engineering Science, 1971. **9**(12): p. 1219-1229.

[43] NAGHDI, P.M. and J.A. TRAPP, RESTRICTIONS ON CONSTITUTIVE EQUATIONS OF FINITELY DEFORMED ELASTIC-PLASTIC MATERIALS. The Quarterly Journal of Mechanics and Applied Mathematics, 1975. **28**(1): p. 25-46.

[44] Simo, J.C. and M. Ortiz, A unified approach to finite deformation elastoplastic analysis based on the use of hyperelastic constitutive equations. Computer Methods in Applied Mechanics and Engineering, 1985. **49**(2): p. 221-245.

[45] Simo, J.C. and K.S. Pister, Remarks on rate constitutive equations for finite deformation problems: computational implications. Computer Methods in Applied Mechanics and Engineering, 1984. **46**(2): p. 201-215.

[46] Simo, J.C. and R.L. Taylor, A return mapping algorithm for plane stress elastoplasticity. International Journal for Numerical Methods in Engineering, 1986. **22**(3): p. 649-670.

[47] Anand, L., On H. Hencky's Approximate Strain-Energy Function for Moderate Deformations. Journal of Applied Mechanics, 1979. **46**(1): p. 78-82.

[48] G'Sell, C., J.M. Hiver, and A. Dahoun, Experimental characterization of deformation damage in solid polymers under tension, and its interrelation with necking. International Journal of Solids and Structures, 2002. **39**(13-14): p. 3857-3872.

CHAPTER 5 CYCLIC VISCOPLASTIC-VISCODAMAGEANALYSIS OF SHAPE MEMORY POLYMER FIBERS WITH APPLICATION TO SELF HEALING SMART MATERIALS*

5.1 Nomenclature

$\boldsymbol{A}^{(\alpha)}$ skwe-symmetry part of the Schmid tensor

$\boldsymbol{c}$ crystallographic axes vector

$\dot{\boldsymbol{d}}^{c}$ inelastic crystalline stretch rate tensor

$\boldsymbol{F}$ total deformation gradient tensor

$\boldsymbol{F}^{e}$ elastic deformation gradient tensor

$\boldsymbol{F}^{p}$ plastic deformation gradient tensor

$\boldsymbol{L}^{c}$ crystalline velocity gradient tenor

$\boldsymbol{\sigma}$ Cauchy stress tensor

$\boldsymbol{\epsilon}$ strain tensor

$\boldsymbol{\tau}^{p}$ first Piola-Kirchhoff tensor

$\tau^{(\alpha)}$ crystalline phase Cauchy shear stress, associated with the αth slippage system

$|\tau|$ amorphous phase shearing stress

μ shear modulus

ν Poisson's ratio

$\boldsymbol{\alpha}$ amorphous phase back stress tensor

$\boldsymbol{X}$ amorphous phase deviatoric back stress tensor

$\boldsymbol{S}^{p}$ second Piola-Kirchhoff tensor

$\boldsymbol{S}^{c}$ deviatoric Cauchy stress tensor

$\boldsymbol{S}^{c*}$ crystalline deviatoric Cauchy stress tensor, projected at the c_i direction

$\boldsymbol{S}^{cp}$ deviatoric Cauchy stress tensor, projected perpendicular to the c_i direction

* Submitted paper to ASME Journal of APPLIED MECHANICS for peer review

$\boldsymbol{s}^*$ driving stress tensor in the amorphous phase

s amorphous athermal shear strength

$\boldsymbol{R}$ rotation tenor

$\boldsymbol{U}$ stretch tensor

$\boldsymbol{R}^{(\alpha)}$ symmetric part of the Schmid tensor

$\dot{\gamma}^{(\alpha)}$ crystalline shearing strain rate associated with αth slippage system

$|\dot{\gamma}^p|$ amorphous shearing strain rate

$\boldsymbol{W}^c$ spin tensor

$\boldsymbol{W}^{c*}$ lattice spin tensor

5.2 Introduction

Shape Memory Polymers (SMPs) have shown their excellent functionality as mechanical actuators in different smart material systems, although their applications are restricted due to the low actuating force. SMP fibers provide enhanced functionality because molecules in fibers are aligned along the longitudinal direction. One of the most promising application fields of SMPs is polymeric self-healing material systems in which the SMP matrix is designed to close the opened cracks due to different category of damages, e.g. structural length scale damages such as impact damage or micron scale damages such as fatigue damage. In previous studies a full understanding of these material systems has been developed [1-6]. These systems utilize a bio-inspired healing mechanism which is called Close-Then-Heal [2, 3, 7] in which the cracks are closed through confined shape recovery upon applying external trigger and then they are healed, as proved by [8]. Once the crack is closed different healing mechanisms such as liquid healing agent [9-11], or solid healing agent such as molten thermoplastic particles [12] may be incorporated to obtain a molecular level healed configuration. Most recently, Li and Shojaei [13] proposed a new biomimetic self-healing system: cold-drawn SMP fiber grid skeleton reinforced conventional thermosetting polymer matrix. The ability to close macroscopic crack through localized heating has been demonstrated. Actually, instead of the SMP fiber grid skeleton, uniformly distributed short SMP fibers, after cold-drawn programming, may have the same capability to close structural-length scale crack in the thermosetting polymer matrix. As discussed by Li and Shojaei [13], the key advantage of this newly proposed approach is (1) it closes macroscopic crack with a small amount of SMP material; (2) the SMP fibers can function repeatedly because each constrained recovery leads to a new round of tension programming [3]. Fig. 5-1 presents a schematic view of the proposed self-healing scheme with distributed short SMP fibers, where short SMP fibers are shown with rods and Thermoplastic Particles (TPs) are shown as particles. The color changes show the temperature changes.

Fig. 5-1(a) illustrates a Representative Volume Element (RVE) of the material system with a macroscale crack. Fig. 5-1(b) shows the crack is closed due to the stress recovery process of these cold-drawn programmed fibers upon the heating process. In Fig. 5-1(c) the TPs are molten due to further heating and they diffuse into the crack matrix. In Fig. 5-1(d) the room temperature configuration is shown in which the molten TPs solidifies and provides a microscale healed configuration. In order to better design this self-healing system, understanding of the SMP fibers under cyclic loading is essential because this system is claimed to repeatedly heal damage.

To this end, a multiscale approach is developed in this work toward incorporating more realistic material inputs. We aims at developing a multiscale approach because it provides correlation between micro-constituent governing behaviors and macroscale mechanical responses and it can describe the physics of the deformation more accurately when it is compared with the pure phenomenological models. In this work two well-established viscoplastic theories for the amorphous and crystalline polymers are presented. These theories are based on certain physical description of the viscoplastic deformation mechanisms in each of these sub-phases and the material constants are related to certain physical properties of them. These two constitutive relations are linked within the micromechanics framework to build the macroscale mechanical responses. The averaging micromechanics techniques are utilized herein and certain numerical approaches are adopted to take care of non-linearity, i.e. plasticity and damage, in each of the sub-phase [14-18]. Speaking in general the individual micro-constituents mechanical behaviors may vary when they are packed in a multiphase material system and a certain deviation in their mechanical responses may exist between the individual and their assembled configurations. However, this deviation is considered negligible herein. In section 2 the basic thermodynamic governing relations are reviewed and in section 3 the experimental characterization of SMP fibers are presented. In section 4 the micromechanics framework is discussed and in section 5 the constitutive relations for each of the sub-phases are presented. In section 6 the damage theory is formulated and in section 7 the computational aspect of numerical implementation of the proposed multiscale scheme is discussed. The results and discussions are presented in section 8. Bold face notation show tensorial parameters while scalars are shown by light face. Hereinafter the operators ".", ":" and "::" denote respectively the contraction of one, two and four indices for the tensorial multiplications.

5.3 Thermodynamics of coupled plasticity-damage process

In the case of finite deformation process, the Helmholtz free energy density takes the following form:

$$\psi = \psi\left(\mathbf{C}, \mathbf{C}^{(p)}, \mathbf{C}^{(d)}, \boldsymbol{\phi}, \aleph, \Omega, T, \delta T\right) \tag{5-1}$$

where $\mathbf{C}$, $\mathbf{C}^{(p)}$ and $\mathbf{C}^{(d)}$ are respectively the total, plastic and damage right Cauchy-Green tensors, $\boldsymbol{\phi}$ is the damage tensor, second order tensors $\aleph$ and Ω are kinematic hardening variables due to plasticity and damage processes, respectively; and T and δT are respectively the temperature and its gradient.

Let σ denote the Cauchy stress which is force per unit deformed area at the spatial configuration. The first Piola-Kirchhoff stress is the applied force per unit undeformed area at the spatial configuration and is defined by: $\mathbf{K} = \det(\mathbf{F})\,\boldsymbol{\sigma}$ and the second Piola-Kirchhoff stress which is defined in the material configuration is the force per unit undeformed area and is expressed by: $\mathbf{S} = \mathbf{F}^{-1}\mathbf{K}\mathbf{F}^{-\mathbf{T}}$ [19-21].

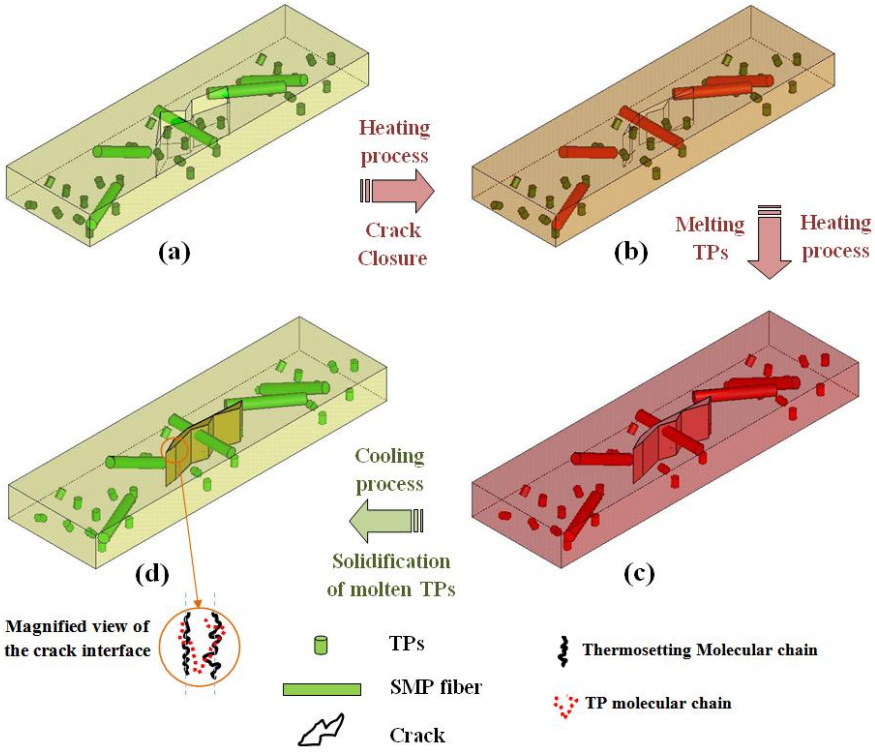

Figure 5-1 Schematic representation of the bio-mimetic self-healing material system (a) damaged configuration with a macroscale crack, (b) closed crack configuration due to the stress recovery process of SMP fibers, (c) diffusion of the molten Thermoplastic Particles (TPs) into the cracked matrix and (d) healed configuration with magnified view of the crack interface which shows molecular entanglement of the solidified TPs and thermosetting polymer molecular chain

The applied energy to the material system is then decomposed in three major segments as discussed by [4, 22]:

$$\psi = W\left(\mathbf{C}, \mathbf{C}^{(p)}, \mathbf{C}^{(d)}, \boldsymbol{\phi}, T\right) + H(\aleph, \Omega) + G_d(\boldsymbol{\phi}) + Q(\delta T) \qquad (5\text{-}2)$$

where W is the elastic energy stored in the material system due to the elastic deformation and it is recoverable upon unloading. The hardening function H takes into account the effect of hardening mechanisms due to inelastic and damage processes. The hardening effects may include the dislocation formation and movement in metallic crystalline microstructures or entropic changes in polymer

networks. Once the local energy exceeds the crystalline binding energy or the strength of polymeric network, new micro-surfaces, which are termed microcracks herein, are formed within the material system. The surface energy function G_d takes into account the energy dissipations due to formation of new microsurfaces and is the representative term for the damage process. The heat dissipation during such an irreversible thermodynamic process, e.g. plasticity and damage, is captured by the energy function Q.Consequently the dissipation energy is divided into the (i) plastic deformation, (ii) formation of microcracks and (iii) heat release.

As discussed above the microscale damage formations are controlled by the surface energy function G_d. In general the polymeric networks are either amorphous or semicrystalline. In crystalline metallic material systems once the local applied stress exceeds the binding energy the crystal slippage system is activated and dislocations are formed. Through further loading separation between crystalline slip planes may occur and produce a microscale crack, as depicted in Fig. 5-2(c). Although in a polymeric material system the governing plasticity and damage mechanisms follow different physics the conceptual damage initiation process remains the same as metals. The amorphous network consists of a series of randomly dispersed polymer chains while in a crystalline network these polymer chains are folded in a certain direction. As shown in Fig. 5-3, in the case of amorphous polymers, the applied stress results in conformational changes in polymeric network, Fig. 5-3(b), in which the chains rotates to orient along the loading direction and upon further loading the chains stretch to a certain limit λ_L Fig. 5-3(c), and then they break once the applied stretch is greater than λ_L and produce a microcrack in Fig. 5-3(d). In Figs. 5-2 and 5-3 the deformation mechanisms are shown by elastic, $F^{(e)}$, plastic, $F^{(p)}$, and damage, $F^{(d)}$, deformation gradient tensors. Inelastic deformation of crystalline phase in semicrystalline polymers includes three different mechanisms: (a) crystallographic slip, (b) twining and (c) Martensite transformations (Stevenson, 1995).

As shown in Figs. 4-2 and 4-3 the microcrack formation between the two presented classes of materials includes different damaging mechanisms. On the other hand these microcrack formation mechanisms enforce the definition of the surface function G_d which is the governing term in prediction of the damage initiation and growth. In Continuum Damage Mechanics (CDM) the designers of the material systems can correlate the thermodynamics of the damage process to the measurable mechanical properties such as changes in elastic stiffness [23]. Here due to the complexity of the deformation mechanism in SMP fibers a new approach is adopted within CDM framework in which the functionality of the SMP fibers is calibrated against the state of the damage as discussed in section 6.

Fig. 5-4 schematically shows the cyclic response of SMP fibers, in which an irregular inelastic deformation in tension and excessive reversible inelastic strains in unloading are illustrated. The theory presented in this work is based on multiplicative decomposition of the deformation gradient into the elastic, $\mathbf{F}^{e}$, and viscoplastic-damage, $\mathbf{F}^{vpd}$, gradients as follows [19-21]:

$$\boldsymbol{F} = \boldsymbol{F}^{e}\,\boldsymbol{F}^{vpd} \tag{5-3}$$

The viscoplastic-damage gradient tensor, $\mathbf{F}^{\mathrm{vpd}}$, is further decomposed to the Unloading viscoplastic, $\mathbf{F}^{\mathrm{vp\,(Unl)}}$, which measures the reversed inelastic deformations during the unloading process and Residual viscoplastic-damage, $\mathbf{F}^{\mathrm{vpd\,(Res)}}$, which is the residual inelastic-damaged strains after unloading process:

$$\boldsymbol{F}^{vpd} = \boldsymbol{F}^{vp\,(Unl)}\boldsymbol{F}^{vpd\,(Res)} \tag{5-4}$$

In order to provide an experimentally admissible procedure to measure the damage, the residual inelastic-damaged strains are assumed to be decomposed into the Recoverable viscoplastic gradient tensor, $\boldsymbol{F}^{vp\,(Rec)}$, which is measured through the recovery process of SMP fibers, and Irreversible viscoplastic gradient tensor, $\boldsymbol{F}^{vp\,(Irr)}$, which takes into account all residual inelastic strains. The Damaged gradient tensor, $\boldsymbol{F}^{d}$, accounts for the microcracks formation and polymeric chain failures. Then Eq. (5-3) by substituting the above gradients is reduced to:

$$\boldsymbol{F} = \boldsymbol{F}^{e}\ \boldsymbol{F}^{vp\,(Rec)}\ \boldsymbol{F}^{vp\,(Irr)}\boldsymbol{F}^{d}\boldsymbol{F}^{vp\,(Unl)} \tag{5-5}$$

One may assume small elastic and finite viscoplastic and viscodamage deformations. The additive decomposition of the Lagrangian elastic, $\boldsymbol{\epsilon}^{\mathrm{e}}$, and viscoplastic-damage, $\boldsymbol{\epsilon}^{\mathrm{vpd}}$, strain is a fundamental assumption in viscoplasticity return mapping solution algorithms [21, 24]:

$$\boldsymbol{\epsilon} = \boldsymbol{\epsilon}^{e} + \boldsymbol{\epsilon}^{vpd} \tag{5-6}$$

This additive decomposition is extended for the presented deformation mechanism in Eq. (5-5) as follows:

$$\begin{aligned}\boldsymbol{\epsilon}^{vpd} = &\left|\left|\epsilon^{vp\,(Rec)}\right|\right|\boldsymbol{n}^{vp\,(Rec)} + \left|\left|\epsilon^{vp\,(Irr)}\right|\right|\boldsymbol{n}^{vp\,(Irr)} + ||\phi||\boldsymbol{n}^{(d)} \\ &+ \left|\left|\epsilon^{vp\,(Unl)}\right|\right|\boldsymbol{n}^{vp\,(Unl)}\end{aligned} \tag{5-7}$$

where$||\quad||$ shows the norm of the second order tensors, and the second order tensor, $\mathrm{n}^{(\#)}$, represents the flow direction for their corresponding phenomenon. Each of the terms in Eq. (5-7) requires an evolution law and they will be proposed in section 5 where the governing constitutive relations are introduced.

5.4 SMP fibers characterization

In the following the experimental results regarding microstructural changes of the SMP fibers are presented and then the governing relations for each of the sub-phases are introduced in the next section.

These relations are then correlated to the macroscopic mechanical responses through the micromechanics framework.

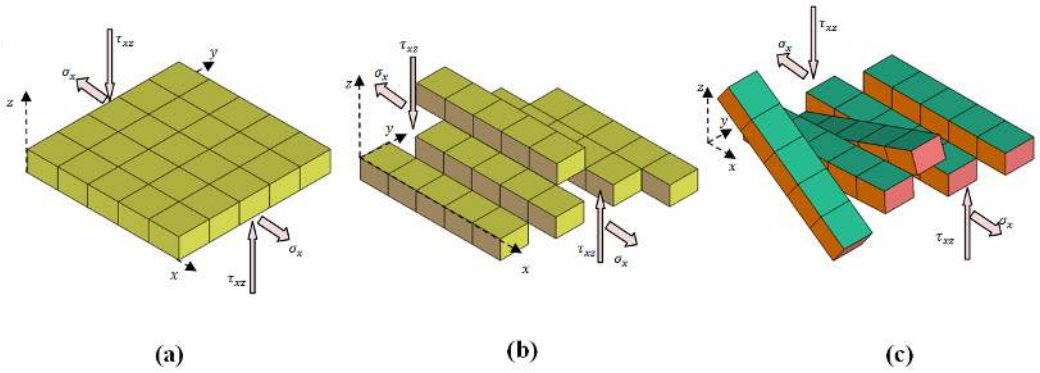

Figure 5-2 Crystalline microstructure under biaxial loading condition (a) undeformed body, (b) formation of different type of dislocation due to the external loading condition and (c) microcrack formation.

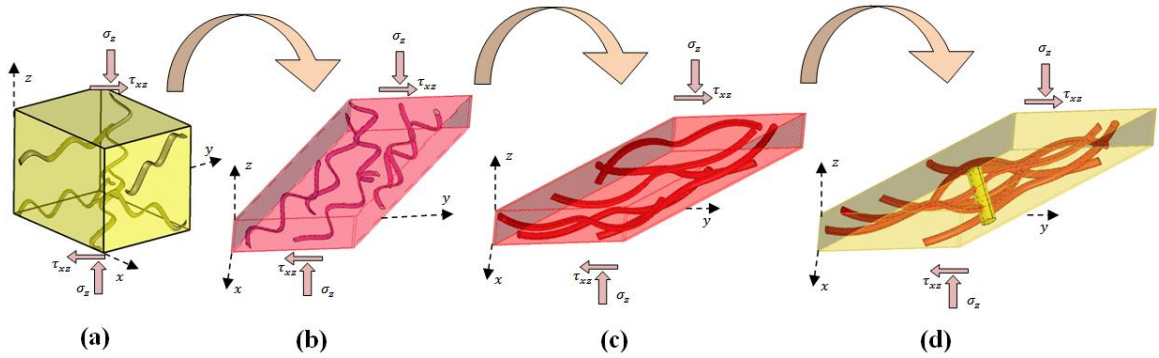

Figure 5-3 Polymeric network under biaxial loading condition, (a) undeformed body, (b) conformational changes due to external loading, (c) stretched chains after saturation of conformational changes and (d) microcrack formation due to breakage of polymer chain.

SMP fibers are mainly manufactured from thermoplastic SMPs, particularly polyurethane [25]. The polyurethane semicrystalline SMP fibers are constituted from the crystalline hard phase and amorphous soft phase. This class of SMP shows excellent solution ability, melting, diffusion, processability, and

repeatability of the Shape Memory (SM) cycle and they are prominent candidates for smart materials applications [26]. Soft segment amorphous phase may be constituted from the polyester or polyether or semi-crystalline polymers such as poly(ε-caprolactone) (PCL) structures. The crystalline hard segments (e.g. diisocyanate (TDI), aromatic urethane or aramid) are dispersed over the soft segment to form thermally stable chemical or physical cross links. These distinguishable sub-phases in the polyurethane elastomers provides the physical basis for a micromechanics based formulation in which a multiscale analysis is implemented to correlate the micro and macro scales [27].

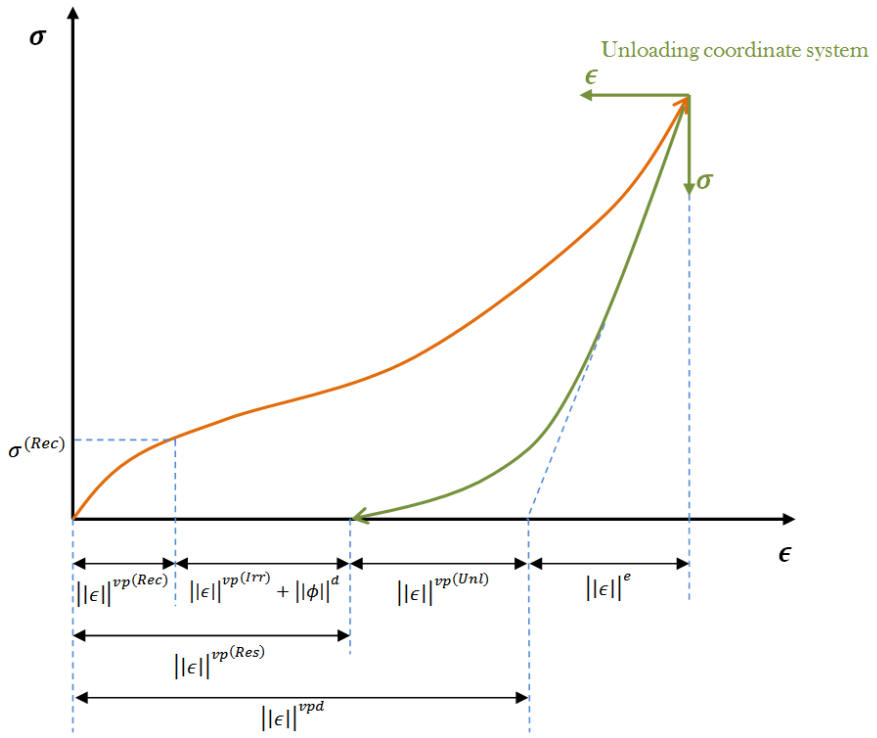

Figure 5-4 Schematic representation of loading-unloading process for SMP fibers

In this study, polyurethane SMP fibers are synthesized from poly(butylene adipate)-600 (Mn) (PBA), 4'4 -diphenylmethane diisocyanate (MDI) and 1,4-butanediol (BDO). On average, the mole ratio of (MDI+BDO): PBA=3:1. The average formula weight ratio of (MDI+BDO): PBA=1021:650. The hard segment, soft segment, and their contents were selected to prepare polyurethane with amorphous soft segment phase and crystalline hard segment phase. The polyurethane fiber was spun by melt spinning. The fiber passed three pairs of rollers with the same rotation speed before being wound up. It has been found that programming below the transition temperature is a faster way of programming SMPs and also a way of enhancing the recovery stress, as evidenced by cold-drawing programming of thermoplastic SMPs [28] and cold-compression programming of thermosetting SMPs (Li and Xu, 2011). In a previous study [13], the SMP fibers were cold-drawn programmed. Polarized Optical Microscope image validated

the molecular alignment along the loading direction after cold-drawn programming. This observation was further evidenced by Small Angle X-ray Scattering, showing orientation change of microstructures after programming. Dynamic Mechanical Analysis test showed a shift of the glass transition temperature towards higher temperature, and a higher storage modulus for the strain hardened SMP fiber as compared to the as received counterparts.

5.5 Micromechanics Formulation

The semicrystalline polyurethane SMP contains different shapes of crystalline hard phase, which might be treated as inclusions, and the macroscopic stress field strongly depends on the volume fraction and orientation of these inclusions and interfacial properties between the crystalline hard phase and the amorphous soft phase. Moreover, the microstructural changes during the cold-drawing processes affect the macroscopic stress field and these effects should be considered in evaluating the macroscopic constitutive behaviors. Then a multiscale micromechanic based theory, which couples the viscodamage and viscoplasticity processes in each of the micro-constituents to the macroscale fields, provides an excellent correlation between the microscale and macroscale mechanical responses. Fig. 5-5 presents a schematic view of the considered Representative Volume Element (RVE) for the SMP fiber in this work, in which Fig. 5-5(a) shows dispersed hard phases and Fig 4-5(b) shows the stretched RVE with changed microstructures.

This multiscale approach provides enough flexibility to capture a vast range of mechanical responses while the simulation relies on physical based constitutive relations. The well-known rule of mixture is utilized here to link the microscale stress fields to the macroscale stress as follows:

$$\boldsymbol{\sigma} = c(0)\boldsymbol{\sigma}^{(0)} + c(1)\boldsymbol{\sigma}^{(1)} \tag{5-8}$$

where $c(i), i = 1,2$ represents the volume fractions of sub-phases and indices 0 and 1 respectively indicate the amorphous and crystalline phases. These volume fractions will be updated based on stress induced crystallization process and the microscale stresses, i.e. $\boldsymbol{\sigma}^{(0)}$ and $\boldsymbol{\sigma}^{(1)}$, take into account the microstructural changes during the cold drawing process. The stress induced crystallization process is experimentally investigated in the literature by many researchers [29-31]. In this work it is assumed that this process is related to the accumulated viscoplastic strain and its rate and it is computed based on the loading history. The following evolution law is proposed to update the crystalline and subsequently the amorphous volume fractions as follows:

$$\dot{c}(1) = \psi\, |\dot{p}| c_0(1)\, exp(-\psi\, |p|) \tag{5-9}$$

where $|p| = \sqrt{2\boldsymbol{\epsilon}^{vp} : \boldsymbol{\epsilon}^{vp}}$ is the effective accumulated viscoplastic strain and ψ is a microstructural related material parameter to control the crystallization process. Rate equation (9) provides an incremental evolution for the stress induced crystallization process and saturates at high inelastic strains.

The physical description for selecting such a behavior is that the stress induced crystallization is expected to be saturated at some inelastic strain range in which upon further loading failure of the polymeric network occurs. In other words, the stress induced crystallization is assumed to occur prior to the microcrack formations and saturates to a certain limit which is governed by the microstructure. Exploring the actual volume fractions for each of these sub-phases is experimentally difficult and some hypothetical values are assumed herein for these volume fractions. This may not undermine the generality of the proposed model because of the fact that upon establishment of the real volume fractions of the crystalline and amorphous phases, these values can be easily mapped to the assumed hypothetical ones and the results are still valid. As discussed later in section 7, the stress induced crystalline volume fraction is partially recovered upon each unloading while at the end of each of the loading-unloading cycles a certain amount of stress induced crystalline phase is frozen which consequently results in higher elastic stiffness at subsequent cycles.

To account for the microstructural changes during the cold-drawing process the textures in the amorphous and crystalline phases and the morphological texture, which account for the interfacial changes between the hard and soft phases, are updated incrementally. These updates are presented in the next section after establishment of the micro-constituents governing relations.

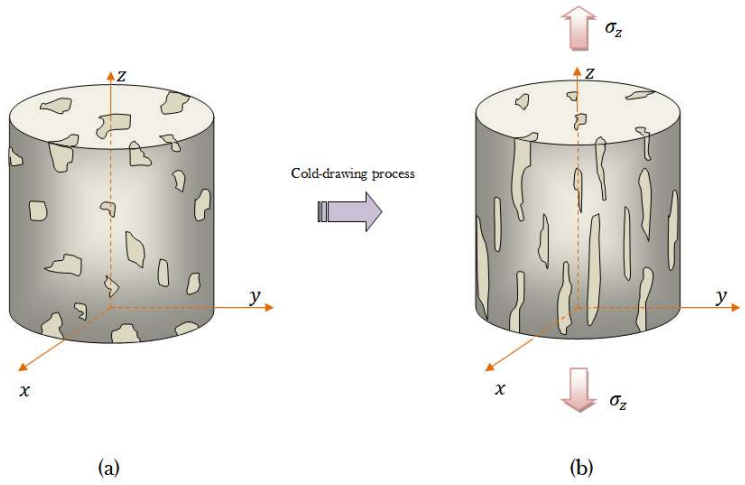

Figure 5-5 RVE (a) non-stretched SMP fiber, and (b) stretched SMP fiber

5.6 Micro-constituents governing relations

As discussed before the semicrystalline polyurethane SMP is constituted from crystalline hard phase which are randomly dispersed in an amorphous matrix. The amorphous phase is constituted from randomly folded polymeric chains while in the crystalline phase these folded chains are oriented in

parallel configurations. This phase can be produced during the manufacturing process, where the spherulite crystalline structures are formed under isotropic conditions (Fig. 5-6(a)). Once physical constraints are imposed during the manufacturing process or external loading condition is applied to the manufactured crystalline phase, the crystalline phase shows chain alignment with respect to these external confinements as shown in Fig. 5-6(b). The last phenomenon is termed as the *stress induced crystallization* in the literature [32, 33].

Speaking in general a system of coupled governing differential equations are required to take into account the amorphous and crystalline damage, viscoplasticity, molecular texture and morphological texture updates. In the following these constitutive equations for the sub-phases are presented in a systematic approach in which each of the individual terms in Eq. (5-7) is introduced. These governing relations are later coupled with the micromechanics formulation to predict the macroscopic mechanical behaviors. The computational implementation is discussed in section 6 for such a multiscale analysis.

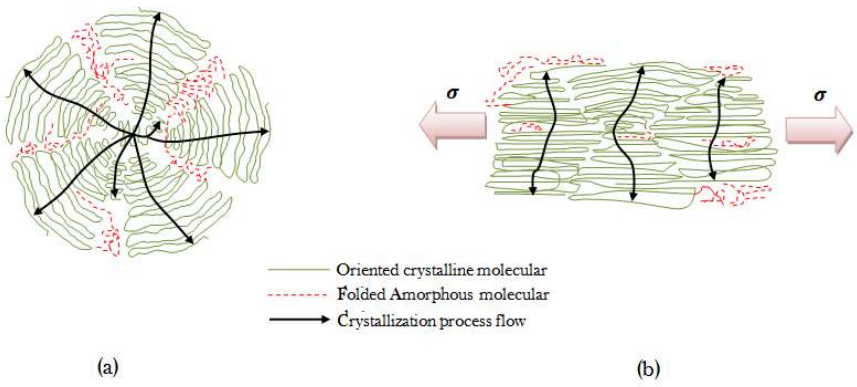

Figure 5-6 Semicrystalline morphology (a) manufacturing induced spherulite microstructure under isotropic conditions and (b) stress induced crystallized microstructure

5.6.1 Amorphous soft phase constitutive relation:

The rate dependent Argon theory describes the viscoplastic deformation of polymers based on double kink formations and the intermolecular resistant, which is the free energy barrier to chain segment rotation [34]. Boyce and coworkers developed this theory to a pressure and temperature dependent version [35-40]. This model is assumed to be held for the amorphous phase of the semicrystalline SMP fiber. The plastic multiplier in this model is introduced as follows (Boyce et al., 1989):

$$|\dot{\gamma}^p| = \dot{\gamma}_0^a \, exp\left[-A\,\frac{s + a\,p}{\Theta}\left(1 - \left(\frac{|\tau|}{s + a\,p}\right)^{5/6}\right)\right] \tag{5-10}$$

where Θ is the absolute temperature, and a is a material parameter, p is pressure and s is the athermal shear strength. The material parameter A and the evolution law for s are defined as follows:

$$A = \frac{39\pi\omega^2\bar{a}^3}{16k}\,;\;\; \dot{s} = h\left(1 - \frac{s}{s_{ss}(\Theta,|\dot{\gamma}^p|)}\right)|\dot{\gamma}^p|^{(a)}. \tag{5-11}$$

where ω and $\bar{a}$ are material parameters and k is the Boltzmann's constant (Argon, 1973). The material parameter h shows the rate of the strain softening and s_{ss} represents the asymptotic preferred structure. The initial value of s for the annealed material is: $s_0 = \frac{0.077\mu}{1-\nu}$, where μ is the elastic shear modulus and ν is the Poisson's ratio.

The material constant $\dot{\gamma}_0^a$, in Eq. (5-10), is called amorphous pre-exponential inelastic strain rate, and $|\dot{\gamma}^p|^{(a)} = \sqrt{2\dot{\boldsymbol{\epsilon}}^{p\,(a)} : \dot{\boldsymbol{\epsilon}}^{p\,(a)}}$ is the effective equivalent inelastic deformation rate of the amorphous phase subjected to the effective equivalent shear stress, |τ|, which is defined as follows:

$$|\tau| = \sqrt{\frac{1}{2}\boldsymbol{S}^*:\boldsymbol{S}^*} \tag{5-12}$$

where $\boldsymbol{S}^* = \boldsymbol{S} - \boldsymbol{X}$ in which $\boldsymbol{S} = \boldsymbol{\sigma} - \sigma^h\boldsymbol{\delta}$ is the deviatoric Cauchy stress and $\sigma^h = \frac{1}{3}(\sigma_1 + \sigma_2 + \sigma_3)$ and $\boldsymbol{X} = \boldsymbol{\alpha} - \alpha^h\boldsymbol{\delta}$ is the deviatoric back stress tensor and $\alpha^h = \frac{1}{3}(\alpha_1 + \alpha_2 + \alpha_3)$ which is defined as follows [35]:

$$\boldsymbol{\alpha} = nk\Theta\,\frac{\boldsymbol{\lambda}^L}{3}\left[\boldsymbol{\lambda}^p\mathcal{L}^{-1}\left(\zeta\,\frac{\boldsymbol{\lambda}^p}{\boldsymbol{\lambda}^L}\right) - I_1^p\mathcal{L}^{-1}\left(\zeta\,\frac{\boldsymbol{\lambda}^p}{\boldsymbol{\lambda}^L}\right)\boldsymbol{\delta}\right] \tag{5-13}$$

where $I_1^p = \frac{1}{3}(\lambda_1^p + \lambda_2^p + \lambda_3^p)$ and n is the number of chains per unit volume, k is the Boltzmann's constant, and λ^L is the limit of chain extensibility and ζ is a viscoplastic related material constant which controls the magnitude of the hardening with respect to the inelastic stretches. In limit analysis Langevin function, $\mathcal{L}(\beta) = \coth(\beta) - 1/\beta$, is used extensively and it imposes a limiting case in the evolution of the back stress tensor. Although the $\mathcal{L}^{-1}(\beta)$ can be obtained numerically, here an approximated Taylor series solution is utilized to obtain the inverse of the Langevin function as follows [41]:

$$\mathcal{L}^{-1}(\beta) = 3\beta + \frac{9}{5}\beta + \frac{297}{175}\beta^2 + \frac{1539}{875}\beta^7 + \cdots \tag{5-14}$$

Eq. (5-14) represents the magnitude of the amorphous inelastic strain rate; while the direction of the amorphous viscoplastic flow rate, $\dot{\boldsymbol{\epsilon}}^{vp\,(a)}$, is governed by the deviatoric driving stress, $\mathbf{S}^*$. The following flow rule is then proposed for the inelastic deformation in the amorphous phase [38]:

$$\left\|\dot{\boldsymbol{\epsilon}}^{vp\,(a)}\right\| \boldsymbol{n}^{vp\,(a)} = |\dot{\gamma}^{p}|^{(a)} \frac{\boldsymbol{S}^*}{\sqrt{2}|\tau|} \tag{5-15}$$

5.6.2 Crystalline hard phase constitutive relation:

The crystalline phase in the semicrystalline polymers may undergo three different inelastic deformation mechanisms including (a) crystallographic slip, (b) twining and (c) Martensite transformations [32]. In this work the slippage mechanism is assumed to be the dominant influencing mechanism. To consider the crystallographic texture changes upon stretching a vector, $\boldsymbol{x}$, is aligned with the crystallographic texture in which its evolution with deformation shows the texture updates. Two active slip mechanisms in the polymeric slippage system have been taken into account which are: (a) *chain slip*: the burgers vector is aligned with $\boldsymbol{x}$ and (b) *transverse slip*: the burgers vector is perpendicular to $\boldsymbol{x}$ [42]. As discussed by Parks and Ahzi, in the semicrystalline polymers there are only four linearly independent crystalline slip systems, which are indicated by the unit vectors in the direction of the slip and normal to the slip planes including: (i) chain slip: (100)[001] and (010)[001], and (ii) transverse slip: (100)[010] and (010)[100] [42]. Vector $\boldsymbol{s}^{(\alpha)}$ denotes the slip direction and vector $\boldsymbol{n}^{(\alpha)}$ represents the unit normal vector to the slip plane, where $\alpha = 1$ to 4 is the number of the slip systems. The viscoplastic crystalline deformation rate tensor, $\dot{\boldsymbol{\epsilon}}^{vp\,(c)}$, is given by [43]:

$$\left\|\dot{\boldsymbol{\epsilon}}^{vp\,(c)}\right\| \boldsymbol{n}^{vp\,(c)} = \sum_{\alpha=1}^{K} \dot{\gamma}^{(\alpha)} \boldsymbol{R}^{(\alpha)}, \tag{5-16}$$

where $R^{(\alpha)}$ is the symmetric part of the Schmid tensor as defined by: $\boldsymbol{R}^{(\alpha)} = \frac{1}{2}\{\boldsymbol{s}^{(\alpha)} \otimes \boldsymbol{n}^{(\alpha)} + \boldsymbol{n}^{(\alpha)} \otimes \boldsymbol{s}^{(\alpha)}\}$, where $\otimes$ shows the dyadic multiplication; $\boldsymbol{R}^{(\alpha)}$ represents the α^{th} crystalline slip plane and the shear rate, $\dot{\gamma}^{(\alpha)}$, is defined as follows [44, 45]:

$$\dot{\gamma}^{(\alpha)} = |\dot{\gamma}^{p}|^{(c)} \frac{\tau^{(\alpha)}}{g^{(\alpha)}} \left|\frac{\tau^{(\alpha)}}{g^{(\alpha)}}\right|^{n^c - 1} \tag{5-17}$$

where $|\dot{\gamma}^{p}|^{(c)}$ is the crystalline reference inelastic strain rate and $g^{(\alpha)}$ is the shear strength for the α^{th} slip system, and n^c is the rate sensitivity factor. Due to the inextensibility assumption of the crystalline chains together with the incompressible plastic flow a constraint is enforced on the effective shear stress, $\tau^{(\alpha)}$, at the α^{th} slippage system, as follows [43]:

$$\tau^{(\alpha)} = \boldsymbol{S}^{*(c)} : \boldsymbol{R}^{(\alpha)}, \tag{5-18}$$

where $\boldsymbol{S}^{*(c)}$ is the projected deviatoric Cauchy stress, **S**, in the direction of the deviatoric part of the dyadic $\boldsymbol{x} \otimes \boldsymbol{x}$ which is defined as $\mathbf{V} = \boldsymbol{x} \otimes \boldsymbol{x} - \frac{1}{3}\boldsymbol{I}$, [43]. The lattice spin which controls the rate of changes of the direction of $\boldsymbol{x}$ is introduced as follows [45, 46]:

$$\boldsymbol{W}^{*} = \boldsymbol{W}^{(c)} - \boldsymbol{W}^{p\,(c)}, \tag{5-19}$$

where $\boldsymbol{W}^{(c)} = \frac{1}{2}\left(\boldsymbol{L}^{(c)} - \boldsymbol{L}^{(c)^T}\right)$is the spin tensor in the crystalline phase, $\boldsymbol{L}^{(c)} = \dot{\boldsymbol{F}}^{(c)}\boldsymbol{F}^{(c)^{-1}}$ is the velocity gradient in the crystalline phase and ' $\dot{}$ ' denotes the time derivative, and $\boldsymbol{W}^{p\,(c)} = \sum_{\alpha=1}^{K} \dot{\gamma}_0^c \, \boldsymbol{A}^{(\alpha)}$ is the plastic spin tensor in the crystalline phase with $\boldsymbol{A}^{(\alpha)} = \frac{1}{2}\left\{\boldsymbol{s}^{(\alpha)} \otimes \boldsymbol{n}^{(\alpha)} - \boldsymbol{n}^{(\alpha)} \otimes \boldsymbol{s}^{(\alpha)}\right\}$, which is the skew part of the Schmid tensor.

5.6.3 Cyclic updates:

SMP fibers show a primary softening region in tensile which follows by an irregular strain hardening response. Based on experimental observations at high cyclic tensile loads the strain hardening responses at high strain levels is aggrandized which can be an indication of the saturation of conformational changes in polymeric network. In this work the microstructural changes due to the cold-drawing process are updated based on physical descriptions of the deformation mechanisms. In other words, the cyclic hardening of the SMP fibers are attributed to: (i) the saturation of the conformational changes in the amorphous phase in which the Langevin element response should be updated based on the residual viscoplastic strains; (ii) updating the molecular network texture in the amorphous phase; (iii) modeling the crystallographic axes changes in the crystalline phase upon cold drawing process. It is assumed that the crystalline axes undergo rotation and extension during the stretching while upon unloading a portion of these rotations and extensions are reversed. In such a way the configuration of the crystalline phase is updated in each of the cycles; (iv) accounting for the morphological updates in the semicrystalline RVE in which the interfacial vectors updates represent the overall morphology of the RVE . These topics are addressed in the following subsections:

(i) Cyclic update of the Langevin element:

The amorphous polymer mechanical responses show a primary softening region in tensile which follows by an irregular strain hardening response. Based on experimental observations the cyclic responses of SMP fibers follow the same saturation process of the polymeric network stretch. To capture this behavior the Langevin function is updated during each loading based on the following governing relation:

$$\dot{\zeta} = \aleph(\kappa - \zeta)|\dot{p}| \tag{5-20}$$

where $\aleph$ and κ are material related constants and $|\dot{p}| = \sqrt{2\dot{\boldsymbol{\epsilon}}^{vp\,(a)} : \dot{\boldsymbol{\epsilon}}^{vp\,(a)}}$ is the effective shear plastic strain rate. Eq. (5-20) evaluates the controller coefficient ζ based on the loading history and allows the Langevin element to show dominant effects at higher cycles while at low cycles its effect is negligible. In such a way at higher cycles the amorphous polymeric network shows stiffer stretches which is in line with the experimental observations. It is assumed in this work that only during the tensile loadings the Langevin function is active while during the unloading this element is turned off.

(ii) Cyclic texture update in the amorphous phase:

Boyce et al. showed that the amorphous tensile yield stress is highly dependent on the orientation and initial texture of the polymeric chains [40]. It is common to neglect the texture effect in an elastic deformation and consider it only during an inelastic deformation by incorporating initial values for the back stress tensor, $\boldsymbol{\alpha}$, athermal shear resistance, s, network stretch vector, $\boldsymbol{\Lambda}^{(a)}$, and residual stress tensor, $\boldsymbol{\sigma}^{(a)}$ (Boyce et al., 1989).

(iii) Cyclic texture update in the crystalline phase:

Let the crystalline texture be represented by a crystallographic vector, $\boldsymbol{x}$. This vector can be affected by the induced rotation in a large deformation process. The following rate equation takes into account the changes in direction of the crystallographic axes with respect to the second order skew symmetry spin tensor $\boldsymbol{W}^*$ [13, 46]:

$$\dot{\boldsymbol{x}} = \boldsymbol{W}^* \,.\, \boldsymbol{x} \tag{5-21}$$

The incremental form of Eq. (5-21) is given by: $\dot{\boldsymbol{x}} = \exp(\boldsymbol{W}^* \Delta t)\, \boldsymbol{x}(t)$ where Δt indicates the time increment. Based on the Cayley-Hamilton expression for exponential term, one may find the following expression:

$$exp(\boldsymbol{W}^* \Delta t) = \boldsymbol{I} + \frac{\sin w}{w} \boldsymbol{W}^* \Delta t + \left(\frac{1 - cosw}{w^2}\right) \boldsymbol{W}^* : \boldsymbol{W}^* \Delta t^2 \tag{5-22}$$

where ":" denotes the contraction of indices and $w^2 = -tr(\boldsymbol{W}^* : \boldsymbol{W}^* \Delta t^2)/2$.

The crystallographic axes, $\boldsymbol{x}$, is computed based on the applied stretching gradients during the loading process based on Eq. (5-21). The evolved texture at the end of the loading process is introduced to the unloading computation module to update it during the unloading process in which a portion of the stored crystallographic texture changes is reversed. The reversible part of the applied texture changes is

assumed to be related to the loading conditions, loading history and material parameters and the following evolution law is proposed:

$$\dot{\boldsymbol{x}}^{(Rev)} = -\boldsymbol{\Omega}_1 \exp\left(-\Omega_2 \left|\gamma^p\right|^{(c)}\right) \tag{5-23}$$

where the material parameters $\boldsymbol{\Omega}_1$ and Ω_2 respectively control the rate and the final value of the convergence. It is worthy of noting that $\dot{\boldsymbol{x}}^{(Rev)}$ is computed incrementally during the loading process and its final value is introduced into the subsequent unloading process.

(iv) Morphological texture updates:

In this work the crystals are treated as inclusions embedded in the amorphous phase [47]. The morphology of such a multiphase system undergoes excessive variations in a large deformation process and a proper description for such a morphological texture update is required. Basically this task is accomplished by updating the interfacial normal vectors in which the deformation gradient is used to compute the variation in these normal vectors. Let the material coordinate system at the interface plane be indicated by two infinitesimal independent vectors, $\delta\boldsymbol{x}^{(1)}$ and $\delta\boldsymbol{x}^{(2)}$ at time $t = 0$. At generic time t, these vectors are transformed respectively to the $\boldsymbol{F}(t).\delta\boldsymbol{x}^{(1)}$ and $\boldsymbol{F}(t)\delta\boldsymbol{x}^{(2)}$ where $\boldsymbol{F}(t)$ is the deformation gradient. Then the following expression for the normal vector $\boldsymbol{n}^I$ is trivial:

$$\boldsymbol{n}^I(0) = \frac{\delta\boldsymbol{x}^{(1)} \times \delta\boldsymbol{x}^{(2)}}{|\delta\boldsymbol{x}^{(1)} \times \delta\boldsymbol{x}^{(2)}|} \tag{5-24}$$

$$\boldsymbol{n}^I(t) = \frac{\boldsymbol{F}(t).\delta\boldsymbol{x}^{(1)} \times \boldsymbol{F}(t).\delta\boldsymbol{x}^{(2)}}{|\boldsymbol{F}(t).\delta\boldsymbol{x}^{(1)} \times \boldsymbol{F}(t).\delta\boldsymbol{x}^{(2)}|} \tag{5-25}$$

Consequently one may assume a specific RVE configuration prior to the loading and then compute the changes of the interfacial normal vectors, $\boldsymbol{n}^I$, for each of the inclusions to update the morphological texture changes.

5.7 Cyclic damage analysis

Due to the high rate dependency in mechanical responses of SMP fibers, a viscous damage model is adopted in this work. Formulation of the damage mechanics with respect to the Zener parameter provides enough flexibility to formulate a rate and temperature dependent damage theory [48-51]:

$$\dot{\boldsymbol{\phi}} = \left|\left|\dot{\boldsymbol{\phi}}\right|\right| \boldsymbol{n}^d = \theta(T) Z \boldsymbol{n}^d \tag{5-26}$$

where $\theta(T)$ introduces the temperature dependency in the damage evolution and it is represented by Arrhenius function of temperature; Z is the Zener parameter and $\boldsymbol{n}^d$ represents the direction of the damage flow. The proposed damage theory utilizes the same concept as viscous stresses in plasticity theory and Zener parameter controls the rate of changes for the viscous damage conjugate force as follows [48, 51]:

$$Z = Z_{ss}\left[f\left[\frac{<\boldsymbol{y}^d - \boldsymbol{y}^{dK} > -1}{D^d}\right]\right] \geq 0 \tag{5-27}$$

where $Z_{ss}[0] = 0$ and $\boldsymbol{y}^d$ and $\boldsymbol{y}^{dK}$ are respectively the damage and damage kinematic hardening thermodynamic conjugate forces and $D^d > 0$ is the drag strength and "<>" is the Macaulay brackets. Freed and Walker proposed different admissible functional forms for f, and in this work the power-law expression is adopted [48-50]. Neglecting the temperature dependency in the damage evolution, one may find:

$$\left|\left|\dot{\boldsymbol{\phi}}\right|\right| = \left[\frac{<\boldsymbol{y}^d - \boldsymbol{y}^{dK} > -1}{D^d}\right]^m \tag{5-28}$$

where $|\boldsymbol{y}^{dK}| = b|\boldsymbol{y}^d|$ with $0 < b < 1$ and m is the power of the viscosity dependence. Basically the damage conjugate force is derived based on the Helmholtz free energy function, Eq. (5-1), as discussed in detail by Voyiadjis et al. [5, 6]:

$$\boldsymbol{y}^d = -\rho\frac{\partial\psi}{\partial\boldsymbol{\phi}} \tag{5-29}$$

where ρ is the density. Based on thermodynamics governing relations the damage conjugate force is correlated to the Cauchy stress tensor as follows [5, 6]:

$$\boldsymbol{y}^d = -(\boldsymbol{\sigma}:\bar{\boldsymbol{L}}^{-1}:\boldsymbol{M}:\boldsymbol{\sigma}) :: \frac{\partial\boldsymbol{M}}{\partial\boldsymbol{\phi}} \tag{5-30}$$

where fourth order tensors $\bar{\boldsymbol{L}}$ and $\boldsymbol{M}$ are respectively the *undamaged stiffness* and *damage-effect* tensors, which relates the states of partially damaged configuration to the fictitious undamaged configuration. They are respectively defined in the context of *Micromechanics* and *Continuum Damage Mechanics* as follows [52]:

$$\begin{aligned}\overline{\boldsymbol{L}} &= c(0)\bar{\boldsymbol{L}}^{(0)} + c(1)\bar{\boldsymbol{L}}^{(1)}\\ \overline{\boldsymbol{\sigma}} &= \boldsymbol{M}:\boldsymbol{\sigma}\end{aligned} \tag{5-31}$$

where the over-bar shows the state of fictitious undamaged configuration and the relationship between damaged and undamaged stiffness tensors are given by Voyiadjis et al. [6]. A simple expression for the damage effect tensor is proposed as follows:

$$\boldsymbol{M} = [(\boldsymbol{I} - \boldsymbol{\phi}) : (\boldsymbol{I} - \boldsymbol{\phi})]^{1/2} \tag{5-32}$$

where $\boldsymbol{I}$ is the second order unity tensor. As discussed before the second order tensor $\boldsymbol{\phi}$ represents the reduction in functionality of SMP fibers in this work. The flow direction of the damage is given by second order tensor $\boldsymbol{n}^d$ as follows:

$$\boldsymbol{n}^d = \frac{\frac{\partial F^d}{\partial \boldsymbol{y}^d}}{\left\| \frac{\partial F^d}{\partial \boldsymbol{y}^d} \right\|} \tag{5-33}$$

where F^d is the damage potential surface and is defined based on the damage and damage kinematic hardening conjugate forces: $\boldsymbol{y}^d$ and $\boldsymbol{y}^{dK}$, rate dependent damage threshold $Y_d(\dot{\boldsymbol{\epsilon}})$, and damage isotropic hardening function $K(|\boldsymbol{\phi}|)$ as follows:

$$F^d = \left\{ \frac{(\boldsymbol{y}^d - \boldsymbol{y}^{dK}) : \boldsymbol{P} : (\boldsymbol{y}^d - \boldsymbol{y}^{dK})}{K(|\boldsymbol{\phi}|) + Y_d(\dot{\boldsymbol{\epsilon}})} + 1 \right\}^{1/2} - 1 \tag{5-34}$$

where fourth order tensor $\boldsymbol{P} = \boldsymbol{Z}^{-1}\boldsymbol{Z}^{-1}$ controls the damage initiation and growth rate. The second order tensor $\boldsymbol{Z}$ is introduced in the following:

$$\boldsymbol{Z} = \left(\lambda\eta \left(\frac{|\boldsymbol{\phi}|}{\lambda} \right)^{\boldsymbol{\zeta^d}} \boldsymbol{\delta}.\boldsymbol{\phi} + \boldsymbol{\delta}\lambda {\nu^d}^2 \right) \tag{5-35}$$

where $|\boldsymbol{\phi}| = \sqrt{2\boldsymbol{\phi} : \boldsymbol{\phi}}$ is the effective accumulated shear damage, λ is the Lame' constant and ζ^d, ν^d and η are material constants to introduce the damage hardening and damage threshold effects [5] and $\boldsymbol{\delta}$ is the Kronecker delta.

One of the milestones in calibrating the damage process in SMP fibers is to find an experimental way to measure the damages. As discussed by Voyiadjis et al. [4-6] the coupling between the damage and the viscoplastic responses is captured by calibrating the elastic modulus or hardness changes or measuring the damaged microsurfaces during a progressive damage mechanism such as fatigue damage [23, 53-55]. In the case of SMP fibers, these measurement techniques are not applicable, due to the high microstructural changes upon the cold-drawing process. In other words, the increasing stiffness due to the texture updates and stress-induced crystallization are coupled with the stiffness reduction due to the formation of microcracks. In order to provide a physically consistent method to capture the damage inside the SMP fibers, a new damage parameter is introduced herein as follows.

The main purpose of utilizing the SMP fibers is to gain the recoverable stresses upon the heating process in self-healing or other smart material systems. One may consider this functionality to provide an insight for the state of the damage inside the SMP fibers. Cyclic changes in the stress recovery, which are then measured after each loading-unloading cycle, provide an indication to the state of the damage inside these fibers. These measurements are demonstrated in Figs. 4-7 and 4-8 where the polyurethane SMP fiber with a diameter of 0.002 mm is cycled up to 150% and 300 % level of strains, respectively, and after the unloading, the recovery process is implemented. In the following the corresponding recoverable strains are measured through the constrained stress recovery in which the MTS machine picks the stresses and a controllable furnace applies the heat. The test procedure is as follows: (i) the SMP fiber is loaded-unloaded from zero stress level, (ii) the unloaded fiber is mounted on MTS machine and heat is applied by the furnace and the recovery stress level, $\sigma^{(rec)}$, is measured by the MTS, and (iii) the loading curve from step (i) is utilized to pick up the corresponding level of strain with respect to the $\sigma^{(rec)}$. Then the recovered stress level, $\sigma^{(rec)}$, at step (ii) is assumed to be a representative for the stored recoverable strains, $\left|\left|\boldsymbol{\epsilon}^{vp\,(Rec)}\right|\right|$, at step (i). It is imperative to mention that, the elastic stiffness of the SMP fiber is assumed to not vary significantly at the recovery temperature ranges. Thermal stability of the SMP fibers is shown by Li and Shojaei [56] and this property is of utmost important for deploying these fibers into the smart fiber-reinforced structures.

Fig. 5-7 shows that the recoverable stresses increase upon first four cyclic stretches, which can be explained by the fact that the maximum recoverable stresses correspond to some specific stored microstructure, and the cyclic loading gradually provides such a microstructural configuration. From cycle number five the amount of the stress recovery is reduced. This phenomenon is interpreted herein as the damage effect and this reduction of the functionality is utilized later to provide a physical means for the damage analysis. In Fig. 5-8 the SMP fiber is stretched up to 300% level of strain in each of the cycles and as it is obvious from Fig. 5-8(b), the damage mechanism is started from the first cycle and the amount of the recoverable stress is reduced monotonically.

The reduction of the functionality of SMP fibers upon cyclic loading and cyclic recoveries is interpreted as gradually failing microstructures, which are the responsible functional units to store the changes and return to their original configuration upon heating process and produce the recoverable stresses. As discussed by Shojaei et al. the strain controlled cyclic loading with non-zero mean stresses results in ratcheting response in which the inelastic strains are accumulated up to the final failure cycle. Due to the fact that the ratcheting plastic strain saturates to a certain value in the case of SMP fibers, the damage parameter is defined as follows:

$$\left|\left|\dot{\boldsymbol{\phi}}\right|\right| = \frac{\left|\left|\boldsymbol{\epsilon}^{vp\,(Res\ \&\ Sat)}\right|\right| - \left|\left|\boldsymbol{\epsilon}^{vp\,(Rec)}\right|\right|}{\left|\left|\Delta\boldsymbol{\epsilon}\right|\right|} \tag{5-36}$$

where $||\Delta\epsilon||$ shows the cyclic applied strain level, e.g. 150% or 300% herein, and $\left|\left|\epsilon^{\mathrm{vp}\,(\mathrm{Res}\ \&\,Sat)}\right|\right|$ is the saturated residual inelastic strains which is measured at higher cycles and this parameter is defined to scale the damage parameter with respect to the loading conditions. Basically the average of the residual inelastic strains in the last two cycles before fracture is considered as $\left|\left|\epsilon^{\mathrm{vp}\,(\mathrm{Res}\ \&\,Sat)}\right|\right|$. The defined damage parameter performs quite well in capturing the cyclic functionality lost of SMP fibers. One may interpret this lost of functionality as initiation and propagation of microscale cracks and polymeric network failure. The third term in Eq. (5-36) is recoverable viscoplastic strain level which is measured through stress recovery tests (see Fig. 5-4).

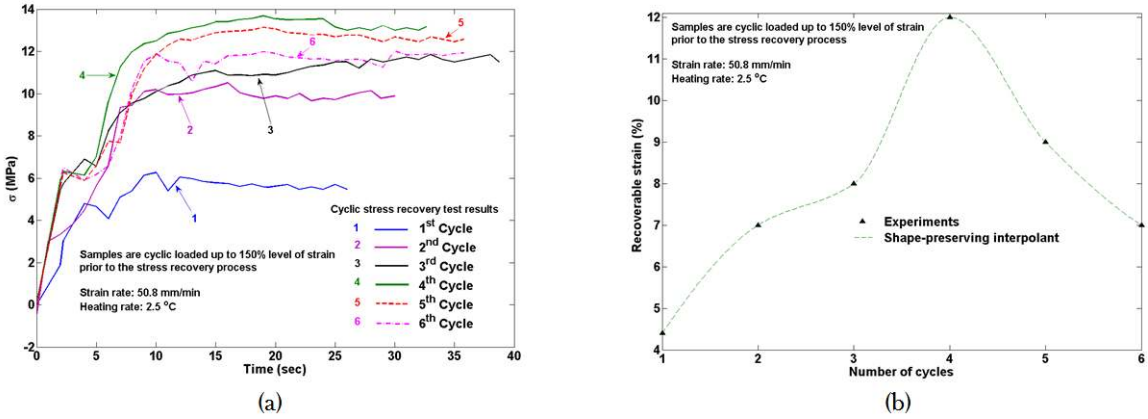

Figure 5-7 Recovery test results for SMP fiber #2 (a) after 150 % cyclic tensions, (b) corresponding recoverable strains

5.8 Multiscale coupled viscoplastic-viscodamage computational aspects

The proposed multiscale scheme in this work requires different microscale computational modules to update the microscale state of plasticity and damage inside each of the sub-phases. Then *amorphous* and *crystalline microscale computation* modules update the microscale fields and *micromechanics computational module* correlates these microscale fields to the macroscopic responses. The return mapping techniques are utilized as the plasticity and damage solution algorithms and these methods are elaborated by Voyiadjis et al. [5]. The detailed description for the cyclic loading numerical algorithm can be found in [57]. As shown in Fig. 5-4 the unloading axes is placed on the final loading point and the unloading stresses and strains are measured with respect to this local coordinate systems. Fig. 5-9 outlines the sequence of the computational modules and input-output flows.

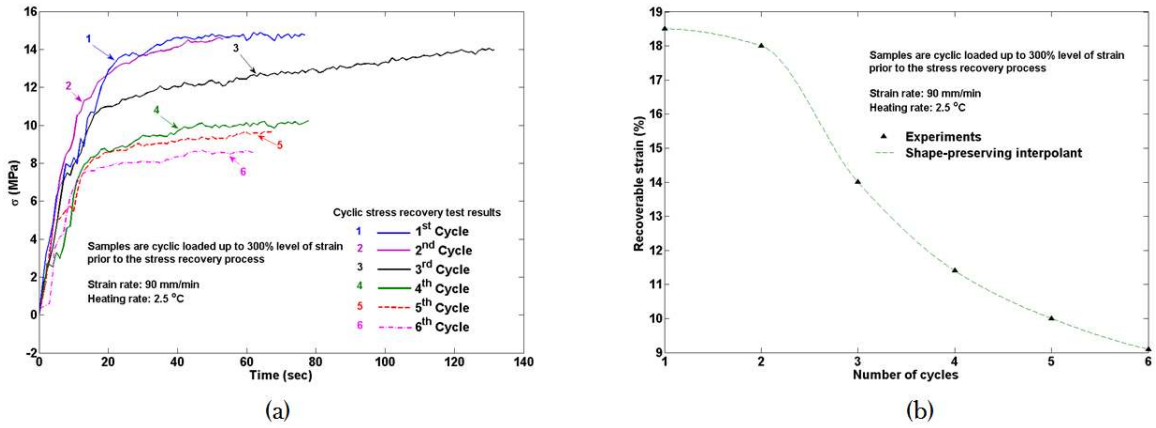

Figure 5-8 Recovery test results for SMP fiber #2 (a) after 300 % cyclic tensions, (b) corresponding recoverable strains

Based on the experimental observations of semicrystalline SMP fiber inelastic responses, a specific deformation mechanism is considered herein to accurately predict their cyclic loading-unloading responses. This deformation mechanism shows excellent correlation with experimental results and it is outlined hereinafter. Let random crystallographic axes, $\boldsymbol{x}$, represent the crystalline texture and the initial amorphous phase is isotropic. The cyclic deformation mechanism of the SMP fiber is assumed to follow the following deformation mechanisms:

1- The crystalline phase deforms in the loading process in accordance with its crystallographic axes. These axes undergo rotation and once the direction of the crystallographic axes aligns with the loading direction, the axes are locked and only the *chain* slippage mechanism remains active. The cyclic evolution of the $\boldsymbol{x}$ component with respect to the loading direction describes the microstructural changes, as shown in Fig. 5-12. This mechanism can efficiently describe the strain hardening effects at higher strain levels where the plastic strains due to the slippage mechanisms are accumulated and crystallographic axes conform to the loading condition. These effects are taken into account through incremental formulations and they update the elastic stiffness of the SMP fiber gradually during the loading process. In other words, after each increment of load the elastic stiffness is updated and all subsequent elastic and plastic strains are computed based on this updated elastic stiffness.

2- Based on the unloading experimental results it is assumed that during the unloading process the major reversed inelastic strains are due to the crystalline phase reverse plasticity. Then the induced texture and volume fraction changes due to the cold-drawing and stress induced crystallization are partially recovered during the unloading process. These changes are captured incrementally by Eqs. (9) and (20)-(25). Furthermore, the Langevin function is turned off during the unloading process while incrementally updated elastic stiffness captures the unloading responses effectively. One may describe these

constraints on the deformation mechanism of SMP fibers through the characterization of the cyclic microstructural changes.

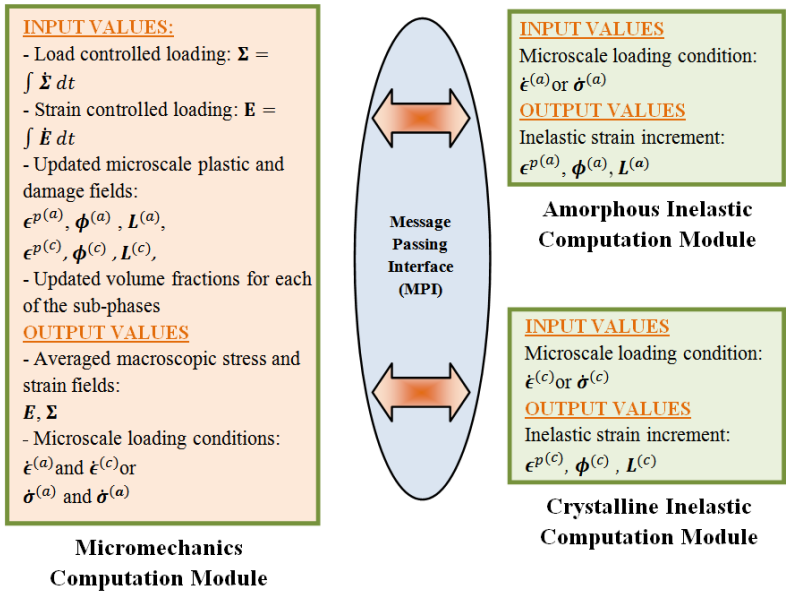

Figure 5-9 Computational modules for the proposed multiscale analysis where a Message Passing Interface is shown as the blue ellipse for parallel programming applications

5.9 Results and discussion

Using an MTS Alliance RT/5 machine, which is specified for fiber tension tests, the SMP fiber is cyclically loaded. The results are shown in Figs. 5-10 and 5-11 in which the SMP fiber is stretched up to 150 % and 300% level of strain respectively with strain rate of 50.80 mm/min. The simulation of the cyclic responses of the SMP fibers are shown respectively in these figures with dashed lines. The material constants are found to fit the experimental results in Fig. 5-10 and the same material constants are utilized to capture the loading condition of 300% level of strain in Fig. 5-11. While excellent correlation between the experimental results and simulation are obtained in Fig. 5-10, utilizing the same material constants for higher loading condition results in some deviation from the experimental results as shown in Fig 5-11. These deviations are unavoidable due to highly non-linear responses of SMP fibers.

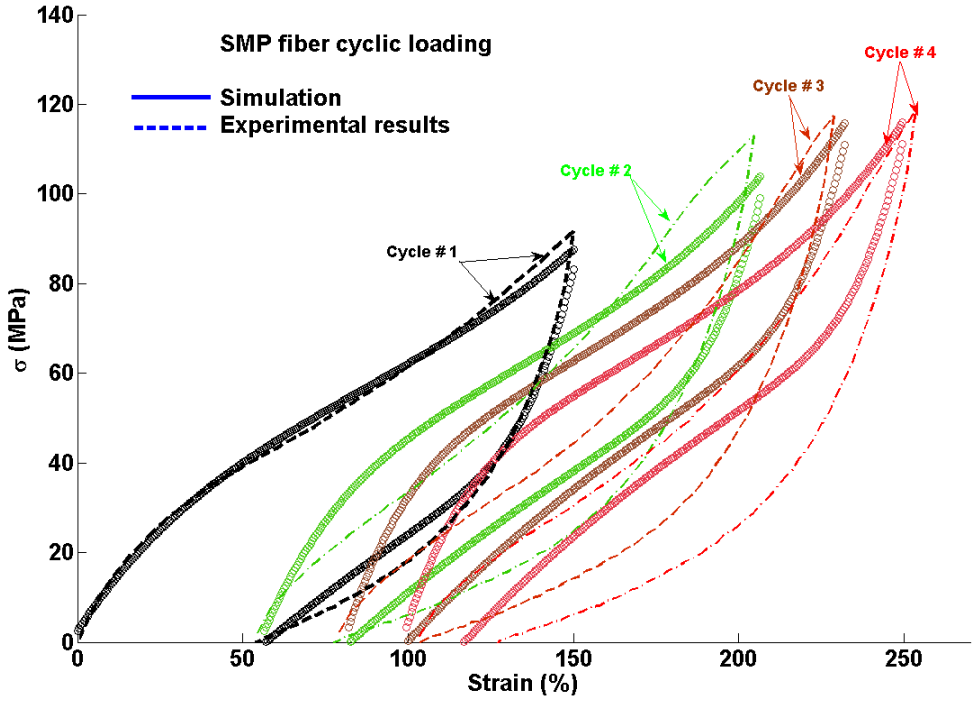

Figure 5-10 Cyclic loading of SMP fiber with $||\Delta\epsilon|| = 150\%$ and strain rate of 50.8 mm/min

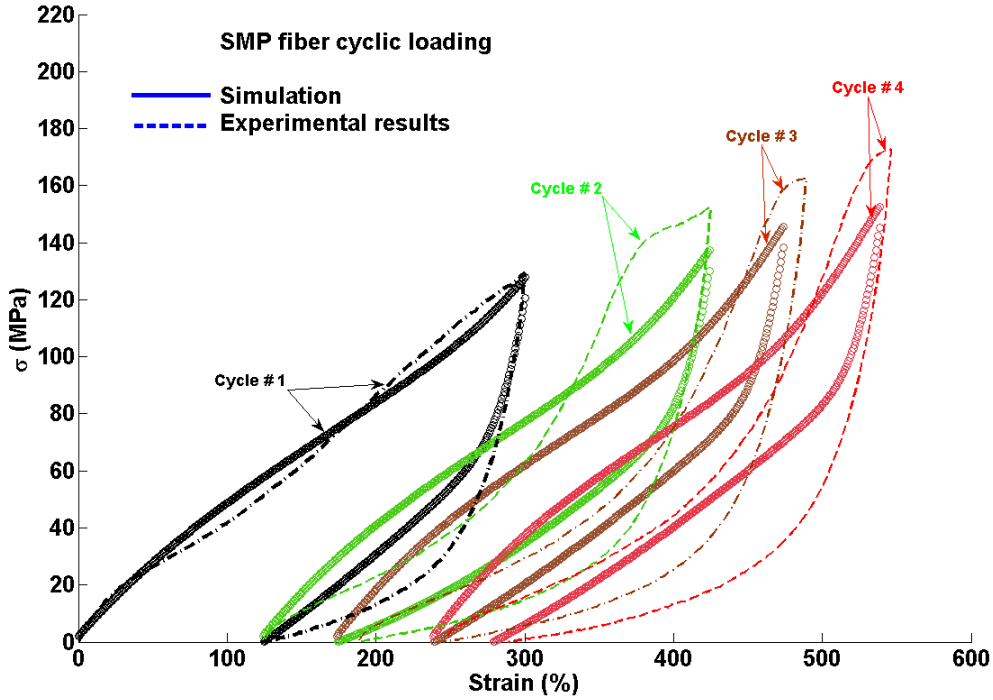

Figure 5-11 Cyclic loading of SMP fiber with $||\Delta\epsilon|| = 300\%$ and strain rate of 50.8 mm/min

Table 5-1 and 5-2 summarize the material constants for the multiscale viscoplastic simulations. The cyclic texture evolution is depicted in Fig. 5-12 in which the updated crystalline axes $\boldsymbol{x}$ are shown for 3 cycles. As discussed in the previous section it is assumed that the crystalline axes conforms to the loading direction and remains locked for the rest of the loading process. Upon the unloading process the crystalline axes are reformed to a more aligned configuration with respect to the loading conditions and after a few cycles the crystalline texture is gradually aligned along the loading direction. As shown in Fig. 5-12 the first component of $\boldsymbol{x}$ is increased after each cycle while the other two components are decreasing. Then the crystallographic axes in Fig. 5-12 are gradually aligned on the loading direction, which is applied at the $x(1)$ direction.

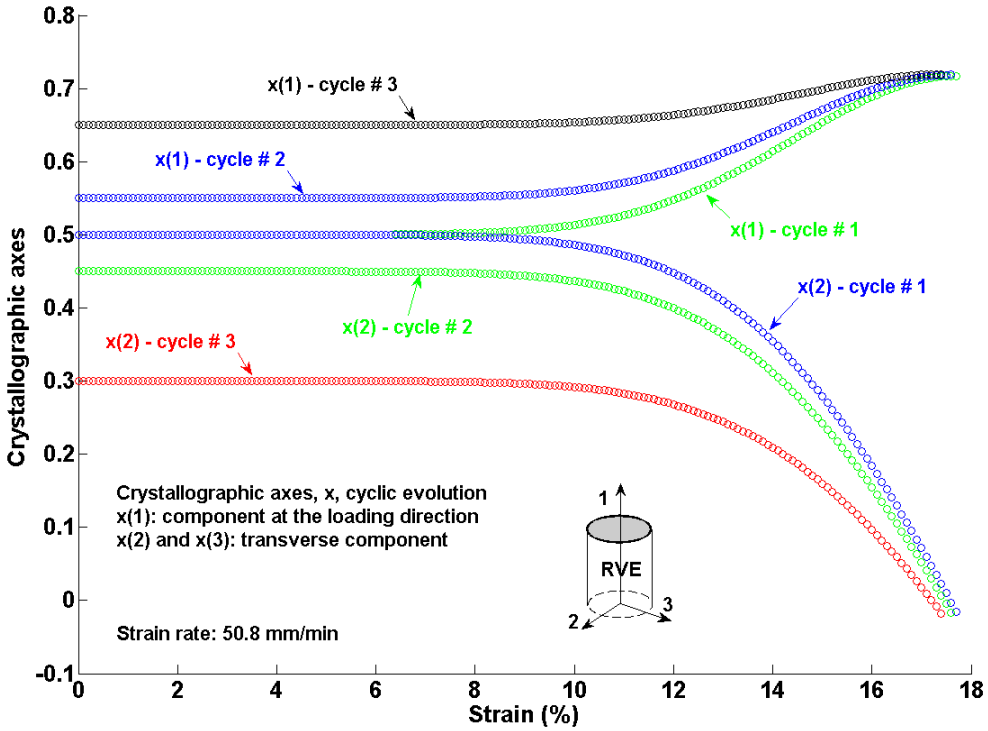

Figure 5-12 Cyclic evolution of the crystalline axes $(0.5, 0.5, 0.5)$

The performance of the proposed viscoplastic theory in capturing the cyclic viscoplastic behavior of the SMP fiber is evaluated at Fig. 5-13. Three different loading rates are examined and it is observed that the higher loading rates result in stiffer cyclic mechanical responses.

The damage evolution in this work relies on functionality of the SMP fibers in which stress recovery responses represent the state of the damage inside the material system. The stress recovery responses after each cycle are precisely measured, as reported in Figs. 5-7 and 5-8. These experimental data are repeated in Fig. 5-14(a) and 5-14(b) together with the simulation results. The material constants for the

damage computation are presented in Table 5-3. These constants are obtained to fit the experimental data for 150% loading condition at Fig. 5-14(a) and they are utilized to estimate the damage for the 300% loading condition at Fig. 5-14(b). While excellent correlation between experiments and simulation is obtained for loading condition $||\Delta\epsilon|| = 150\%$, in the case of $||\Delta\epsilon|| = 300\%$ the simulations deviates from the experimental results. These deviations are due to the viscous nature of SMP fibers in which certain material parameters can only describe certain loading conditions.

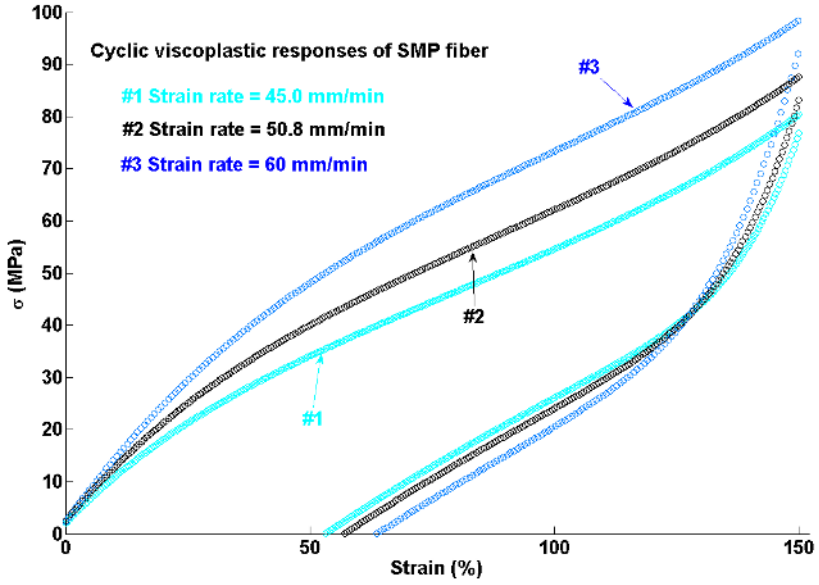

Figure 5-13 Viscoplastic response of SMP fiber at three different strain rates

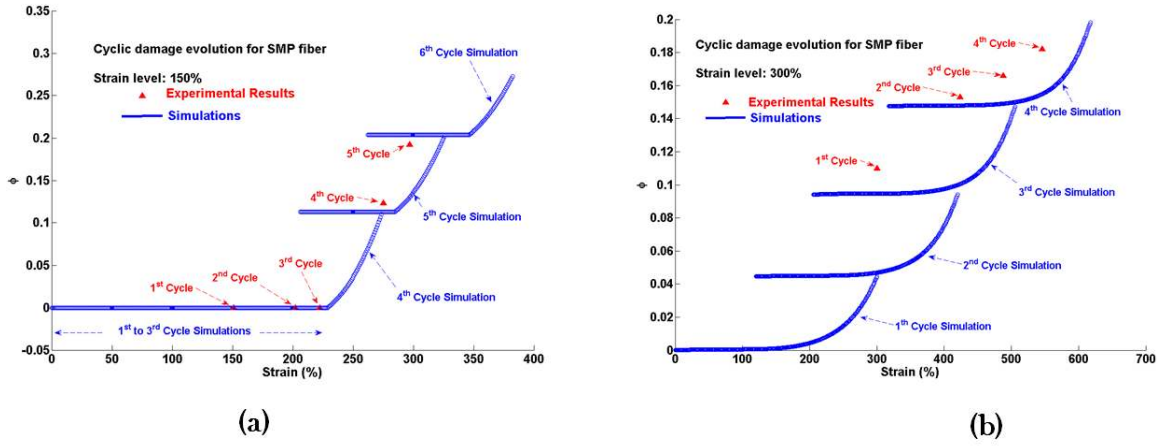

Figure 5-14 Cyclic damage evolution of SMP fiber with loading conditions (a) $||\Delta\epsilon|| = 150\%$, and (b) $||\Delta\epsilon|| = 300\%$

Table 5-1 Material parameters for the crystalline and amorphous computational modules

Amorphous Computational Module (Soft Segment)											
nkT (MPa)	$\dot{\gamma}_0^a$ (sec^{-1})	A	λ_L	h (MPa)	T (K)	s_{ss} (MPa)	ℵ	κ	σ_y (MPa)	E_z (MPa)	E_t (MPa)
0.5	0.03	3.31e-27	7.0	0.5	298	8	0.2	1.2	20	80	50

Crystalline Computational Module (Hard Segment)							
n^c	Reference Cry. Axes	Slippage Systems	$\boldsymbol{\Omega}_1$	Ω_2	σ_y (MPa)	E_z (MPa)	E_t (MPa)
5	(0.5,0.5,0.5)	See Table 2	(1,1,1)	0.2	100	200	50

Table 5-2 Hypothetical crystalline slippage systems

Slippage Type	Indicial Notation	Normalized resistance (g^α/τ_0)
Chain Slip	(100)[001]	1
	(010)[001]	2.5
	{110}[001]	2.5
Transverse Slip	(100)[010]	1.6
	(010)[100]	2.5
	{110}<1$\bar{1}$0>	2.5

Table 5-3 Damage related material parameters

D^d	m	ζ^d	ν^d	η	$\left\|\boldsymbol{\epsilon}^{vp\,(Res\ \&\ Sat)}\right\|$
300	2	0.95	0.002	0.0001	17.5 for$\Delta\epsilon = 150\%$
					102.5 for$\Delta\epsilon = 300\%$

5.10 Conclusion

Potential application of SMP fibers as mechanical actuators in smart material systems is evaluated in this work. A new bio-inspired self-healing material system is proposed in which the stress recovery of the SMP fibers provides the required crack closure force. This system is constituted from thermosetting polymer matrix together with dispersed short SMP fibers and embedded thermoplastic particles. It is found that the polyurethane thermoplastic fibers, upon strain hardening by cold-drawing programming, can achieve the required recovery stress to close macroscopic cracks. Furthermore, the strain hardened SMP fibers show excellent mechanical properties in which a new application field is opened for these fibers to be deployed in SMP fiber reinforced composite structures.

The enhanced mechanical responses of the cold drawn semicrystalline polyurethane SMP fibers are correlated to the stress induced crystallization process and the texture updates in the amorphous and crystalline phases in this work. A micromechanical multiscale viscoplastic theory is developed to link the microscale mechanical responses of the amorphous and crystalline sub-phases to the macroscale mechanical behaviors of the SMP fibers including cyclic hardening, and stress recovery responses. The cyclic loading and cyclic damage responses of the SMP fibers are experimentally investigated in which the proposed theory is utilized to capture these phenomena. A new damage parameter is proposed based on loss of functionality of SMP fibers and the thermodynamic consistent viscodamage theory is develop to accurately predict the damage process. The proposed viscoplastic-viscodamage theory together with the material characterizations of the SMP fibers provides designers with the ability to predict the cyclic strength, stress recovery and life of smart structures made from the semicrystalline SMP fibers.

5.11 References

[1] Voyiadjis, G.Z., A. Shojaei, and G. Li, A thermodynamic consistent damage and healing model for self healing materials. International Journal of Plasticity, 2011a. 27(7): p. 1025-1044.

[2] Green, A.E. and P.M. Naghdi, A general theory of an elastic-plastic continuum. Archive for Rational Mechanics and Analysis, 1965. 18(4): p. 251-281.

[3] Green, A.E. and P.M. Naghdi, Some remarks on elastic-plastic deformation at finite strain. International Journal of Engineering Science, 1971. 9(12): p. 1219-1229.

[4] Naghdi, P.M. and J.A. Trapp, RESTRICTIONS ON CONSTITUTIVE EQUATIONS OF FINITELY DEFORMED ELASTIC-PLASTIC MATERIALS. The Quarterly Journal of Mechanics and Applied Mathematics, 1975. 28(1): p. 25-46.

[5] Meng, Q.H. and J.L. Hu, The Influence of Heat Treatment on Properties of Shape Memory Fibers: I. Crystallinity, Hydrogen Bonding and Shape Memory Effect. Journal of Applied Polymer Science, 2008. 109: p. 2616-2623.

[6] Ping, P., W. Wang, X. Chen, and X. Jing, Poly(ε-caprolactone) Polyurethane and Its Shape-Memory Property†. Biomacromolecules, 2005. 6(2): p. 587-592.

[7] Clough, S.B., N.S. Schneider, and A.O. King, Small-angle X-Ray scattering from polyurethane elastomers. Journal of Macromolecular Science, Part B, 1968. 2(4): p. 641-648.

[8] Negahban, M., Thermodynamic modeling of the thermomechanical effects of polymer crystallization: A general theoretical structure. International Journal of Engineering Science, 1997. 35(3): p. 277-298.

[9] Negahban, M. and A.S. Wineman, Modeling the mechanical response of a material undergoing continuous isothermal crystallization. International Journal of Engineering Science, 1992. 30(7): p. 953-962.

[10] Negahban, M., A.S. Wineman, and R.-J. Ma, Simulation of mechanical response in polymer crystallization. International Journal of Engineering Science, 1993. 31(1): p. 93-113.

[11] Stevenson, A., Effetc of crystallization on the mechanical properties of elastomers under large deformation in Current Research in the Thermo-Mechanics of Polymers in the Rubbery-Glassy Range. 1995, ASME.

[12] Wang, T.T., Morphology and mechanical properties of crystalline polymers. I. Transcrystalline polyethylene. Journal of Applied Physics, 1973. 44(5): p. 2218-2224.

[13] Argon, A.S., A theory for the low-temperature plastic deformation of glassy polymers. Philosophical Magazine, 1973. 28(4): p. 839 – 865.

[14] Arruda, E.M. and M.C. Boyce, Evolution of plastic anisotropy in amorphous polymers during finite straining. International Journal of Plasticity, 1993. 9(6): p. 697-720.

[15] Arruda, E.M. and M.C. Boyce, A three-dimensional constitutive model for the large stretch behavior of rubber elastic materials. Journal of the Mechanics and Physics of Solids, 1993. 41(2): p. 389-412.

[16] Arruda, E.M., M.C. Boyce, and H. Quintus-Bosz, Effects of initial anisotropy on the finite strain deformation behavior of glassy polymers. International Journal of Plasticity, 1993. 9(7): p. 783-811.

[17] Boyce, M.C., D.M. Parks, and A.S. Argon, Large inelastic deformation of glassy polymers. part I: rate dependent constitutive model. Mechanics of Materials, 1988. 7(1): p. 15-33.

[18] Boyce, M.C., D.M. Parks, and A.S. Argon, Large inelastic deformation of glassy polymers. Part II: numerical simulation of hydrostatic extrusion. Mechanics of Materials, 1988. 7(1): p. 35-47.

[19] Boyce, M.C., D.M. Parks, and A.S. Argon, Plastic flow in oriented glassy polymers. International Journal of Plasticity, 1989. 5(6): p. 593-615.

[20] Cohen, A., A Pade' approximant to the inverse Langevin function. Rheologica Acta, 1991. 30: p. 270-273.

[21] Parks, D.M. and S. Ahzi, Polycrystalline plastic deformation and texture evolution for crystals lacking five independent slip systems. Journal of the Mechanics and Physics of Solids, 1990. 38(5): p. 701-724.

[22] Lee, B.J., D.M. Parks, and S. Ahzi, Micromechanical modeling of large plastic deformation and texture evolution in semi-crystalline polymers. Journal of the Mechanics and Physics of Solids, 1993. 41(10): p. 1651-1687.

[23] Hutchinson, J.W., Bounds and Self-Consistent Estimates for Creep of Polycrystalline Materials. Proceedings of the Royal Society of London. A. Mathematical and Physical Sciences, 1976. 348(1652): p. 101-127.

[24] Asaro, R.J., Geometrical effects in the inhomogeneous deformation of ductile single crystals. Acta Metallurgica, 1979. 27(3): p. 445-453.

[25] Asaro, R.J. and J.R. Rice, Strain localization in ductile single crystals. Journal of the Mechanics and Physics of Solids, 1977. 25(5): p. 309-338.

[26] Hershey, A.V., The elasticity of an isotropic aggeregate of anisotropic cubic crystal Journal of Applied Mechanics, 1954. 21: p. 236-241.

[27] Voyiadjis, G.Z., A. Shojaei, and G. Li, A Generalized Coupled Viscoplastic- Viscodamage-Viscohealing Theory for Glassy Polymers. International Journal of Plasticity, 2012b. 28(1): p. 21-45.

[28] Voyiadjis, G. Z., Shojaei, A, Li, G. and Kattan, P.I.,A Theory of Anisotropic Healing and Damage Mechanics of Materials. Proceeding of The Royial Society A, 2012, 468(2137): 163-183.

[29] Lemaitre, J., Coupled elasto-plasticity and damage constitutive equations. Computer Methods in Applied Mechanics and Engineering, 1985. 51(1-3): p. 31-49.

[30] Lemaitre, J. and J. Dufailly, Damage measurements. Engineering Fracture Mechanics, 1987. 28(5-6): p. 643-661.

[31] Freed, A.D. and K.P. Walker, Steady-State and Transient Zener Parameters in Viscoplasticity: Drag Strength Versus Yield Strength. Applied Mechanics Reviews, 1990. 43(5S): p. S328-S337.

[32] Deliktas, B., G.Z. Voyiadjis, and A.N. Palazotto, Simulation of perforation and penetration in metal matrix composite materials using coupled viscoplastic damage model. Composites Part B: Engineering, 2009. 40(6): p. 434-442.

[33] Voyiadjis, G.Z., B. Deliktas, and A.N. Palazotto, Thermodynamically consistent coupled viscoplastic damage model for perforation and penetration in metal matrix composite materials. Composites Part B: Engineering, 2009. 40(6): p. 427-433.

[34] Voyiadjis, G.Z., A. Shojaei, G. Li and Kattan P.I., Continuum Damage-Healing Mechanics with Introduction to New Healing Variables. International Journal of Damage Mechanics, 2011. In press.

[35] Shojaei, A., M. Eslami, and H. Mahbadi, Cyclic loading of beams based on the Chaboche model. International Journal of Mechanics and Materials in Design, 2010. 6(3): p. 217-228.

CHAPTER 6 SUMMARY AND FUTURE WORKS

6.1 Summary

In this dissertation, the application of SMP fibers as actuators is investigated with application in smart material systems. A multiscale viscoplastic scheme is developed to analyze the bulk SMP and then this scheme is further developed to study the viscoplastic and viscodamage responses of SMP fibers. Several experimental results, such as DMA, SAXS, and TFIR, are brought forward to justify the theoretical formulations. A summary of the main results is as follows.

6.1.1 Modified two-phase TFA multiscale scheme

- A multiscale scheme is developed which utilizes the physical description of mechanical responses of each of the micro-constituents phases. The developed theory incorporates more realistic deformation mechanisms compared to phenomenological models.
- A novel modification is proposed on TFA multiscale analysis in which analytical solution of a two-phase material system is generalized to capture the localized viscoplastic behaviors.

6.1.2 SMP fiber evolution

- Cyclic loading of SMP fibers is investigated and the proposed multiscale theory is extended further to investigate the cyclic responses of SMP fibers.
- A viscodamage theory is developed to investigate the cyclic damage responses of SMP fibers. A new damage parameter is defined based on lose of functionality of SMP fibers and the cyclic damage behavior of these fibers is investigated theoretically and experimentally.

6.2 Recommendation of Future Works

SMP fibers are relatively new topics in the smart materials field. Much more research works are necessary to gain a thorough understanding of their working mechanism. The following recommendations are made for possible future research:

- According to the experiment results in this dissertation, the texture evolution of the SMP fibers is highly related to the loading conditions. A full understanding of texture dependency on level of the loading and also effect of stress relaxation on texture changes is required.
- A complete three-dimensional FEA model considering time dependent stress relaxation and texture evolution needs to be developed to simulate the behavior of the embedded SMP fiber within a material system such as self-healing grid structures.
- Utilizing the FEA analysis the crack closure and diffusion of molten TP into the crack surfaces can be investigated.

- The responses of short SMP fibers can be analyzed through FEA analysis and introducing the developed theory to the commercial FEA codes such as ABAQUS by developing user-defined subroutines such as UMAT (ABAQUS standard) or VUMAT (ABAQUS explicit).

APPENDIX A: ESHELBY TENSOR

For simplification the fourth order tensors are compacted into six order matrix and second order tensors are compacted into sixth order vectors as indicated in the following:

$$T_{ijkl} \Rightarrow \tilde{T}_{ij} = \begin{bmatrix} T_{1111} & T_{1122} & T_{1133} & T_{1123} & T_{1113} & T_{1112} \\ T_{2211} & T_{2222} & T_{2233} & T_{2223} & T_{2213} & T_{2212} \\ T_{3311} & T_{3322} & T_{3333} & T_{3323} & T_{3313} & T_{3312} \\ T_{2311} & T_{2322} & T_{2333} & T_{2323} & T_{2313} & T_{2312} \\ T_{1311} & T_{1322} & T_{1333} & T_{1323} & T_{1313} & T_{1312} \\ T_{1211} & T_{1222} & T_{1233} & T_{1223} & T_{1213} & T_{1212} \end{bmatrix}_{6\times 6}$$

$$P_{ij} \Rightarrow \tilde{P}_i = \begin{bmatrix} P_{11} \\ P_{22} \\ P_{33} \\ P_{23} \\ P_{31} \\ P_{12} \end{bmatrix}_{6\times 1} \tag{A1}$$

With this approach the stress-strain relation is reduced to the following expression in the case of the orthotropic materials:

$$\sigma_{ijkl} = L_{ijkl}\,\epsilon_{kl} \Rightarrow \begin{bmatrix} \sigma_{11} \\ \sigma_{22} \\ \sigma_{33} \\ \sigma_{23} \\ \sigma_{31} \\ \sigma_{12} \end{bmatrix} = \begin{bmatrix} L_{1111} & L_{1122} & L_{1133} & L_{1123} & L_{1113} & L_{1112} \\ L_{2211} & L_{2222} & L_{2233} & L_{2223} & L_{2213} & L_{2212} \\ L_{3311} & L_{3322} & L_{3333} & L_{3323} & L_{3313} & L_{3312} \\ L_{2311} & L_{2322} & L_{2333} & L_{2323} & L_{2313} & L_{2312} \\ L_{1311} & L_{1322} & L_{1333} & L_{1323} & L_{1313} & L_{1312} \\ L_{1211} & L_{1222} & L_{1233} & L_{1223} & L_{1213} & L_{1212} \end{bmatrix} \begin{bmatrix} \epsilon_{11} \\ \epsilon_{22} \\ \epsilon_{33} \\ \epsilon_{23} \\ \epsilon_{31} \\ \epsilon_{12} \end{bmatrix} \tag{A2}$$

where

$$L_{1111} = 1/E_1;\; L_{1122} = -\nu_{12}/E_2;\; L_{1133} = -\nu_{31}/E_3\;;\; L_{2211} = -\nu_{12}/E_1; \tag{A3}$$

$$L_{2222} = 1/E_2;\ L_{2233} = -\nu_{23}/E_3\ ; L_{3311} = -\nu_{31}/E_1; L_{3322} = -\nu_{23}/E_2;$$

$$L_{3333} = 1/E_3; L_{2323} = 1/\mu_{23}; L_{1313} = 1/\mu_{13}; L_{1212} = 1/\mu_{12};$$

where E_1, E_2 and E_3 are elastic modulus in principal directions and ν_{12}, ν_{23} and ν_{31} are Poission's ratio; and μ_{12}, μ_{23} and μ_{13} are shear modulus with respect to principal directions. The following components of the Eshelby tensor for ellipsoidal cylinder inclusion ($a_1 \neq a_2$, and $a_3 \to \infty$) are then assembled into a sixth order matrix:

$$\begin{aligned}
S_{1111} &= \frac{1}{2(1-\nu)}\left(\frac{a_2^2+2a_1a_2}{(a_1+a_2)^2} + (1-2\nu)\frac{a_2}{a_1+a_2}\right);\\
S_{2222} &= \frac{1}{2(1-\nu)}\left(\frac{a_1^2+2a_1a_2}{(a_1+a_2)^2} + (1-2\nu)\frac{a_1}{a_1+a_2}\right);\\
S_{3333} &= 0;\\
S_{1122} &= \frac{1}{2(1-\nu)}\left(\frac{a_2^2}{(a_1+a_2)^2} - (1-2\nu)\frac{a_2}{a_1+a_2}\right);\\
S_{2233} &= \frac{\nu}{(1-\nu)}\left(\frac{a_1}{a_1+a_2}\right);\\
S_{2211} &= \frac{1}{2(1-\nu)}\left(\frac{a_1^2}{(a_1+a_2)^2} - (1-2\nu)\frac{a_1}{a_1+a_2}\right);\\
S_{1133} &= \frac{\nu}{(1-\nu)}\left(\frac{a_2}{a_1+a_2}\right);\\
S_{3311} &= S_{3322} = 0;\\
S_{1212} &= \frac{1}{2(1-\nu)}\left(\frac{a_1^2+a_2^2}{2(a_1+a_2)^2} + \frac{1-2\nu}{2}\right);\\
S_{2323} &= \frac{a_1}{2(a_1+a_2)};\ S_{3131} = \frac{a_2}{2(a_1+a_2)}.
\end{aligned} \tag{A4}$$

For a penny shape inclusion ($a_1 = a_2 \gg a_3$) the Eshelby tensor components are:

$$\begin{aligned}
S_{1111} &= S_{2222} = \frac{\pi(13-8\nu)}{32(1-\nu)}\frac{a_3}{a_1},\\
S_{3333} &= 1 - \frac{\pi(1-2\nu)}{4(1-\nu)}\frac{a_3}{a_1},\\
S_{1122} &= S_{2211} = \frac{\pi(8\nu-1)}{32(1-\nu)}\frac{a_3}{a_1},
\end{aligned} \tag{A5}$$

$$S_{1133} = S_{2233} = \frac{\pi(2\nu-1)}{8(1-\nu)}\frac{a_3}{a_1},$$

$$S_{3311} = S_{3322} = \frac{\nu}{1-\nu}\left(1 - \frac{\pi(4\nu+1)}{8\nu}\frac{a_3}{a_1}\right),$$

$$S_{1212} = \frac{\pi(7-8\nu)}{32(1-\nu)}\frac{a_3}{a_1},$$

$$S_{2323} = S_{3131} = \frac{1}{2}\left(1 + \frac{\pi(\nu-2)}{4(1-\nu)}\frac{a_3}{a_1}\right).$$

APPENDIX B: LETTERS OF PERMISSION TO USE PUBLISHED MATERIAL

From: The Royal Society, Proceedings A
To: Amir Shojaei
Date: Apr 12, 2012
Subject: License Agreement

This is a License Agreement between Amir Shojaei ("You") and The Royal Society ("The Royal Society") provided by Copyright Clearance Center ("CCC"). The license consists of your order details, the terms and conditions provided by The Royal Society, and the payment terms and conditions.

License Number	2886480169021
License date	Apr 12, 2012
Licensed content publisher	The Royal Society
Licensed content publication	Proceedings A
Licensed content title	A viscoplastic theory of shape memory polymer fibres with application to self-healing materials
Licensed ccopyright line	Copyright © 2012, The Royal Society
Licensed content author	Guoqiang Li, Amir Shojaei
Licensed content date	April 11, 2012
Type of Use	Thesis/Dissertation
Requestor type	academic/educational
Format	print and electronic
Portion	text extract
Number of pages requested	25
Will you be translating?	no
Circulation	1
Order reference number	
Title of your thesis / dissertation	MULTISCALE VISCOPLASTIC-VISCODAMGE ANALYSIS OF SHAPE MEMORY POLYMER FIBERS WITH APPLICATION TO SELF HEALING SMART MATERIALS
Expected completion date	May 2012
Estimated size (number of pages)	138
Billing Type	Credit Card

Credit card info	Visa ending in 1037
Credit card expiration	12/2013
Permissions Cost	4.20 USD
VAT (0.0%)	0.00 USD
Total	4.20 USD

Terms and Conditions

STANDARD TERMS AND CONDITIONS FOR REPRODUCTION OF MATERIAL FROM A ROYAL SOCIETY JOURNAL

1. Use of the material is restricted to the type of use specified in your order details.

2. The publisher for this copyrighted material is the Royal Society. By clicking "accept" in connection with completing this licensing transaction, you agree that the following terms and conditions apply to this transaction (along with the Billing and Payment terms and conditions established by Copyright Clearance Center, Inc. ("CCC"), at the time that you opened your Rightslink account and that are available at any time at http://myaccount.copyright.com.

3. You may not alter or modify the material in any manner, nor may you translate the material into another language without written consent of the Royal Society.

4. The following credit line appears wherever the material is used: author, title, journal, year, volume, issue number, pagination, by permission of the Royal Society.

5. For the reproduction of a full article from a Royal Society journal for whatever purpose, the corresponding author of the material concerned should be informed of the proposed use. Contact details for the corresponding authors of all Royal Society journals can be found alongside either the abstract or full text of the article concerned, accessible from royalsocietypublishing.org.

6. If the credit line in our publication indicates that any of the figures, images or photos was reproduced from an earlier source it will be necessary for you to clear this permission with the original publisher as well. If this permission has not been obtained, please note that this material cannot be included in your publication/photocopies.

7. Licenses may be exercised anywhere in the world.

8. While you may exercise the rights licensed immediately upon issuance of the license at the end of the licensing process for the transaction, provided that you have disclosed complete and accurate details of your proposed use, no license is finally effective unless and until full payment is received from you (either by publisher or by CCC) as provided in CCC's Billing and Payment terms and conditions. If full payment is not received on a timely basis, then any license preliminarily granted shall be deemed automatically revoked and shall be void as if never granted. Further, in the event that you breach any of these terms and conditions or any of CCC's Billing and Payment terms and conditions, the license is

automatically revoked and shall be void as if never granted. Use of materials as described in a revoked license, as well as any use of the materials beyond the scope of an unrevoked license, may constitute copyright infringement and publisher reserves the right to take any and all action to protect its copyright in the materials.

9. Publisher reserves all rights not specifically granted in the combination of (i) the license details provided by you and accepted in the course of this licensing transaction, (ii) these terms and conditions and (iii) CCC's Billing and Payment terms and conditions.

10. Publisher makes no representations or warranties with respect to the licensed material.

11. You hereby indemnify and agree to hold harmless publisher and CCC, and their respective officers, directors, employees and agents, from and against any and all claims arising out of your use of the licensed material other than as specifically authorized pursuant to this license.

12. This license may not be amended except in a writing signed by both parties (or, in the case of publisher, by CCC on publisher's behalf).

If you would like to pay for this license now, please remit this license along with your payment made payable to "COPYRIGHT CLEARANCE CENTER" otherwise you will be invoiced within 48 hours of the license date. Payment should be in the form of a check or money order referencing your account number and this invoice number RLNK500759063.
Once you receive your invoice for this order, you may pay your invoice by credit card. Please follow instructions provided at that time.

Make Payment To:
Copyright Clearance Center
Dept 001
P.O. Box 843006
Boston, MA 02284-3006

For suggestions or comments regarding this order, contact RightsLink Customer Support: customercare@copyright.com or +1-877-622-5543 (toll free in the US) or +1-978-646-2777.

Gratis licenses (referencing $0 in the Total field) are free. Please retain this printable license for your reference. No payment is required.

VITA

Amir Shojaei was born in Esfahan, Iran. He received Bachelor of Mechanical Engineering from Kashan University in 2006 and in 2008 he received his Master degree of Mechanical Engineering - Applied Mechanics from Amir-kabir University of Technology. In August 2009, he started to pursue his doctoral study in the Department of Mechanical Engineering at Louisiana State University. Since then, he had been a doctoral student under the guidance of Dr. Guoqiang Li, John W. Rhea, Jr. Associate Professor in the Department of Mechanical Engineering at Louisiana State University and his minor Professor was Dr. George Z. Voyiadjis, Boyd Professor, Chair and Bingham C. Stewart Distinguished Professor of Engineering in Department of Civil and Environmental Engineering. Amir Shojaei will receive his Doctor of Philosophy degree at the 2012 Summer Commencement and will join the Mechanical Engineering Department of University College London, UK, to pursue his academic career as a research associate.